FINAL TECHNICAL PROGRESS REPORT
For Award Period 10/1/01 – 4/30/05

DoE Award #**DE-FC26-01NT41203**
"High-Efficiency Nitride-Based Solid-State Lighting"

JULY 30, 2005

Authors: Dr. Paul T. Fini, Prof. Shuji Nakamura

University of California, Santa Barbara
Materials Dept., Bldg. 503, Rm. 1355
Santa Barbara, CA 93106-5050

DISCLAIMER

"This report was prepared as an account of work sponsored by an agency of the United States Government. Neither the United States Government nor any agency thereof, nor any of their employees, makes any warranty, express or implied, or assumes any legal liability or responsibility for the accuracy, completeness, or usefulness of any information, apparatus, product, or process disclosed, or represents that its use would not infringe privately owned rights. Reference herein to any specific commercial product, process, or service by trade name, trademark, manufacturer, or otherwise does not necessarily constitute or imply its endorsement, recommendation, or favoring by the United States Government or any agency thereof. The views and opinions of authors expressed herein do not necessarily state or reflect those of the United States Government or any agency thereof."

ABSTRACT

In this final technical progress report we summarize research accomplished during Department of Energy contract #**DE-FC26-01NT41203**, entitled "High-Efficiency Nitride-Based Solid-State Lighting". Two teams, from the University of California at Santa Barbara (Principle Investigator: Dr. Shuji Nakamura) and the Lighting Research Center at Rensselaer Polytechnic Institute (led by Dr. N. Narendran), pursued the goals of this contract from thin film growth, characterization, and packaging/luminaire design standpoints.

The UCSB team initially pursued the development of blue gallium nitride (GaN)-based vertical-cavity surface-emitting lasers, as well as ultraviolet GaN-based light emitting diodes (LEDs). In Year 2, the emphasis shifted to resonant-cavity light emitting diodes, also known as micro-cavity LEDs when extremely thin device cavities are fabricated. These devices have very directional emission and higher light extraction efficiency than conventional LEDs. Via the optimization of thin-film growth and refinement of device processing, we decreased the total cavity thickness to less than 1 μm, such that micro-cavity effects were clearly observed and a light extraction efficiency of over 10% was reached. We also began the development of photonic crystals for increased light extraction, in particular for so-called 'guided modes' which would otherwise propagate laterally in the device and be re-absorbed. Finally, we pursued the growth of smooth, high-quality nonpolar *a*-plane and *m*-plane GaN films, as well as blue light emitting diodes on these novel films. Initial nonpolar LEDs showed the expected behavior of negligible peak wavelength shift with increasing drive current. *M*-plane LEDs in particular show promise, as unpackaged devices had unsaturated optical output power of ~ 3 mW at 200 mA drive current.

The LRC's tasks were aimed at developing the subcomponents necessary for packaging UCSB's light emitting diodes, and packaging them to produce a white light fixture. During the third and final year of the project, the LRC team investigated alternate packaging methods for the white LED device to achieve at least 25 percent more luminous efficacy than traditional white LEDs; conducted optical ray-tracing analyses and human factors studies to determine the best form factor for the white light source under development, in terms of high luminous efficacy and greater acceptance by subjects; and developed a new die encapsulant using silicone-epoxy resins that showed less yellowing and slower degradation. At the conclusion of this project, the LRC demonstrated a new packaging method, called scattered photon extraction (SPE), that produced an average luminous flux and corresponding average efficacy of 90.7 lm and 36.3 lm/W, respectively, compared with 56.5 lm and 22.6 lm/W for a similar commercial white LED package. At low currents, the SPE package emitted white light with an efficacy of over 80 lm/W and had chromaticity values very close to the blackbody locus. The SPE package showed an overall improvement of 61% for this particular comparison, exceeding the LRC's third-year goal of 25% improvement.

TABLE OF CONTENTS

LIST OF FIGURES, TABLES 5

EXECUTIVE SUMMARY 10

INTRODUCTION AND EXPERIMENTAL 14
E.1 Experimental Apparatus 14
E.2 Vertical Cavity Surface Emitting Laser (VCSEL) Fabrication 18
E.3 Ultraviolet LED Growth and Fabrication 21
E.4 RCLED and MCLED Development 22
E.5 A-plane GaN Lateral Overgrowth by HVPE 24
E.6 A-plane LEDs on HVPE LEO Templates 24
E.7 M-plane LEDs on Free-Standing HVPE GaN 25
E.8 Source Modeling 26
E.9 Phosphor Characterization and Secondary Optics Studies 27
E.10 Understanding Source Form Factors for General Illumination 27
E.11 Development of LED Encapsulants 28
E.12 Benchmarking Current, State-of-the-art LED Devices 29

RESULTS AND DISCUSSION 30
R.1 Vertical Cavity Surface Emitting Laser (VCSEL) Fabrication 30
R.2 Ultraviolet LED Growth and Fabrication 34
R.3 RCLED and MCLED Development 37
R.4 A-plane GaN Lateral Overgrowth by HVPE 45
R.5 A-plane LEDs on HVPE LEO Templates 47
R.6 M-plane LEDs on Free-Standing HVPE GaN 49
R.7 Source Modeling 52
R.8 Phosphor Characterization and Secondary Optics Studies 53
R.9 Understanding Source Form Factors for General Illumination 66
R.10 Development of LED Encapsulants 99
R.11 Benchmarking Current, State-of-the-art LED devices 104

CONCLUSIONS 113

UCSB, LRC Papers and Pending Patents 116

REFERENCES 119

APPENDICES 122
A.1 Views of experimental conditions for the mockup experiment 122
A.2 Questionnaire for mockup experiment 123
A.3 Results of subjective evaluations for the 12 pairs of contrasting words 124
A.4 UGR formula (CIE, 1995) 126
A.5 Layouts and views of light sources in scale model experiment 127
A.6 Questionnaire for scale model experiment 129
A.7 Results (p-values) of t-tests for the scale model experiment 130

LIST OF GRAPHICAL MATERIALS

Fig. 1. Pictorial cut-away schematic of a multi-wafer close-spaced vertical showerhead deposition chamber.

Fig. 2. Front view of MOCVD system (left) and Control Panel (right).

Fig. 3. Front view of HVPE system shortly after move-in and installation.

Fig. 4. Schematic of angular measurement system for RCLED testing.

Fig. 5. Picture of FEI focused-ion beam etching system.

Fig. 6. Cross-section device schematic (above) and a SEM micrograph (below) of a 10 μm aperture device prior to flip-chip bonding.

Fig. 7. Illustration of gain-length difference between edge-emitter and VCSEL.

Fig. 8. MOCVD layer structure for the device in Fig. 6.

Fig. 9. Side-view schematic of VCSEL cavity position relative to LEO stripe (left), and optical micrograph of fabricated VCSELs on a coalesced LEO film (right).

Fig. 10. Schematics of the structures of UV LEDs with 'bulk' (top) and 'SPASL' (bottom) cladding layers.

Fig. 11. Schematic of MCLED epitaxial thin film structure.

Fig. 12. Schematic of processed MCLED device structure.

Fig. 13. Schematic of blue LED device structure on *a*-plane LEO GaN template.

Fig. 14. Schematic of *m*-plane GaN LED on free-standing *m*-plane HVPE GaN template.

Fig. 15. L-I-V characteristics for a 10 μm aperture 10 QW device with an ITO contact, pulsed at 5 kHz with varying pulse widths.

Fig. 16. L-I-V characteristics for a 10 μm aperture 10 QW device with an ITO contact, pulsed at 5 kHz.

Fig. 17. Comparison of 110 nsec, 5 kHz pulsed L-I-V curves for 5 and 10 QW 2 μm aperture devices with ITO contacts.

Fig. 18. Comparison of 110 nsec, 5 kHz pulsed L-I-V curves for 10 QW devices with ITO contacts and varying aperture diameters.

Fig. 19. L-I-V characteristics of a 5 μm implant-defined aperture device, pulsed at 5 kHz and varying pulse widths.

Fig. 20. Pulsed spectrum (200 nsec, 5 kHz) for a 10 μm aperture 10 QW device with an ITO contact.

Fig. 21. Zoomed-in pulsed spectrum (50 nsec, 5 kHz) for a 10 μm aperture 10 QW device with an ITO contact.

Fig. 22. Photoluminescence of bulk-clad LEDs with varying amounts of Al in the barriers between quantum wells.

Fig. 23. Comparison of DC IV for bulk- and SPASL-clad MQW UV LEDs.

Fig. 24. Electroluminescence (EL) from SPASL-clad 130x130 μm UV LEDs with 3 and 5 QWs, at 20, 40, 60, and 80 mA drive current.

Fig. 25. Voltage (V) and output power (P) vs. current (I) for 5 QW (left) vs. 3 QW (right) SL-clad LEDs.

Fig. 26. Output power vs. current (I) for 5QW LEDs of various lateral sizes.

Fig. 27. Size of cavity and source position vs. mode formation.

Fig. 28. RCLED extraction efficiency (scale on right) vs. cavity length and QW position.

Fig. 29. Angular dependence of emission for a conventional LED (left), a microcavity with a cavity order of 8 (center), and a thinner microcavity with an order of 2 (right). The red lines delineate the extraction cone, which depends on the difference in refractive indices between the LED and its surroundings.

Fig. 30. Schematic of concentric etched ring extraction scheme.

Fig. 31. Schematic of a triangular photonic crystal surrounding an active region (above), and an SEM micrograph of holes etched into GaN with a focused ion beam (below).

Fig. 32. Ewald diagrams of light diffraction in triangular 2-D photonic crystals as a function of direction ($\theta = 0$, 30, or 90°).

Fig. 33. Schematic of an A7 Archimedean tiling (left), and its associated diffraction pattern (right).

Fig. 34. Schematic of an A7 Archimedean tiling (above), and an SEM micrograph of this tiling etched into GaN with a focused ion beam (below).

Fig. 35. Emission Spectra of a standard LED (black) and an MCLED (red) processed from the same epitaxial film.

Fig. 36. Contour plot of the MCLED far-field emission, expressed as wavelength at various emission angles.

Fig. 37. (a) Nomarski optical contrast micrograph of a coalesced LEO *a*-plane GaN film. The stripes are oriented along the $[10\bar{1}0]$ direction. (b-d) AFM images of coalesced $[10\bar{1}0]$-oriented GaN stripes: (b) 40 x 40 μm image showing the relative surface quality of the window and wing regions. (c) Magnified view of the window region. (d) Magnified view of the overgrown region.

Fig. 38. (a) Cross-sectional SEM image of parallel LEO stripes approaching coalescence. (b) Cross-sectional SEM image showing coalesced stripes. The arrows mark sub-micron voids at the wing-mask interface where the stripes coalesced. (c) Plan-view SEM image of the coalesced region pictured in (d), which is a monochromatic CL image of the region shown in (c) at 365 nm. The mask in each case consisted of parallel SiO_2 stripes along the GaN $[10\bar{1}0]$ direction.

Fig. 39. (a) Cross-sectional TEM image of an *a*-GaN LEO stripe. (b) Plan-view TEM image.

Fig. 40. Electroluminescence spectrum of an *a*-plane LED as a function of drive current. Note the negligible shift of peak wavelength over this current range.

Fig. 41. Output power (left) and external quantum efficiency (right) of an *a*-plane LED as a function of drive current.

Fig. 42. (a) Digital photograph of a free-standing *m*-plane GaN wafer on a 1 mm^2 grid. (b) Nomarski optical contrast micrograph of the *m*-plane GaN film surface.

Fig. 43. Atomic force micrographs of representative *m*-plane GaN film surfaces.

Fig. 44. (a) *m*-plane GaN LED electroluminescence vs. wavelength for various drive currents.
(b) Peak wavelength vs. drive current.

Fig. 45. Unpackaged *m*-plane LED output power and external quantum efficiency vs. drive current.

Fig. 46. Placement of the RCLED: (a) RCLED placed at the bottom of the epoxy cone; (b) RCLED placed inside the epoxy cone).

Fig. 47. Experimental setup used for measuring the transmitted and reflected light off the phosphor (Left: schematic of the experimental setup; Right: experimental setup).

Fig. 48. Spectral power distributions for the transmitted and reflected radiations of one phosphor-coated plate ($7mg/cm^2$).

Fig. 49. Reflected and transmitted blue and yellow energy as a function of phosphor density.

Fig. 50. Two-axis goniometer to measure beam profiles of phosphor-coated plates and LED prototypes.

Fig. 51. Normalized intensity distribution of a YAG:Ce phosphor-coated glass plate (red line) and a normalized Lambertian distribution (blue line).

Fig. 52. Schematic of SPE Package 1: the phosphor layer is embedded in the middle section of the distributing optics, as if splitting it into two pieces.

Fig. 53. Schematic of SPE Package 2: a phosphor plate is hanging below the LED/RCLED array.

Fig. 54. Schematic of the SPE Package 3: a phosphor layer is coated on top of a secondary optic.

Fig. 55. Luxeon III Star LED LightTools model and its luminous intensity distribution.

Fig. 56. Optical modeling setup (left) and ray-tracing for the setup (right).

Fig. 57. Possible designs for the secondary optic and their corresponding intensity distributions.

Fig. 58. Package A: Commercial blue LED with phosphor around the epoxy dome and a clear optic.

Fig. 59. Package B: SPE package with a commercial blue LED and phosphor coated on the optic.

Fig. 60. Profile of the commercial optic (left); the optic's ray-tracing (middle); and the optic's intensity distribution (right).

Fig. 61. Chromaticity values (left) and efficacy changes (right) as a function of phosphor density. (Source: 1-watt LED with 455 nm peak wavelength.)

Fig. 62. Efficacy for the twelve packages, SPE and typical.

Fig. 63. Light output and efficacy of the two types of LED packages as a function of current.

Fig. 64. Fixture incorporating six SPE LED packages. The micro-lens diffuser is not shown in the picture for clarity.

Fig. 65. Measured efficacy and flux for the SPE fixture.

Fig. 66. Chromaticity coordinates of the SPE fixture with and without the micro-lens diffuser.

Fig. 67. Optical modeling setup.

Fig. 68. Intensity distribution (a) traditional LED die and (b) RCLED die.

Fig. 69. Ray-tracing for the modeling of (a) traditional LED die and (b) RCLED die with 0.25-in diameter acrylic rod.

Fig. 70. Coupling efficiency as a function of rod diameter.

Fig. 71. Optical modeling setup.

Fig. 72. Intensity distributions of (a) regular LED die and (b) RCLED die immersed inside a typical epoxy dome.

Fig. 73. Ray traces for (a) regular LED die and (b) RCLED die with 0.25-inch diameter acrylic rod.

Fig. 74. Coupling efficiency as a function of rod diameter.

Fig. 75. Different general lighting configurations.

Fig. 76. The plan and view of the experimental setup.

Fig. 77. A view of the light pipe condition.

Fig. 78. Comparisons of evaluations between light pipe with downlights.

Fig. 79. Results of detailed questions.

Fig. 80. Results of probability of agreements. The green shade in the graph shows the range in which all five ratings exceeded the 70^{th} percentile.

Fig. 81. Results of clustering.

Fig. 82. Comparison of glare evaluations and UGR calculations.

Fig. 83. Comparison of UGR and subjective glare rating.

Fig. 84. Appropriate numbers of fixtures with different luminances.

Fig. 85. Lighting design tool to avoid glare.

Fig. 86. View of scale model experimental setup.

Fig. 87. Results of evaluation—perception of space.

Fig. 88. Results of evaluations—appearance of ceiling.

Fig. 89. Relative light output as a function of time for five types of high-flux LEDs at operating conditions (a) 350mA 35°C; (b) 350mA 50°C; (c)450mA 35°C.

Fig. 90. Relative light output as a function of time for high-flux white LEDs at (a) 35^{o}C and (b) 50^{o}C ambient temperature operating conditions.

Fig. 91. Light output variation as a function time for the 5-mm LED arrays in Experiment 1.

Fig. 92. Degradation rate α as a function of junction temperature for the 5-mm LED arrays in Experiment 1.

Fig. 93. Light output variation as a function time for the high-flux LED arrays in Experiment 2.

Fig. 94. Degradation rate α as a function of junction temperature for the high-flux LED arrays in Experiment 2.

Fig. 95. Light output variation as a function time for the single-die white LEDs used in the first benchmarking study.

Fig. 96. Hypothesized degradation rate α as a function of junction temperature for high-flux LEDs.

LIST OF TABLES

Table 1. Initial modeling results investigating various epoxy refractive indexes and their effect on light extraction efficiency.

Table 2. Optic efficiency and exiting rays for each optic.

Table 3. Photometric and electrical data for the twelve LEDs.

Table 4. Lighting conditions used in the experiment.

Table 5. Results of evaluations.

Table 6. Results (p-values) of ANOVAs in the first and second sessions. P-values below 0.05 indicate significance.

Table 7. Lighting conditions used in the experiment.

Table 8. Lighting conditions used in the experiment.

Table 9. Results of the evaluations.

Table 10. Parameters used to model the layout preference.

Table 11. Testing conditions for high-flux white LEDs.

Table 12. Testing conditions and estimated junction temperatures for the 5-mm LED arrays in Experiment 1.

Table 13. Testing conditions and estimated junction temperatures for the high-flux LED arrays in Experiment 2.

EXECUTIVE SUMMARY

Recently, solid-state lighting based on gallium nitride (GaN) semiconductors has made remarkable breakthroughs in efficiency, with current commercially available 'white' LEDs at greater than 20 lm/W. With further improvements to GaN-based LEDs and laser diodes (originally demonstrated by Principle Investigator Nakamura and coworkers), solid-state light source with >50% efficiency (corresponding to a luminous efficiency of 200 lm/W) are possible. GaN LEDs already surpass incandescent technology and have the potential to displace halogen and fluorescent lighting. Not only would GaN-based devices be the most efficient visible light sources, but they would be non-toxic (mercury-, phosphorus- and arsenic-free) and have projected lifetimes longer than 10 years. We have assembled a team of researchers in the Materials Department at U.C. Santa Barbara and at the Lighting Research Center (LRC) at Rensselaer Polytechnic Institute to explore the fundamental issues associated with nitride-based solid-state lighting.

The principle goal at UCSB became the demonstration of an efficient white-light emitter in the form of a GaN-based micro-cavity LED (MCLED). Although work in the first year of the project focused on vertical cavity surface-emitting lasers and ultraviolet light emitting diodes for generating white light via red-green-blue phosphor excitation, these devices required much more time for proper optimization than this project provided. Thus research emphasis shifted to blue MCLEDs in the second year. Due to their low overall device thickness, development of MCLED structures required improvements in not only film growth, but in particular post-growth processing. We found that the most viable process was to remove the (Al,In)GaN epitaxial device layer from its sapphire substrate, in a flip-chip process in which a silicon wafer supported the device. Then the device cavity was thinned using a combination of reactive-ion etching and mechanical polishing. These were critical processes, since optimal light extraction from the MCLED cavity required precise control of thickness.

In the second year UCSB also focused on the development of thick nonpolar GaN epitaxial layers and free-standing substrates. We optimized the lateral epitaxial overgrowth process for *a*-plane and *m*-plane GaN grown by hydride vapor phase epitaxy. In doing so, regions of very low dislocation density ($< 1 \times 10^6$ cm^{-2}) were obtained. In the case of *m*-plane GaN, free-standing films were obtained by spontaneous separation from their $LiAlO_2$ substrates. GaN substrates such as this (instead of sapphire) can enable back-side contacting, provide improved thermal conduction, and have reduced threading dislocation densities. An additional benefit of nonpolar substrates is the lack of electrical polarization fields in the conduction direction, which hinder the efficient recombination of electrons and holes in quantum wells. It is also theorized that nonpolar GaN p-type doping and laser gain will be superior to that in polar *c*-plane GaN devices.

In the third year of the project we developed nonpolar blue LEDs on both *a*-plane and *m*-plane GaN, which showed impressive performance for initial devices. The LEDs on *a*-plane LEO HVPE GaN benefited from lowered average dislocation density, while LEDs on free-standing planar *m*-plane HVPE GaN had the advantage of better heat extraction into the substrate. Most notably, these LEDs exhibited little or no wavelength shift with increasing drive current, which has been a persistent problem in conventional polar *c*-plane LEDs. Additionally, the optical output power was unsaturated at drive current values much higher than observed for *c*-plane LEDs.

During the first year of this project, the LRC concentrated on developing the specifications for the proposed white light source by benchmarking existing high-power white LEDs, conducting human factors studies, and completing a literature review. In addition, the LRC characterized existing encapsulants to package the short-wavelength LEDs. During the second year, the LRC conducted extensive ray-tracing analyses to study device performance, and developed secondary optics to package UCSB's light emitters. A tubular white light source was produced using a light guide in front of a commercial blue LED. The phosphor was placed remotely over the light guide to improve overall system performance.

During the second-year project review, the LRC's principle goal for the third year was established, which was to enhance efficacy by 25 percent or greater for a "white" light source from a high-efficiency blue LED compared to a commercial, high luminous efficacy white LED made from similar blue LEDs. This was to be achieved by combining a high-efficiency blue LED with a yellow YAG:Ce-based phosphor, along with optimized secondary optics and/or encapsulation material and geometry.

The LRC source modeling effort begun in Year 2 was continued by incorporating physical optics into the models, so that the modeled results agree with UCSB's light output measurement results. The objective was to identify ways to improve overall source efficacy. Further characterization of YAG:Ce phosphor material was also to be completed, including careful analysis of the phosphor's optical properties and beam-scattering properties in the forward and reverse directions. The objective was to show that at least a 25% improvement in luminous efficacy is achievable by placing the phosphor away from the die. Finally, alternate secondary optics were to be identified to create uniform radiation on the phosphor layer. The concept of making the encapsulant function as the distribution optics was to be investigated, and the better of the two candidates to be selected for a final prototype light source/fixture. A commercially available blue LED package was to be used in this task, and a prototype white light source was to be built and tested in the laboratory.

The LRC conducted a phosphor characterization study to better understand the interaction between short-wavelength light and phosphor and to quantify the amount of light reflected back to the die in a phosphor-converted white LED package. From the data gathered, the LRC estimated that at higher phosphor densities, approximately 40% of the light was transmitted through the phosphor-coated plate and the remaining 60% was reflected back toward the die. This estimate is in line with the findings of Yamada *et al.* [Yamada 2003]. Therefore, it was concluded that a packaging method is needed to help extract these backscattered photons and raise the luminous efficacy of white LEDs.

The LRC hypothesized that by placing the phosphor layer away from the die, the backscattered light could be extracted before being absorbed by the die. To explore this hypothesis, the LRC investigated options for secondary optics. Based on the simulation results and current lab capabilities, an initial prototype of the "scattered photon extraction" (SPE) package was built. The SPE package places the phosphor away from the die onto the top layer of a secondary optic. Results comparing SPE and typical white LED packages showed that the average luminous flux and the corresponding average efficacy for six tested SPE packages were 90.7 lm and 36.3 lm/W, respectively. The average luminous flux and the corresponding average efficacy for six similar commercial white LED packages were 56.5 lm and 22.6 lm/W, respectively.

A comparison study of different source forms for general illumination was conducted in two parts: an optical ray-tracing analysis and a human factors study. For the ray-tracing analysis, light from each type of LED die, RCLED and high-brightness LED (HBLED), was coupled into a light guide (rod) using two methods. With the first method, the die was totally immersed inside the rod. With the second method, the die was packaged in an epoxy dome to tailor the beam, and then this package was placed in front of the rod. Overall, the RCLED offers greater benefits when creating a linear light source compared to the traditional HBLED. The RCLED package is about 60% more efficient than the traditional LED package. For the traditional LED, maximum efficiency is reached at a diameter of 0.25 inch. With the RCLED, the rod diameter can be smaller, 0.1 inch. With the encapsulated method, it is possible to achieve similar optical efficiencies with both types of LEDs (RCLED and traditional HBLED).

The source form dictates how a light source is used in general lighting applications. Usually, tubular sources like linear fluorescent lamps have been used in fixtures that produce general, diffused light, whereas spherical sources like incandescent and compact fluorescent lamps have been used in more directional lighting fixtures, such as downlights. To understand how people react to the two types of lighting, a human factors study was conducted to understand their preferences. For this study, two experiments were conducted: a mockup experiment and a scale model experiment. The mockup experiment compared two application styles, downlight and general diffuse light from a suspended linear source (a light pipe). To understand whether people have preferences for the number of downlights in a given space, a second human factors study also was conducted. The results suggested that the light pipe condition was rated as the dimmest lighting condition and as the least appropriate condition for commercial lighting. The results also suggested that the lighting condition with 12 downlight luminous elements in the field of view was rated as the brightest lighting condition and as the most appropriate condition for office and commercial lighting. The sensation of glare was reduced as the number of luminous elements increased for a fixed total area and a fixed luminance of luminous elements.

The scale model experiment was conducted to verify the validity of the mockup study results. Here again, the results suggested that lighting conditions with 12 luminous elements were rated as the most appropriate. As the size of each element decreased while the number of downlight luminous elements increased to maintain appropriate illuminance, the room became less glaring for the same luminance. Larger luminaire spacing, which provides a more uniform illuminance distribution, may be preferred with an appropriate number of downlights.

In the area of epoxy development, efforts turned towards silicone-epoxy resins after initial studies found that simple organic resins could not be considered for LED encapsulants due to their significant yellowing at 140°C. It was reasoned that if the epoxy portion of the molecule were eliminated, it might be possible to achieve a reasonable level of thermal oxidative stability. Thus, several polydimethylsiloxane (silicone) resins were evaluated. The results were dramatic. Even after four weeks at 140°C in air, there was no observable yellowing. Polydimethylsiloxanes appear to have excellent, inherent oxidative stability. However, on long-term exposure to heat, even these resins undergo slow, degradative bond cleavage reactions. Apparently, the key to the ability of these resins to survive the screening test is due to the fact that despite this degradation, the products that are produced are not colored. Over the course of the third year, the structure of the Si-H containing oligomer has changed substantially. After a series of tests and changes, Rensselaer's Chemistry group is now confident that the chemical approach to the design of encapsulants using thermoset silicone resins for high-intensity LEDs is correct.

In the third year of the project, the LRC voluntarily continued its experimental studies from Years 1 and 2 to benchmark the performance of current LED devices. The results show that single-die green and single-die white LEDs degraded slowly, even under increased drive current and ambient temperature, whereas single-die blue and multi-die white LEDs showed the highest rates of degradation. Experiments from the life prediction study showed that the LED degradation rate changes as a function of junction temperature depending on the source of increasing heat (drive current or ambient heat). For 5-mm LEDs, rises in current-induced junction temperature have a greater effect on the degradation rate than rises in ambient heat-induced junction temperature. However, for high-flux LEDs, the ambient temperature seems to have a greater effect than the current.

INTRODUCTION AND EXPERIMENTAL

E.1 Experimental Apparatus

At UCSB, (Al,In)GaN device layers for UV as well as *a*-plane LEDs were deposited by metalorganic chemical vapor deposition (MOCVD). Specifically, single-wafer vertical close-spaced 'showerhead' deposition chambers were employed for the growth of these films. These chambers feature a showerhead for gas injection, which is a platen with alternating holes supplying group-III (*e.g.* trimethylgallium, TMG) precursors and ammonia (NH_3). The substrate upon which the film is grown is placed on a SiC-coated graphite susceptor, and is separated from the showerhead by about 1 cm. Heat is supplied by BN-coated graphite heater(s) below the susceptor, and the film surface temperature as well as film deposition rate may be monitored through one of three optical ports which extend through the showerhead platen. A pictorial schematic of a multi-wafer version of this reactor design is shown in Fig. 1. Note that the susceptor typically rotates for improved film growth uniformity.

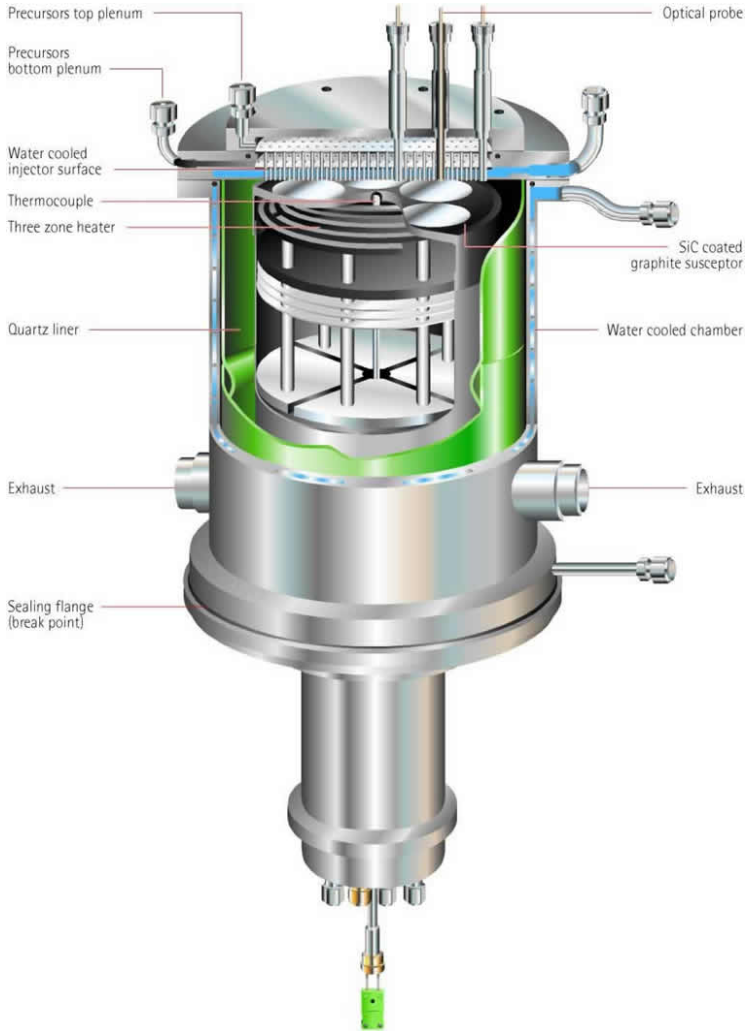


Fig. 1. Pictorial cut-away schematic of a multi-wafer close-spaced vertical showerhead deposition chamber.

(courtesy Thomas Swan Scientific Equipment Ltd.)

For film growth development of micro-cavity light emitting diode (MCLED) devices, MOCVD in a custom-designed cold-wall deposition chamber was performed. This deposition chamber incorporates a pseudo-two-flow approach, directed via a nozzle at a single 2-inch sapphire substrate held by a quartz tray. Heating is accomplished resistive BN-coated graphite heater, which can reach temperatures of over 1200°C. A typical growth procedure consists of loading a sapphire substrate, performing a hydrogen 'prebake' to clean the surface, deposition of a low-temperature (*e.g.* 600°C) GaN nucleation layer using TMG and NH_3 as precursors, followed by a high-temperature (*e.g.* 1050°C) planar GaN layer. Further device layers (*e.g.* AlGaN cladding layers, p-GaN layer) are then deposited. Pictures of this MOCVD system are shown in Fig. 2. The control panel shown in the picture at right has an integrated computer control system, in which programs (recipes) can be developed via a Microsoft Excel® environment in the computer on the left, and uploaded to the computer on the right for execution. A graphical interface allows direct control of most components in the system, including solenoid valves and mass flow controllers.



Fig. 2. Front view of MOCVD system (left) and Control Panel (right).

All device processing for LEDs discussed in the following sections was carried out in UCSB's multi-user Nanofabrication Facility, which is comprised of Class-10000 and Class-100

cleanrooms. Conventional photolithographic processes were employed, in which a photoresist (PR) such as AZ 4110 is spun onto an as-grown wafer, and is then selectively exposed to ultraviolet light through a patterned metal-on-glass mask. When the photoresist is 'developed', selected areas are removed, whereas others remain to cover the epitaxial film. Subsequently, a variety of processing steps may be carried out, such as selective dry etching by reactive-ion etching (RIE), or metal deposition in an E-beam vacuum deposition chamber. The deposition, patterning, and removal of PR may be performed multiple times depending on the complexity of the device to be fabricated.

The hydride vapor phase epitaxy (HVPE) lateral overgrowth studies were performed in a hot-wall quartz horizontal-flow reaction chamber. This system provides Ga to the growing GaN film via a gaseous HCl flow over liquid Ga upstream of the reaction zone, which creates $GaCl_x$. As in MOCVD, NH_3 serves as the N source for the film. The growth temperature range is similar to that used in MOCVD (1000-1100°C), but heating is provided by a split-shell furnace design. A picture of this HVPE system is shown in Fig. 3.

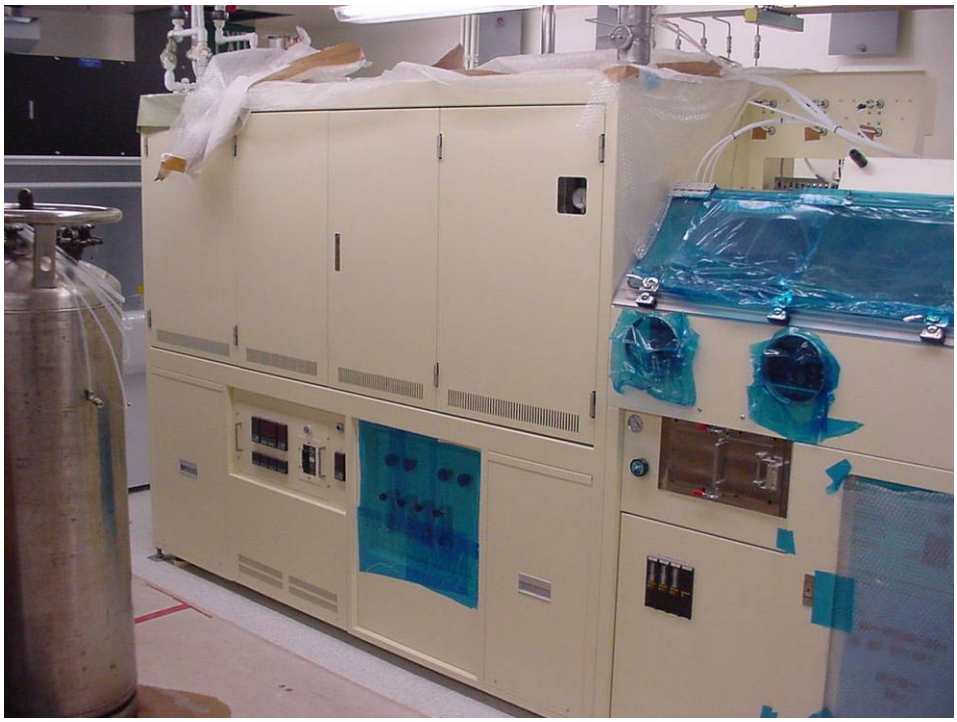


Fig. 3. Front view of HVPE system shortly after move-in and installation.

As described in subsequent sections, UCSB has begun fabrication and testing of resonant-cavity and microcavity LEDs. If these LEDs operate as intended under current injection, the intensity of the emitted light should have a strong directional (angular) dependence, due to mode formation in the LED cavity. To measure this effect, we have constructed a simple computer-controlled measurement setup, shown below in Fig. 4. Via the use of an aperture and collimation lens on a moveable arm, this setup enables angular-dependent intensity measurements, which are useful in determining whether an RCLED is performing as designed.

For increased MCLED light extraction efficiency, we plan on fabricating etched-in photonic crystal structures in the periphery around the device active region. An ideal tool for our initial photonic crystal studies is the focused-ion beam etching apparatus at UCSB, a picture of which is shown in Fig. 5. The FEI DB235 is small-stage system combining a Hexalens electron column and a Magnum ion column. A Schottky emitter is used for scanning electron microscopy from 200 – 300 kV, while Gallium liquid metal is used for the focused ion beam (FIB) operating at 5 to 30 kV in a current range of 1pA to 20 nA. 3D imaging can be carried out by using these two beams arranged in 52°-tilt angle. The resolution is 3 nm for SEM and 7 nm for FIB.

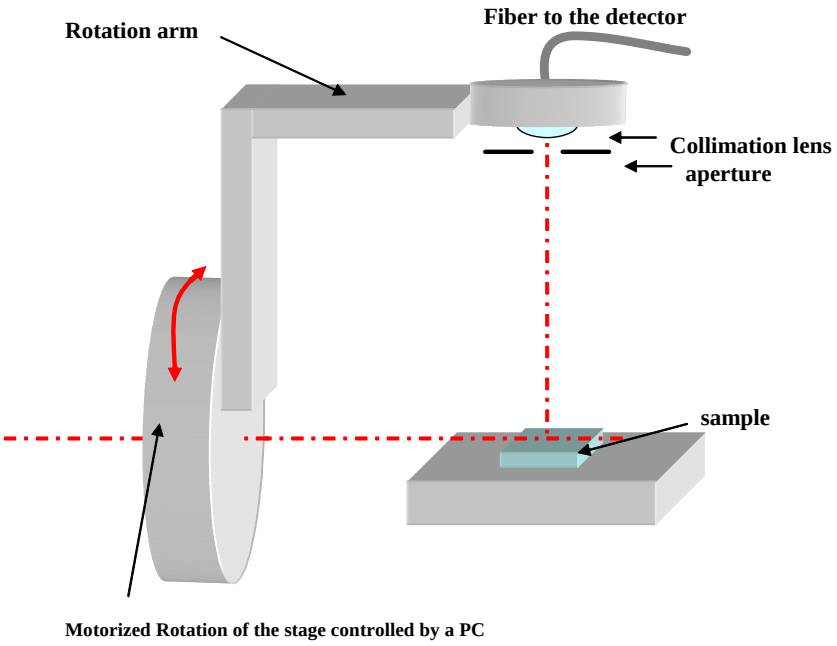


Fig. 4. Schematic of angular measurement system for RCLED testing.



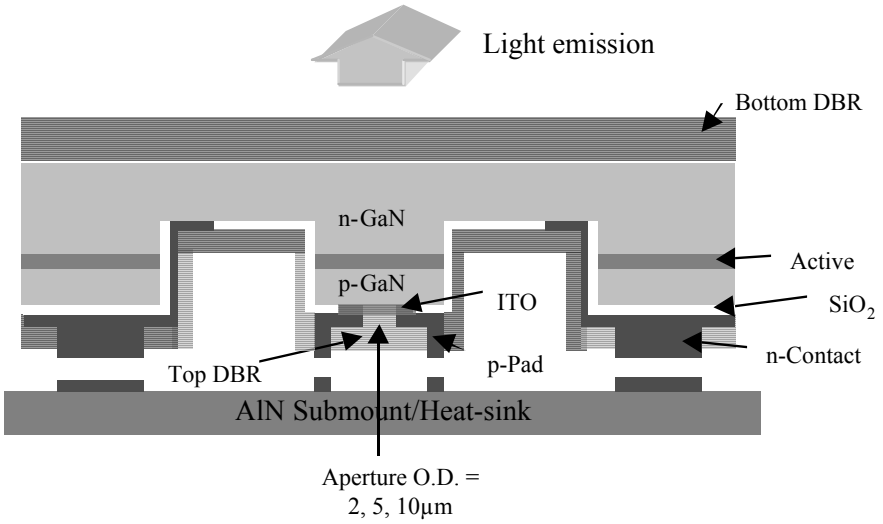
Fig. 5. Picture of FEI focused-ion beam etching system.

E.2 Vertical Cavity Surface Emitting Laser (VCSEL) Fabrication

Two approaches were explored in the VCSEL device design. In the first, the devices were fabricated using a two top contact scheme, with indium tin oxide (ITO) as the transparent p-contact. The ITO was deposited by DC magnetron sputtering in an oxygen ambient, then annealed at 500°C for 3 minutes to achieve transparency. An 11.5 period Ta_2O_5/SiO_2 dielectric mirror (R > 99.5%) was deposited at 250°C on the contacted side, followed by flip-chip bonding of the devices onto an AlN submount. The sapphire substrate was then removed via laser-assisted debonding. Finally, the now-upturned GaN:Si was polished and a second 11.5 period DBR was deposited to form a 6 um thick cavity.

In the second design, the samples were implanted with 180 keV aluminum ions in doses of 10^{13}, 10^{14}, and 10^{15} cm^{-2} prior to device fabrication, followed by a regrowth of 1230Å of GaN:Mg. The current confinement provided by the ion implantation allowed for the use of a ring-shaped ohmic metal p-contact (instead of ITO). Otherwise, the device fabrication remained the same.

Figure 6 presents a cross-section schematic of the ITO-contacted device structure, as well as an SEM micrograph of a diode just prior to flip-chip bonding. While the end design is somewhat different than traditional GaAs or InP based VCSELs, the overall objective is the same: to minimize the losses in a cavity with a short gain medium so that the lasing threshold can be reached. This minimization is far more critical in a VCSEL as compared to an edge-emitting LD -- Fig. 7 illustrates this point. The short amplification length (*i.e.* small per-pass gain) requires that losses such as transmission through the mirrors, absorption in contacts, and scattering from rough interfaces be much smaller than those tolerable in edge-emitting LDs. Of course the gain can be increased through higher current injection, but only to a point, after which heating effects dominate.



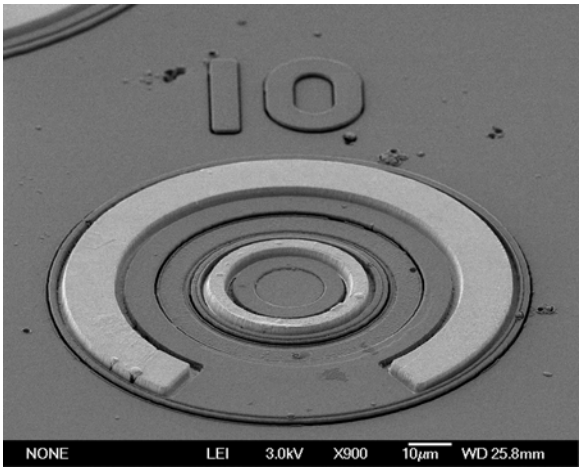


Fig. 6. Cross-section device schematic (above) and a SEM micrograph (below) of a 10 μm aperture device prior to flip-chip bonding.

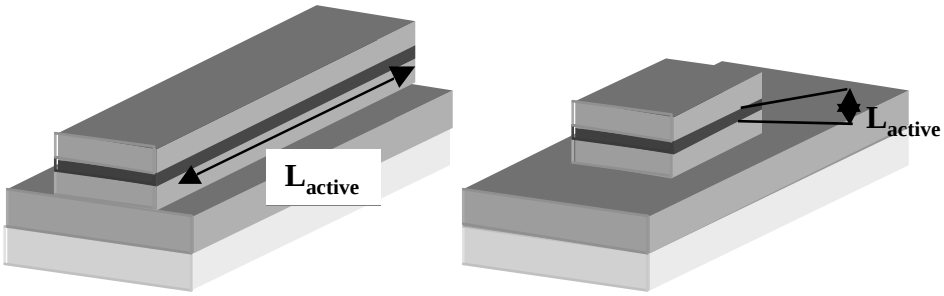


Fig. 7. Illustration of gain-length difference between edge-emitter and VCSEL.

Figure 8 details the layer structure of the device presented in Fig. 6, grown by metalorganic chemical vapor deposition (MOCVD) on double-side polished sapphire substrates. Typically, the films consist of 5 μm of GaN:Si (with an optional insertion of 1000Å of InGaN:Si), five to ten 40Å $In_{0.1}Ga_{0.9}N$ wells separated by 80Å $In_{0.03}Ga_{0.97}N$:Si barriers, a 200Å $Al_{0.2}Ga_{0.8}N$ electron-barrier layer, and 5000Å of GaN:Mg.

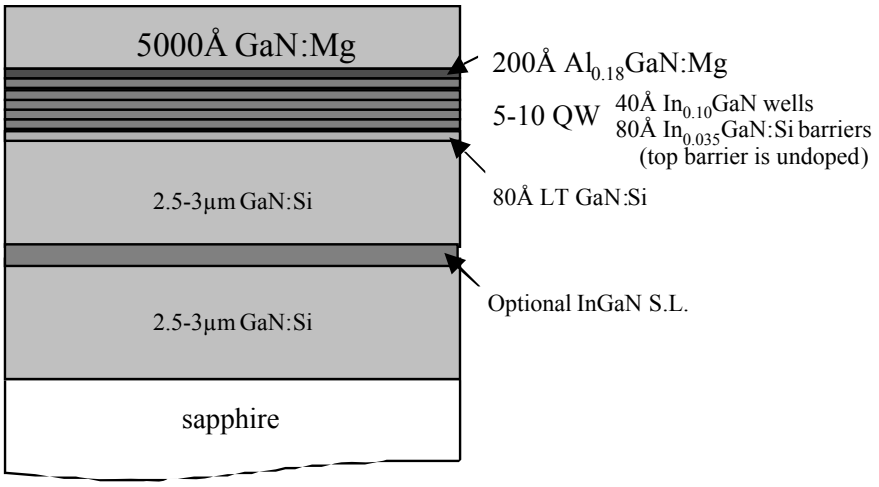


Fig. 8. MOCVD layer structure for the device in Fig. 6.

Our later efforts in the development of electrically pumped GaN-based VCSELs focused on the use of GaN lateral epitaxial overgrowth (LEO). In this process, a planar 'seed' GaN film of 2-3 µm thickness is coated with a mask material such as SiO_2, which is then typically etch-patterned with periodic stripe openings in a specific crystallographic orientation. When GaN regrowth on this patterned mask is performed, the material grows laterally from these openings, and the resulting 'wings' have threading dislocation densities that are 3-4 orders of magnitude lower than the 'window' regions directly above the openings. Once sufficient LEO GaN is deposited to coalesce wings from neighboring stripes, a device structure such as that for a VCSEL may be grown. We at UCSB have demonstrated that the (opto)electronic device performance benefits from placement on the high-quality overgrown wings vs. on the dislocated windows. In particular, our edge-emitting lasers on LEO material had a lower threshold current density and a higher external differential efficiency than those on typical planar GaN films.

Based on our success with edge-emitting lasers on LEO GaN, we began the fabrication of VCSELs on LEO GaN underlying layers. In Fig. 9 below, the alignment of as-processed devices is shown schematically as well as pictorially. As in our previous demonstrations, we intentionally aligned devices in three different areas: dislocated windows, dislocation-free wings, and coalescence regions between neighboring stripes. In so doing, we demonstrated the effectiveness of LEO for improving device performance in an internally consistent manner. There are still some important processing steps to be done before the VCSELS can be tested: we remove the film from its sapphire substrate via excimer laser lift-off, thin the underlying GaN template with RIE etching (as shown in Fig. 9), and finally deposit a dielectric Bragg mirror stack on the backside of the thinned GaN. From this point we have fully completed device structures which will be tested at room temperature under pulsed conditions.

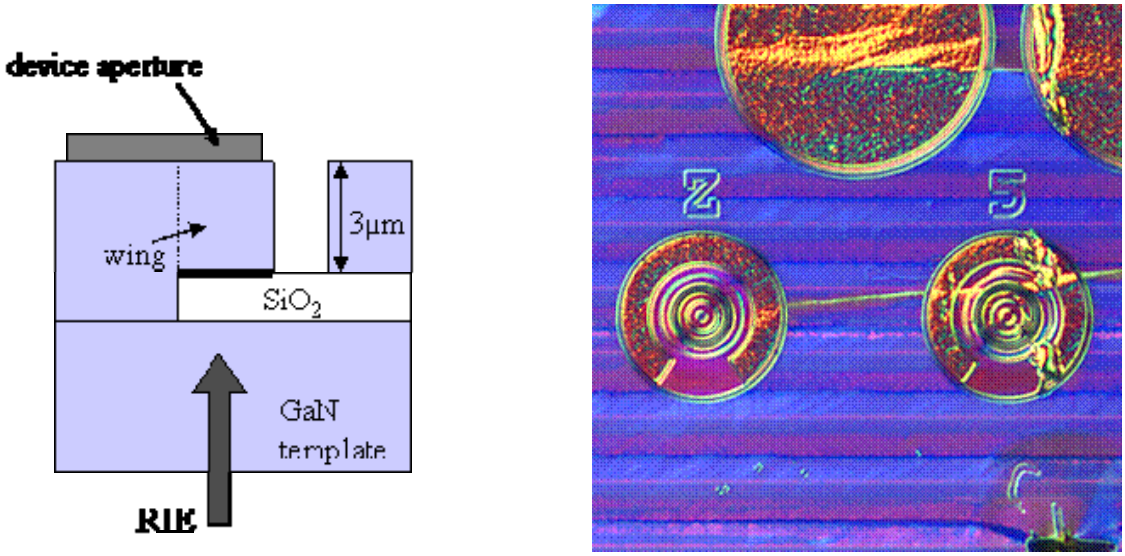
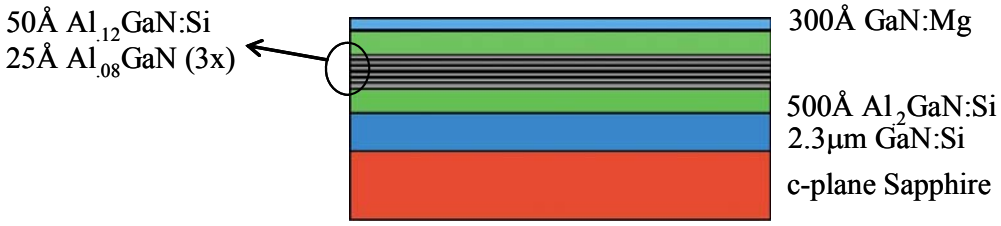


Fig. 9. Side-view schematic of VCSEL cavity position relative to LEO stripe (left), and optical micrograph of fabricated VCSELs on a coalesced LEO film (right).

E.3 Ultraviolet LED Growth and Fabrication

In the development of an LED emitting at ~ 340nm (with the ultimate goal of laser emission at this wavelength), we have begun growth and fabrication of UV LEDs with $Al_xGa_{1-x}N$ active regions, where x is typically 10%. By immediately pursuing the more difficult goal of electrical pumping (vs. optical pumping), we hope to identify the key challenges to the development of an electrically pumped 340 nm laser. Specifically, our approach has been to deposit multi-quantum well (MQW) structures by MOCVD. We have considered two structures: quantum wells with a 'bulk' AlGaN cladding, as well as short-period superlattice (SPASL) cladding. Both structures were grown on a ~ 2 μm GaN 'template' layer on 2" sapphire substrates. Schematics of both of these structures are shown below in Fig. 10. The active regions of the bulk-clad and SPASL-clad LEDs both had 3- and 5- period MQWs, which consisted of $Al_{0.07\text{-}0.08}GaN$ wells and $Al_{0.12}GaN$ barriers.



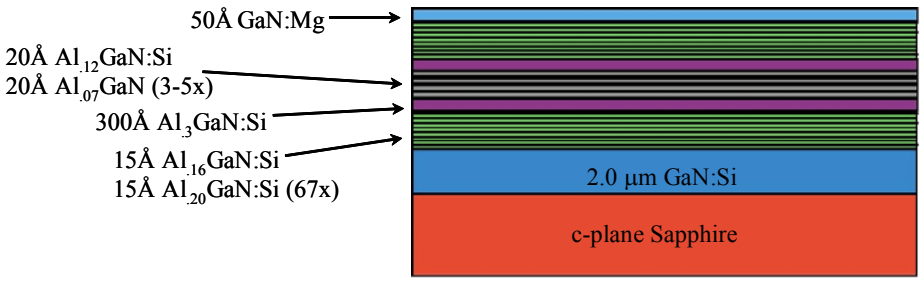


Fig. 10. Schematics of the structures of UV LEDs with 'bulk' (top) and 'SPASL' (bottom) cladding layers.

Once grown, these films were processed into a 'conventional' LED test geometry by using chlorine Reactive Ion Etching (RIE) to define mesas. A dual top-contact scheme was used: Ti/Al/Ni/Au n-type contacts and Pd/Au p-type contacts were deposited by e-beam deposition. All intermediate steps were performed using conventional photolithography in our cleanroom.

Testing was performed in a direct-current (DC), un-pulsed mode up to a current of 100mA with a Hewlett-Packard 4145B Parameter analyzer. At present, this test equipment is limited to 100mA, so higher currents were not investigated. The light emitted from the **top** side of the devices was collected with a UV-enhanced photodiode located approximately 7mm above the wafer. The collection at this distance is about 20% of a total sphere. Spectra were obtained by coupling light into a fiber (located about 15mm above the sample) connected to a spectrometer.

E.4 RCLED and MCLED Development

A resonant-cavity light emitting diode (RCLED) consists of an optically active light-emitting region appropriately positioned within a Fabry-Perot cavity, such that the emission from the active region is in resonance with the cavity modes of the structure [Schubert 1992]. RCLEDs demonstrate several enhancements in performance compared to conventional light emitting diodes (LEDs); they show enhanced directionality, extraction efficiency, and spectral purity. In order for a resonant cavity to be within the 'micro-cavity' regime, the effective cavity length must be such that it is short enough to permit only one mode to lie within the extraction cone of the device [Benisty 1998]. A device operating within the micro-cavity (MC) regime will exhibit an additional improvement in extraction efficiency.

The objective of this work was to design and fabricate a general-purpose high efficiency nitride-based MCLED that emits in the 500-525 nm wavelength range. A GaN-based micro-cavity device that emits in this wavelength range has potential applications not only in solid-state lighting, but also as light sources in plastic optical fiber data transmission.

The device design discussed in this report differs from those of other studies [Shaw 2002, Calle 2002, De Mierry 2002, Shaw 2004] in that we did not employ an epitaxial distributed Bragg reflector (DBR). Figure 11 shows a schematic of the as-grown structure, and Fig. 12 shows a schematic of the final fabricated device structure. The MCLED device design and the fabrication process that we employ are similar to those described by us in a previous report [Fujii 2004]. In this design, the cavity is bound by a silver mirror (with a nickel interlayer) with an effective reflectivity $R_1 \cong 80\%$ on one side and the GaN/air interface with a reflectivity $R_2 \cong 17\%$ on the other side, as shown in Fig. 12. In order to fabricate this cavity, the epitaxial

material is subjected to a flip chip process wherein the sapphire substrate is removed by laser lift-off, and the desired cavity length is attained through cavity thinning by reactive ion etching of the exposed nitrogen-face GaN surface. This design and process was chosen to overcome the difficulty involved in the crystal growth of epitaxial DBRs in this material system, and in order to achieve the shortest cavity length possible. The penetration of the optical wave into a DBR increases the effective cavity length and consequently affects the extraction efficiency of the micro-cavity device [Benisty 1998].

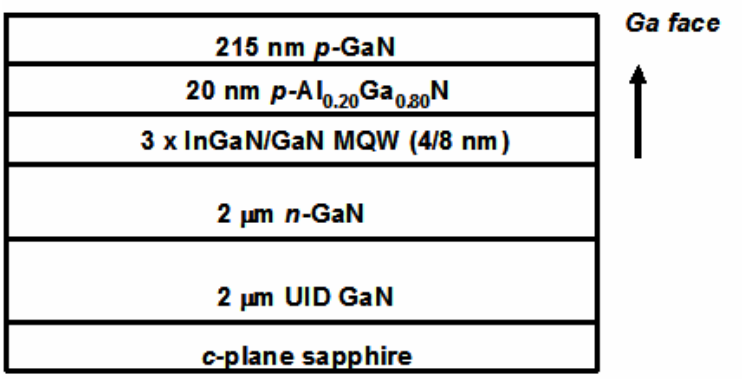


Fig. 11. Schematic of MCLED epitaxial thin film structure.

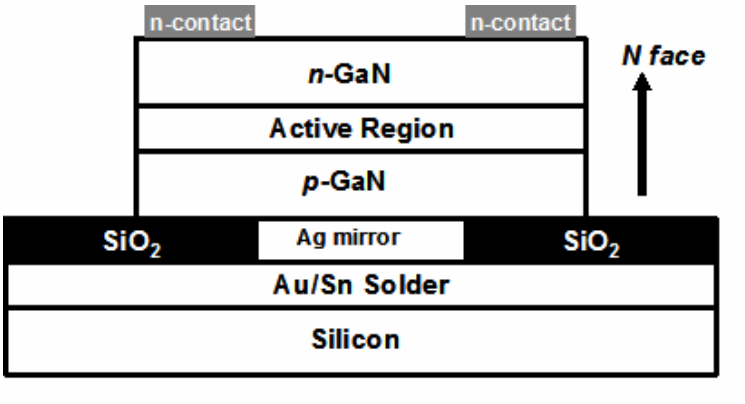


Fig. 12. Schematic of processed MCLED device structure.

The epitaxial material for our device was grown by metalorganic chemical vapor deposition (MOCVD) on a *c*-plane sapphire substrate. The active region consisted of a 3-period InGaN/GaN (4nm/8nm) multiple quantum well structure. The design and structure of the active region were based on a compromise between the requirement of high brightness and the simultaneous requirement of a compact emission region. The thickness of the active region from the beginning of the first quantum well to the end of the third quantum well was 28nm, which was significantly less than $\lambda/4n$, thus ensuring that all of the quantum wells could be positioned at or near the anti-node of the standing optical wave. The placement of the active region with respect to the silver mirror is another critical design parameter for maximum extraction efficiency [Shaw 2004]. The target thickness of the *p*-GaN layer in our sample was chosen so as to place the center of the active region at the third anti-node of the standing optical wave, approximately 250nm from the silver mirror.

The process used to fabricate the epitaxial film into a current-injected MCLED was as follows. The *p*-type GaN layer was activated by rapid thermal annealing in a nitrogen/oxygen

environment. Emission regions were defined by patterning SiO_2 to create current apertures on the surface of the material. A silver mirror that also served as an electrical contact was then deposited within the defined current apertures. A 1 nm nickel interlayer was employed to improve cohesion of the silver mirror to the GaN surface. Prior to laser lift-off from the sapphire substrate, the gallium surface of the material was bonded to a conductive silicon carrier wafer, using a Sn/Au solder. The sapphire substrate was removed using a KrF (248nm) excimer laser that dissociated the GaN into gallium and nitrogen at the sapphire/GaN interface [Fujii 2004]. The GaN layer was then thinned using a carefully timed reactive ion etch in a chlorine environment. After etching, the surface of the sample was smoothed to an RMS roughness of less than 1 nm, using a chemical-mechanical polish with colloidal silica. Mesas were defined using another reactive ion etch step in order to isolate individual devices, and ring contacts were deposited to contact the *n*-GaN. The mesa height was determined by profilometry and scanning electron microscopy to be approximately 830 nm, corresponding to roughly $4 \times \lambda$ at the peak emission wavelength. The conductive silicon sub-mount was used to contact the *p*-GaN.

E.5 A-plane GaN Lateral Overgrowth by HVPE

Since bulk GaN crystals of appreciable size are not yet available, hydride vapor phase epitaxy (HVPE) has been used to heteroepitaxially grow thick (10-300+ μm) *c*-plane GaN films to serve as homoepitaxial pseudo-substrates for subsequent device growth by molecular beam epitaxy (MBE) and MOCVD. Recently we reported on the first successful growth of planar $(11\bar{2}0)$ *a*-plane GaN by HVPE, demonstrating the potential for fabrication of non-polar GaN substrates. These films described exhibited defect densities comparable to those of heteroepitaxially grown *c*-plane films. However, ideal GaN substrates would be essentially free of threading dislocations, stacking faults, and macroscopic defects that could affect the quality of the device layers subsequently regrown upon them.

As mentioned above, LEO has been demonstrated to be an effective approach for the reduction of threading dislocation densities in *c*-plane GaN by both MOCVD and HVPE. LEO performed by MOCVD has yielded similar threading dislocation reduction in *a*-plane GaN films. In this report we demonstrate defect reduction in HVPE-grown *a*-plane GaN films via LEO.

The masks for the LEO process were prepared by utilizing conventional photolithographic processing and wet etching on ≈ 1300 Å-thick PECVD SiO_2 layers. A variety of mask designs were investigated, including arrays of circular apertures, parallel stripes oriented along the [0001] direction, parallel stripes oriented along the $[10\bar{1}0]$ direction, and non-parallel stripes in a 'wagon-wheel' pattern. The LEO growth process was carried out in a conventional three-zone horizontal directed-flow HVPE system, identical to the system used previously for the growth of planar a-plane $(11\bar{2}0)$ GaN films on *r*-plane sapphire substrates. Typical vertical growth rates ranged from 16 to 40 μm/hr at a substrate temperature of ~ 1040°C. A variety of mask geometries yielded coalesced films; in particular the use of masks consisting of periodic arrays of $[10\bar{1}0]$-oriented stripes allowed full 2-inch diameter *a*-plane GaN wafers to be coalesced.

E.6 A-plane LEDs on HVPE LEO Templates

In previous reports we described the successful growth of planar $(11\bar{2}0)$ *a*-plane GaN by HVPE, demonstrating the potential for fabrication of non-polar GaN substrates. These films exhibited defect densities comparable to those of heteroepitaxially grown *c*-plane films.

However, ideal GaN substrates would be essentially free of threading dislocations, stacking faults, and macroscopic defects that could affect the quality of the device layers subsequently regrown upon them. Lateral epitaxial overgrowth (LEO) was demonstrated to be an effective approach for the reduction of threading dislocation densities in *a*-plane GaN grown by HVPE.

These *a*-plane LEO GaN templates were used in the regrowth of nonpolar LEDs. The LED structure was regrown by MOCVD on a 10-µm-thick reduced-dislocation density *a*-plane GaN LEO template. The mask for the LEO consisted of parallel 8-µm-wide SiO_2 stripes separated by 2-µm-wide window openings oriented parallel to the GaN <11$\underline{2}$0> direction. MOCVD device layer growth consisted of a 2.2 µm Si-doped n-GaN base layer with an electron concentration of 2×10^{18} cm^{-3}, followed by the active region, which consisted of a five period MQW stack with 16 nm Si-doped GaN barriers and 4 nm $In_{0.17}Ga_{0.83}N$ QWs. A 16 nm undoped GaN barrier separated the active region from the 0.3 µm Mg-doped p-type GaN layer, with a hole concentration of 6×10^{17} cm^{-3}. The structure was capped with a 40 nm p^+-GaN contact layer. See Fig. 13 for a schematic of the entire device structure. The as-grown samples were investigated by optical microscopy and photoluminescence (PL) measurements. 300 x 300 μm^2 diode mesas were defined by chlorine-based reactive ion etching. Pd/Au (3/200 nm) and Al/Au (30/200 nm) were used as p-GaN and n-GaN contacts, respectively. The electrical and luminescence characteristics of the diode were measured by on-wafer probing of the devices. The I–V measurements were performed with a Hewlett-Packard 4155B semiconductor parameter analyzer. Relative optical power measurements under dc conditions were obtained from the backside emission through the sapphire substrate onto a calibrated broad area Si photodiode. The emission spectrum and the optical power emission of the LEDs were measured as a function of drive current, and all measurements were carried out at room temperature.

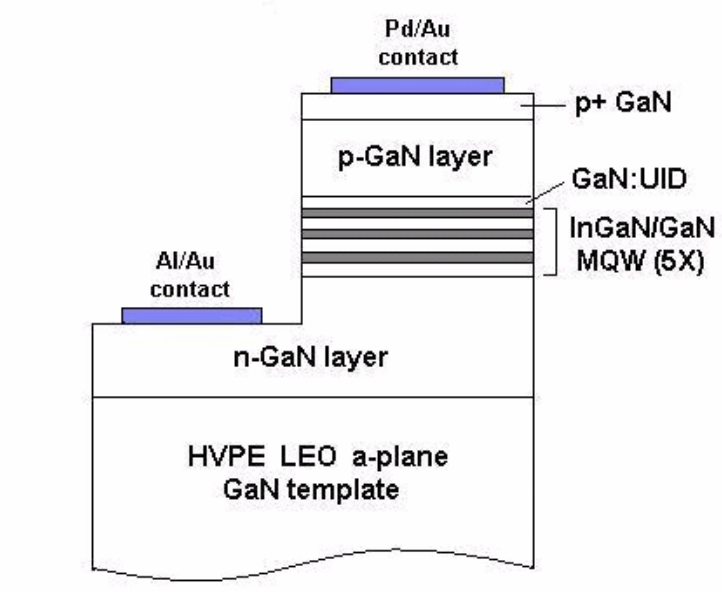


Fig. 13. Schematic of blue LED device structure on *a*-plane LEO GaN template.

E.7 M-plane LEDs on Free-Standing HVPE GaN

The *m*-plane HVPE GaN films were grown in a conventional three-zone horizontal hydride vapor phase epitaxy reactor. Double-side polished two inch diameter (100) γ-$LiAlO_2$ substrates

were loaded directly into the growth chamber without any *ex situ* cleaning. The *m*-plane GaN films were grown directly on the lithium aluminate substrates without the use of any low-temperature buffer or nucleation layers. GaCl, formed by the *in situ* reaction of purified HCl and 7N purity metallic Ga, was combined with purified NH_3 8-20 mm from the substrates, with V/III ratios between 10 and 60. The growth rate of the *m*-plane GaN films varied from 30 to 240 μm/hour, and films up to 250 μm thick were grown at substrate temperatures between 860 and 890°C.

The nonpolar LED structure was grown by MOCVD on 250 mm thick free-standing *m*-plane HVPE GaN substrates. The device structure, shown in Fig. 14, consisted of a 2.2 μm Si doped n-type GaN base layer with an electron concentration of 2 x 10^{18} cm^{-3}, followed by the active region, which consisted of a 5 period MQW stack with 16 nm Si-doped GaN barriers and 4 nm $In_{0.17}GaN$ quantum wells. A 16 nm undoped GaN barrier separated the active region from the 0.3 μm Mg-doped p-type GaN layer with a hole concentration of 6 x 10^{17} cm^{-3}. A 40 nm p^+ GaN layer was used to cap the structure for improved electrical contact to the p-GaN layer. The as-grown samples were investigated by optical microscopy and room temperature photoluminescence measurements. 300 x 300 μm^2 square diodes were defined by chlorine-based reactive ion etching. Electron beam deposited Pd/Au (20/200 nm) and Al/Au (30/300 nm) were used as p-GaN and n-GaN contacts, respectively. The electrical and luminescence characteristics of the diode were measured by on-wafer probing of the devices. The I-V measurements were performed with a Hewlett-Packard 4155B semiconductor parameter analyzer. Relative optical power measurements under direct current (dc) conditions were obtained from backside emission through the GaN substrate onto a calibrated broad area Si photodiode.

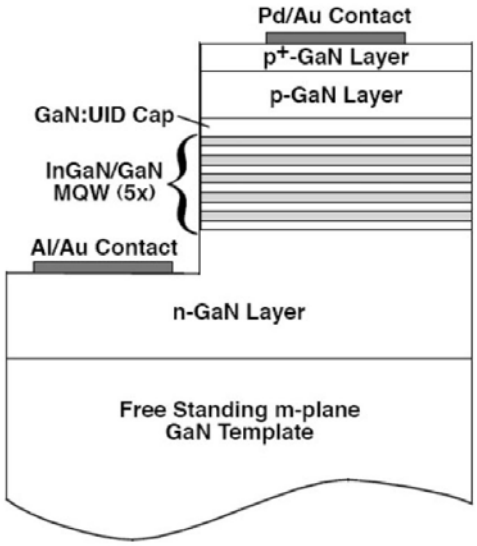


Fig. 14. Schematic of *m*-plane GaN LED on free-standing *m*-plane HVPE GaN template.

E.8 Source Modeling

The goal of this task was to optimize the chip shape and package design and to increase the light extraction efficiency of the resonant-cavity light-emitting diode (RCLED). Last year, the LRC investigated the impact of RCLED aperture size, internal emission pattern, and the shape of the encapsulant on the light extraction efficiency of the RCLED using LightTools™, a commercial ray-tracing software. This year, the LRC continued these efforts to model the

RCLED and improve source efficacy; specifically, the LRC studied how source wavelength, index of refraction of the encapsulant, and die placement within the encapsulant affect source efficiency. The light source structure and its physical properties were obtained from UCSB and were built into the LightTools model.

E.9 Phosphor Characterization and Secondary Optics Studies

The most common method for creating white light from LEDs is to apply a layer of cerium doped yttrium aluminum garnet (YAG:Ce) phosphor over a gallium nitride (GaN) based blue LED [Nakamura 1994]. Typical commercial white LEDs are packaged with the phosphor embedded inside an epoxy resin that surrounds the LED die. While these products provide sufficient white light for use in certain niche illumination applications, many are not suitable for general illumination applications because of their low overall light output and low luminous efficacy.

To achieve higher luminous efficacy from white LEDs, improvements are needed at several levels, including internal quantum efficiency, extraction efficiency, and phosphor-conversion efficiency. Because much is already being done in these fields, the LRC considered other approaches to improving white LED efficacy from a packaging standpoint. Past literature [Yamada 2003, Narendran 2004, Narendran 2005] shows that a significant portion of the light emitted from the die is backscattered by the phosphor and absorbed within the LED, but to the best of our knowledge no one to date has attempted to improve performance by capturing and extracting these backscattered photons.

The goal for this study was to understand the packaging issues that affect the efficacy of an LED light source, and to develop a high-efficacy, reliable white light source using UCSB's RCLED devices. As described in the second-year report, placing the phosphor layer close to the RCLED die is not ideal because light can be scattered by the phosphor, which negatively affects performance in terms of luminous efficacy and life. To quantify the amount of light scattered by the phosphor, a laboratory study was conducted in which several glass plates were coated with YAG:Ce phosphor. These plates were coated by OSRAM SYLVANIA (Dr. Madis Raukas). In this study, a dual integrating sphere setup was used to capture and measure the forward and backward scattered light from the phosphor. Based on results that showed significant backscattering of photons, a method was developed to capture these photons to increase overall system efficiency. The LRC created a scattered photon extraction (SPE) method that allows the phosphor layer to be moved away from the die, preventing light feedback into the RCLED. At the same time, the package captures both the transmitted and reflected components to significantly improve system efficiency. Prior to constructing the initial prototype devices, an optical modeling study and a series of lab tests were conducted to identify the optimum system components. The overall goal was to demonstrate that by placing the phosphor remotely and capturing and extracting the backscattered light, the overall light output and efficacy of the source can be increased by at least 25%.

E.10 Understanding Source Form Factors for General Illumination

General illumination is one of the target applications for solid-state light sources such as LEDs. Based on the second-year project results, it may be advantageous to package the RCLEDs into tubular light source shapes, similar to a linear fluorescent lamp.

The two most commonly used light sources in general illumination applications are incandescent and fluorescent. In commercial spaces, incandescent-based light sources are commonly used in recessed downlights, and linear fluorescent light sources are used in recessed troughs (*e.g.*, 2 ft. by 4 ft.) and suspended direct/indirect fixtures. One of the strengths of LED technology is that it can be formed into any shape, including hemispherical and tubular shapes that resemble traditional light sources. Therefore, given the option, the question is which shape is better suited for the RCLED developed by UCSB.

To address this question, the LRC conducted two studies: an optical ray-tracing analysis to study light source efficiency, and a human factors evaluation to understand how people liked or disliked the lighting.

E.11 Development of LED Encapsulants

As solid-state lighting moves toward general lighting applications that require high-intensity white light LED sources, the plastic packages used for these LEDs are more and more a critical factor in their overall performance. The LED elements, like any semiconductor device, absolutely require protection from environmental exposure and mechanical damage for their operation. This is most often accomplished today through the use of plastic encapsulants. Such encapsulants are thermoset materials of moderate viscosity that are thermally polymerized around the LED device. It is crucial that the encapsulant flow freely so that even the most delicate structures and wire bonds in the electronic device be preserved during encapsulation. Such plastic packages have other functions besides providing environmental and mechanical isolation. For example, the encapsulant often is cast in such a manner that it serves as a lens to focus the emitting light out of the package in a specific direction. Semiconductor encapsulants are oftentimes opaque materials, while LED encapsulants must be optically transparent and maintain that transparency over the life of the LED. Further, the plastic package must undergo no degradation leading to color formation that will shift the color of the emitted light. One of the most promising schemes for generating high-intensity white LED light is to employ devices that emit in the UV region. Conversion to visible white light is accomplished with the use of phosphors emitting in the visible region. Yellowing upon exposure to UV light is a very common problem with many types of organic polymers. This is unacceptable for high-brightness LED applications.

Currently, most LEDs are packaged using epoxy thermosetting resins. Such resins are very attractive due to their convenient processing characteristics and their ready, commercial availability. However, these materials display very pronounced yellowing characteristics on long-term exposure to light and heat. These characteristics will be further exacerbated in high-intensity LEDs due both to the anticipated increase in light flux as well as the higher operating temperatures. In addition, most advanced LED sources will emit in the UV region. The degradation and yellowing of epoxy encapsulants is markedly accelerated in the presence of UV light. To date, there is no acceptable plastic encapsulant material suitable for high-intensity white light-emitting LEDs. Such encapsulants are expected to maintain their properties without change over an operating lifetime of 100,000 hours or longer. For this reason, the current program has

been mounted to identify and evaluate alternative packaging materials. Finding such a material is absolutely critical to the eventual successful application of high-intensity white light emitting LEDs. Along with the other materials' properties mentioned above that are required for LED encapsulants, there are a number of processing characteristics that must also be met by any novel, prospective encapsulant. These characteristics are determined by current industry practice employed for the present, commercially used epoxy encapsulants. For example, the encapsulant must be processed by batch casting on live devices and cured over several hours in forced-air ovens at moderate temperatures. Lastly, the encapsulant should be composed of readily available, bulk materials and be cost-effective.

E.12 Benchmarking Current, State-of-the-art LED Devices

Over the past three years, the LRC conducted a benchmarking study to characterize the performance of currently available, commercial high-power LEDs. The purpose of this study was to eventually compare the commercial devices with those being developed in the scope of this project. One component of the benchmarking study was to investigate long-term performance issues. Arrays of LEDs were mounted inside individual life-test thermal chambers, which were designed and built by the LRC and housed in a temperature-controlled lab. The test chambers had two functions: 1) to keep the ambient temperature constant, and 2) to act as light-integrating boxes for measuring photometric parameters. These parameters include light output, luminous efficacy, and color properties (CIE *x,y* values), which were continually measured and evaluated as a function of time. Five types of commercial high-flux LEDs were selected for testing: red, green, blue, and single-die white LED packages, and a multiple-die white LED package. LED arrays for each type (a total of 15) were powered on for a life test on January 3, 2003. The LEDs were seasoned for 500 hours and then tested for initial light output and other relevant photometric and electrical characteristics. The LED arrays were tested for 10,000 hours at three different operating conditions: 350 mA and 35°C; 350 mA and 50°C; and 450 mA and 35°C.

Since the benchmarking study began, several LED manufacturers have released new types of commercial high-power LEDs. The LRC put these devices to a life-test as well at two common ambient temperatures: 35°C and 50°C. The performances of the different devices were compared at similar operating conditions.

Additionally, the LRC investigated the effects of ambient temperature and drive current on LED light output depreciation. Both parameters contribute to the junction temperature of the LED, which is known to be a good predictor of LED life. Therefore, to understand how the different LED packages are affected by these parameters, LED arrays were tested at different operating conditions using either the same current but different ambient temperatures, or the same ambient temperature but different currents. Eventually, this information will be useful in developing a life predictor that can reduce the need for time-consuming life tests. The details of these life tests were published in the 2004 SPIE Proceedings [Gu 2004].

RESULTS AND DISCUSSION

R.1 Vertical Cavity Surface Emitting Laser (VCSEL) Fabrication

The completed VCSEL devices were pulse-tested at room temperature, applying voltage pulses ranging from 50 to 500 nsec at both 5 and 10 kHz. A HP 8114A pulse generator was used as the injection source. Light emission from the devices was uniform over the aperture area, indicative of current spreading by the ITO contact. A 100 μm diameter multimode fiber-optic probe was used to collect and guide the light into a Hamamatsu photomultiplier tube (PMT), biased at 900-1200 V.

Light output versus current (L-I) and current-voltage curves (I-V) for a 10 quantum well (QW), 10 μm diameter aperture device with an ITO contact are shown in Fig. 15 for varying pulse lengths.

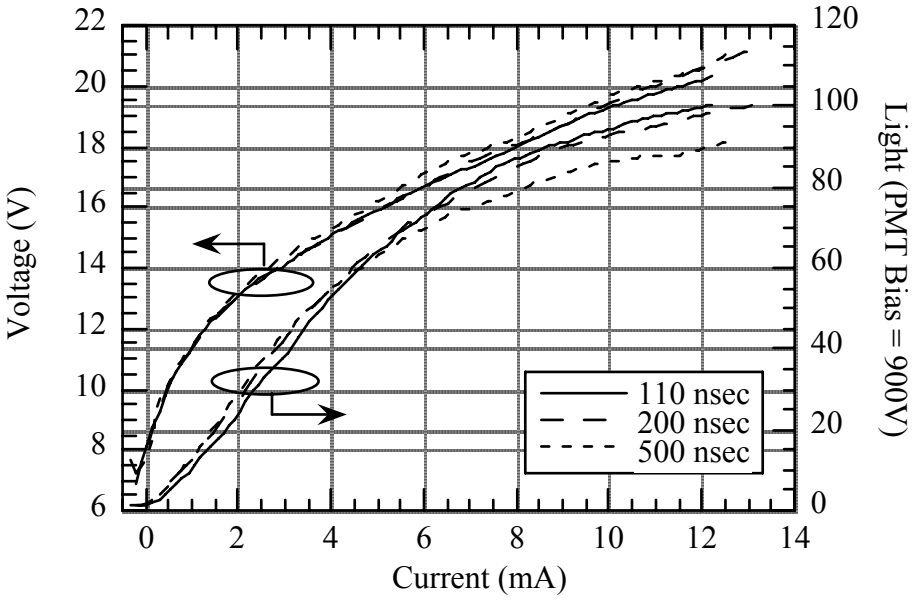


Fig. 15. L-I-V characteristics for a 10 μm aperture 10 QW device with an ITO contact, pulsed at 5 kHz with varying pulse widths.

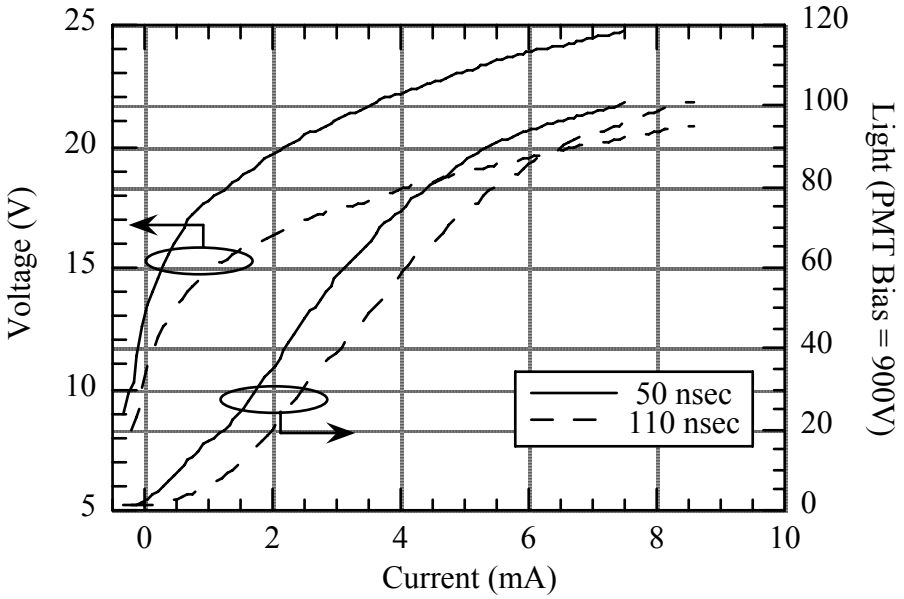


Fig. 16. L-I-V characteristics for a 10 μm aperture 10 QW device with an ITO contact, pulsed at 5 kHz.

The turn-on voltage that is a result of the Schottky ITO contact is approximately 12–15 V, although higher at 50 nsec pulse lengths (Fig. 16). The L-I characteristics tail off at higher current densities indicating that the devices are heating up during the pulse. As expected, this tail-off occurs at lower currents for longer pulses. A slight bend in the L-I at low currents (< 2 mA) is probably indicative of non-radiative trap saturation. Reducing the number of QWs from 10 to 5 did not significantly alter device performance (Fig. 17).

Radiative performance scaled with aperture size, although I-V characteristics did not (Fig. 18). Smaller devices seemed to handle much larger current densities (up to 220 kA/cm^2) than those with larger ITO apertures, before catastrophically short circuiting – somewhat surprising considering that heating is inversely proportional to the device size. For VCSEL-type geometries, the relation between change in temperature and power dissipation is,

$$\Delta T = P_D Z_T = P_D \frac{1}{2\xi s}, \qquad (1)$$

where s is the diameter of the device is and ξ is the thermal conductivity (ξ_{GaN} = 1.3 W/cm-K). A possible explanation is that shorting occurs along threading dislocations; smaller devices have fewer of these conduction paths.

As an aside, the light output scale is listed in arbitrary units primarily due to uncertainty in the collection efficiency of the fiber probe. The measurement is in reality a voltage taken from the peak of the PMT signal on the oscilloscope. Assuming no loss in the fiber – at the device, along the fiber, and at the PMT – 1 volt on the readout translates to approximately 2 nW of output power, after accounting for the responsivity of the PMT and a gain of 1.1 x 10^6.

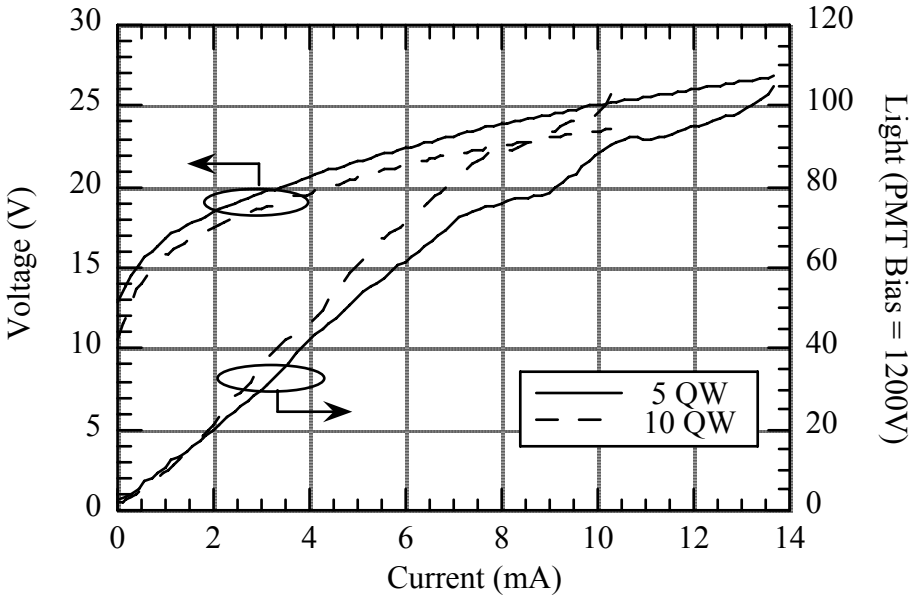


Fig. 17. Comparison of 110 nsec, 5 kHz pulsed L-I-V curves for 5 and 10 QW 2 μm aperture devices with ITO contacts.

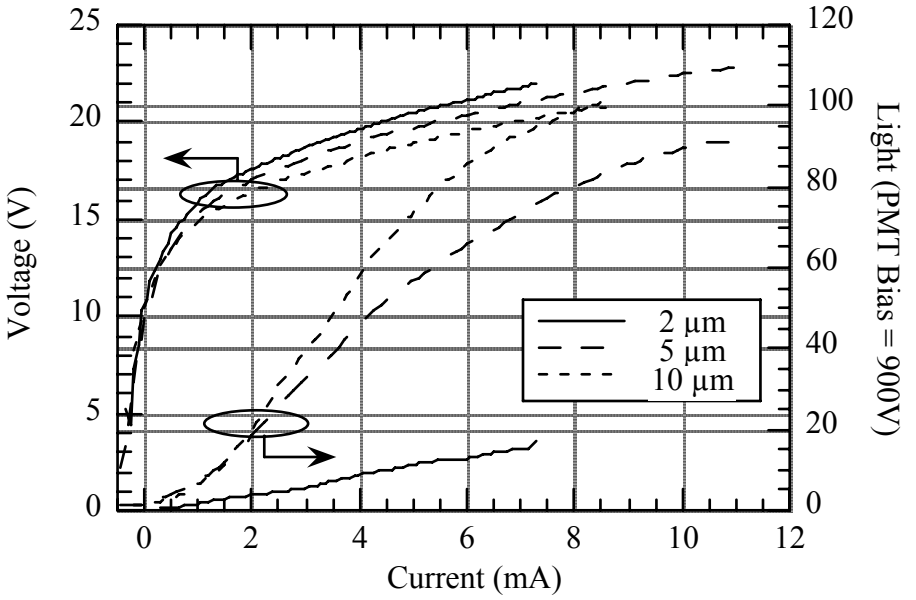


Fig. 18. Comparison of 110 nsec, 5 kHz pulsed L-I-V curves for 10 QW devices with ITO contacts and varying aperture diameters.

Devices with a 5 μm diameter implant-defined aperture were also tested, and the L-I-V characteristics are shown in Fig. 19. Due to non-optimized regrowth conditions the turn-on voltage of these devices is still around 15 V, even though the devices incorporate 2 ohmic metal contacts. The bend in the L-I curves of these diodes at low currents is more significantly pronounced than for the ITO-devices, indicating a greater presence of non-radiative traps.

Emission from the devices was centered between 400 and 410 nm. A pulsed spectrum for a 10 μm aperture device is shown in Fig. 20, taken with a CVI SM240 integrating diode array spectrometer. Cavity modes are clearly present and spaced 4 to 5 nm apart, as expected for a cavity length of approximately 5.5 μm. The spectral linewidth of the modes is around 0.8 nm full width at half maximum (FWHM), from which we calculate a cavity Q of >510. Two other peaks of note are visible in the spectrum.

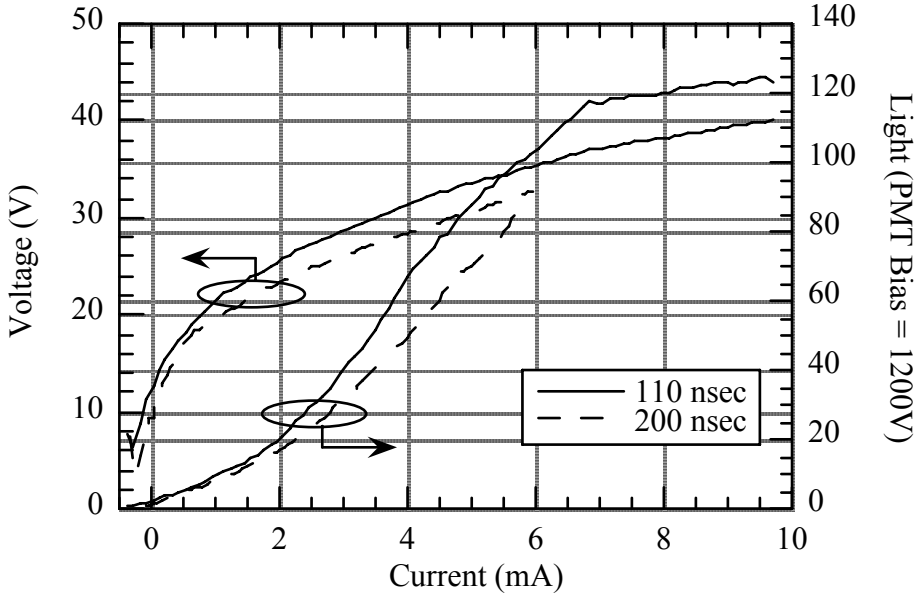


Fig. 19. L-I-V characteristics of a 5 μm implant-defined aperture device, pulsed at 5 kHz and varying pulse widths.

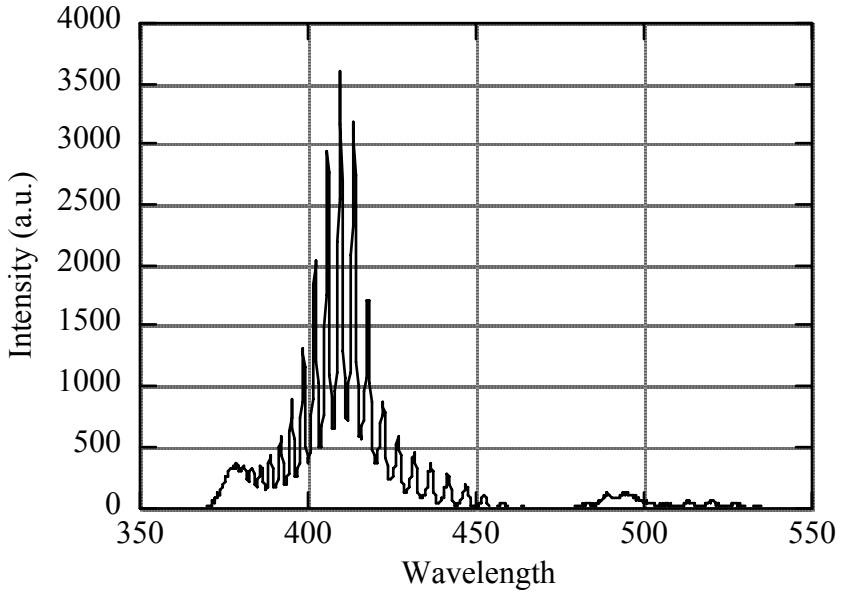


Fig. 20. Pulsed spectrum (200 nsec, 5 kHz) for a 10 μm aperture 10 QW device with an ITO contact.

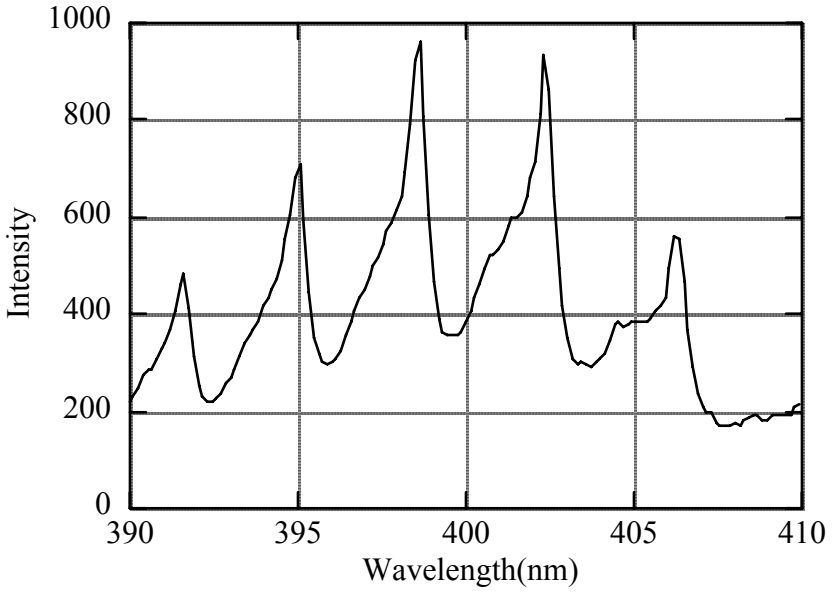


Fig. 21. Zoomed-in pulsed spectrum (50 nsec, 5 kHz) for a 10 μm aperture 10 QW device with an ITO contact.

The first is a low-intensity peak at around 500 nm. We believe this to be a result of constructive interference with an air-gap cavity formed between the AlN submount and the first dielectric DBR. The second peak, at a shorter wavelength emission of approximately 380 nm – corresponding to the InGaN barriers – appears at higher current densities for some devices. This peak increases in intensity with higher current injection while the intensity of the primary peak at 400 nm saturates. Most likely this is carrier leakage due to heating, corresponding to the roll-off in the L-I characteristics at higher currents.

There were slight variations between devices. Figure 21 shows a pulsed spectrum for another diode from the same wafer. The modal linewidth in this case is around 0.6 nm (Q >660). Of interest is the appearance of secondary shoulder peaks at the left (shorter wavelength) of the main modes, also evenly spaced. These may be lateral modes, reflecting off of the dielectric layers defining the device aperture.

R.2 Ultraviolet LED Growth and Fabrication

The room-temperature photoluminescence spectra of UV LEDs with 'bulk' cladding, 2.5 nm $Al_{.06}GaN$ quantum wells, and varying amounts of Al in the 5.0 nm quantum well barriers are shown in Fig. 22 below. Strong emission was detected at ~ 345nm (QW emission) and ~365nm (the GaN band edge) for all structures. The GaN band-edge emission came from the underlying GaN 'template' layer, which is absorbing at the QW emission wavelength, but had much lower dislocation density than an AlGaN template layer of the same thickness. As the amount of Al in the AlGaN barriers between QWs was increased, the intensity of the QW emission decreased, which we believe is due to higher strain-driven piezoelectric fields in the wells. These strong fields tend to spatially separate electrons and holes and therefore reduce recombination efficiency, a well-known effect called the Quantum-confined Stark Effect.

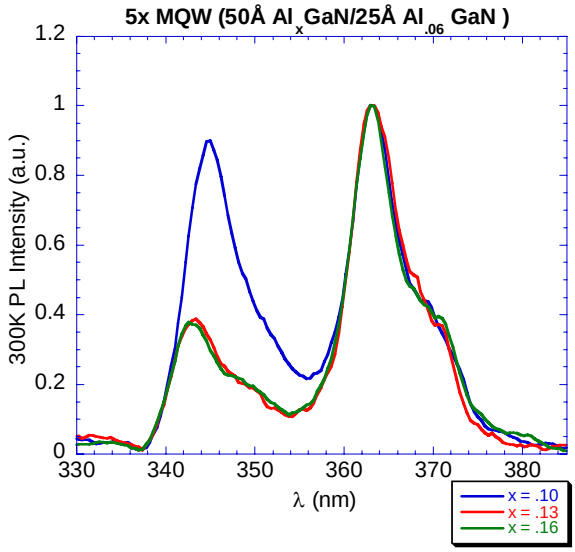


Fig. 22. Photoluminescence of bulk-clad LEDs with varying amounts of Al in the barriers between quantum wells.

As mentioned in the previous section, in addition to 'bulk' AlGaN cladding layers, we also investigated the use of AlGaN superlattices. In preparation for electroluminescence measurements, the electrical properties of processed device structures were first measured, the results of which are shown in Fig. 23. Although all devices had a turn-on voltage of approximately three volts, it became immediately apparent that LEDs with SL cladding layers had lower series resistance, as indicated by their higher I-V curve slopes. This was due to higher hole generation in such SLs, which our group has exploited in the past – a hole concentration enhancement of over 10 times has been observed. The band bending between alternating layers in these SLs causes more Mg acceptor atoms to be ionized, leading to hole accumulation in 'sheets' at the SL interfaces.

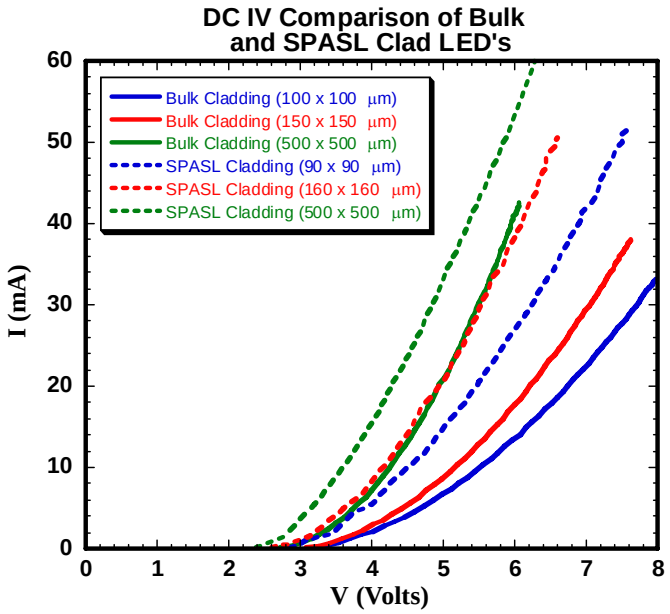


Fig. 23. Comparison of DC IV for bulk- and SPASL-clad MQW UV LEDs.

After initial I-V measurements were completed, electroluminescence (EL) spectra were recorded for SL-clad LEDs at various pump currents. In Fig. 24, EL from 130μm x 130μm LEDs with three QWs as well as five QWs is plotted vs. wavelength. For each drive current, the EL intensity at 348 nm increased as the number of QWs was increased. The higher EL intensity with five QWs shows there was effective pumping of all of the wells despite the low hole mobility typically seen in AlGaN ternary alloys. In the future, we will fabricate LEDs with higher numbers of QWs to see when this trend ceases, which is expected to occur when holes are no longer able to diffuse to those QWs closest to the n-type side of the device.

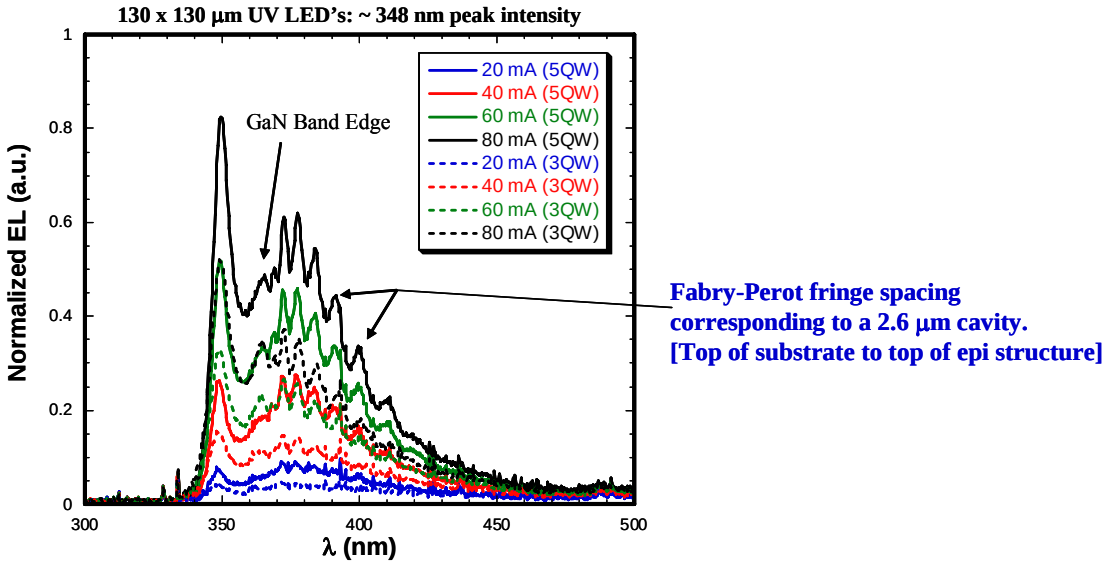


Fig. 24. Electroluminescence (EL) from SPASL-clad 130x130 μm UV LEDs with 3 and 5 QWs, at 20, 40, 60, and 80 mA drive current.

In comparing SL-clad LEDs with three and five QWs, we measured the dependence of both voltage and output power (at 348 nm) on input current, the results of which are shown in Fig. 25. For each number of QWs, we also fabricated devices of two sizes. As expected, the output power of the smaller (130 x 130 μm) devices was higher throughout the input current range, since the current density in these devices was also higher. However, the voltage for smaller devices was in general slightly higher than for larger ones, which suggests problems with lateral p-type conductivity in these structures.

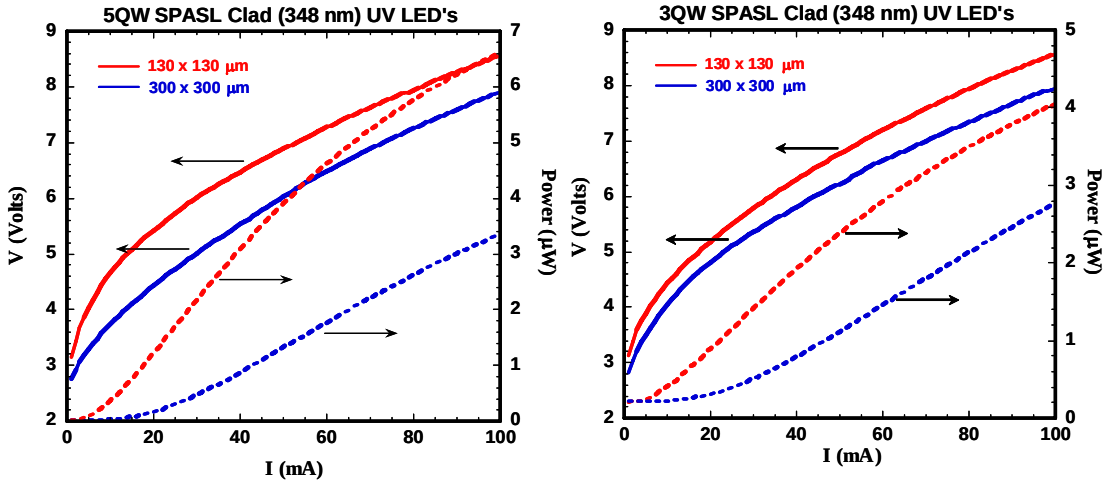


Fig. 25. Voltage (V) and output power (P) vs. current (I) for 5 QW (left) vs. 3 QW (right) SL-clad LEDs.

Finally, we compared the output power vs. current behavior of LEDs of various sizes. As the device size becomes smaller, the current density at a given nominal drive current is higher, which explains the difference between most of the curves in Fig. 26 below. However, at the highest current density (in the 130 x 130 µm device), the effects of device heating are evident, in particular since we grew these structures on sapphire substrates. Sapphire has a low thermal conductivity compared to SiC and Si, and to (Al)GaN itself. In the future when we wish to test at higher current densities (for lasers in particular), heat sinking techniques will be necessary for devices on sapphire.

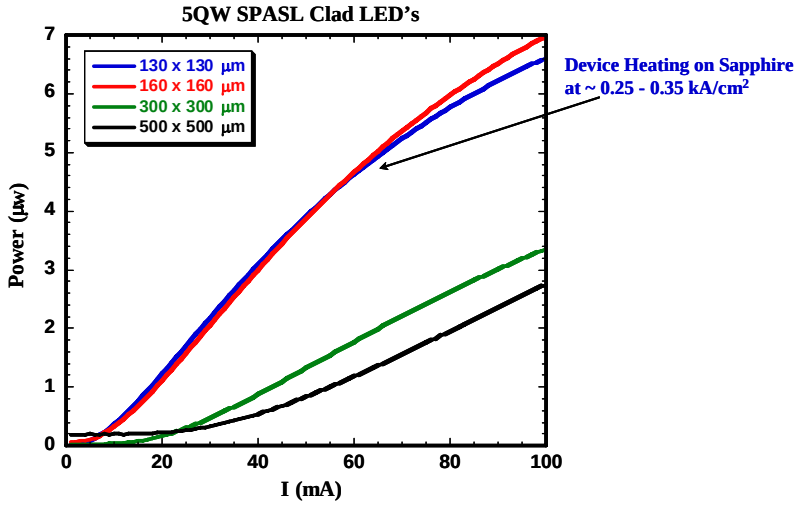


Fig. 26. Output power vs. current (I) for 5QW LEDs of various lateral sizes.

R.3 RCLED and MCLED Development

As mentioned briefly in the last report, RCLEDs have the potential for much higher efficiency than conventional LEDs due to mode formation in a thin cavity. RCLEDs are Fabry-Perot cavities, thus the cavity thickness is an important parameter for device design. In addition,

as shown schematically in Fig. 27 below, the position of the 'source' (in this case one or more quantum wells) must be located in the cavity such that it interferes positively with the light that is reflected back and forth in the cavity. This position may be calculated by taking into account the principal (peak) wavelength of the light being emitted compared to the cavity thickness. Recently, our group has begun performing exact simulations to determine the light extraction efficiency of an RCLED as a function of the cavity thickness and QW position. Preliminary results for a simple RCLED with a silver mirror at the bottom and air on top are shown in Fig. 28. It is apparent that there are indeed multiple combinations of cavity length and quantum well position for which an extraction efficiency of 30% or greater could be reached. In the near future we will investigate the effects of using a DBR reflector instead of the GaN-air (or GaN-epoxy) interface to establish the benefits (or detriments) of using a DBR stack. When dealing with extremely thin cavities, the 'effective length' that a DBR adds on to the cavity length (and thus the cavity order) may outweigh the benefit of inherently higher reflectivity [Weisbuch 2004].

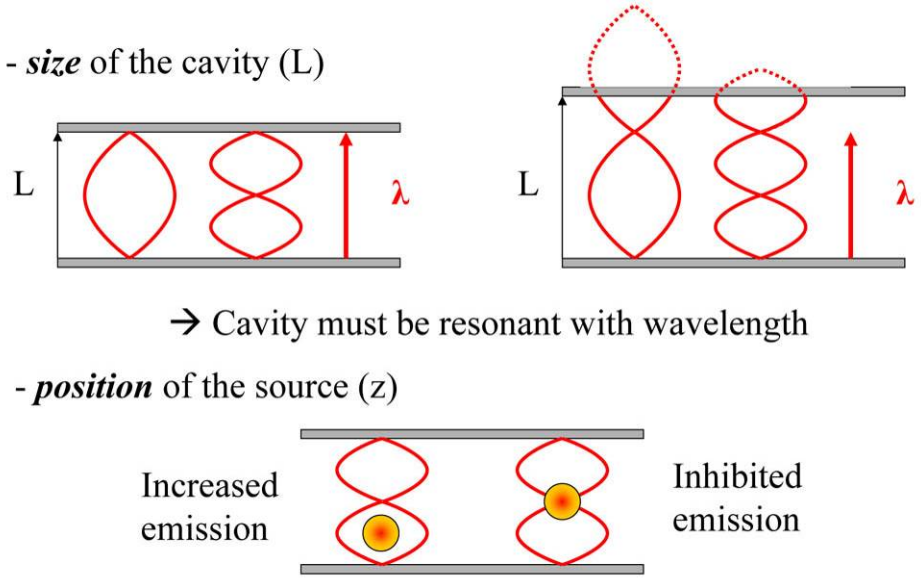


Fig. 27. Size of cavity and source position vs. mode formation.

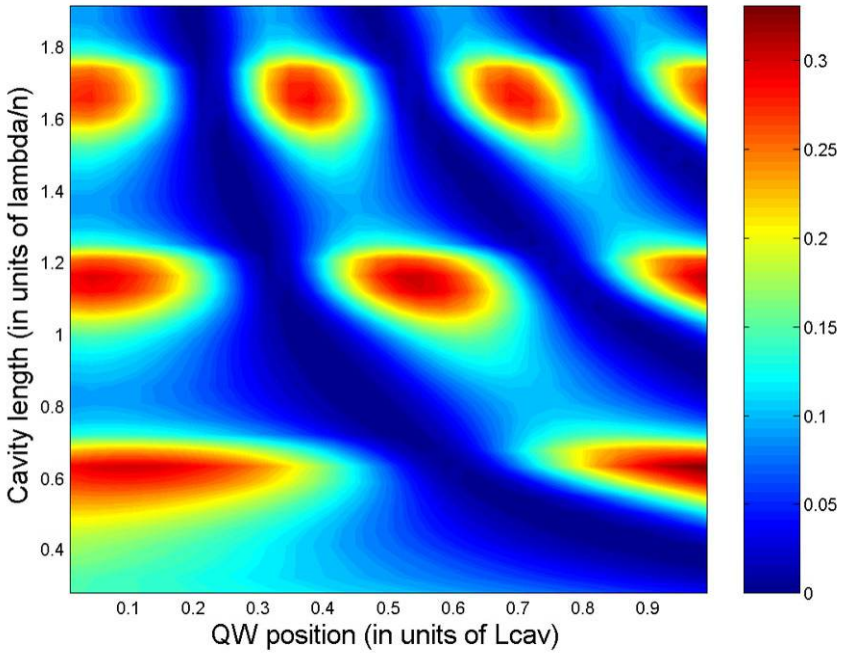


Fig. 28. RCLED extraction efficiency (scale on right) vs. cavity length and QW position.

When a microcavity is formed, the resulting interference determines the directions in which light is emitted, and only modes which are within the extraction cone (denoted by red lines below) will escape. For the sake of extraction efficiency, it is desirable to have as few modes as possible outside this cone, and the way to readily achieve this is to reduce the cavity order (m_c) and thus the thickness of the cavity, as shown below in Fig. 29.

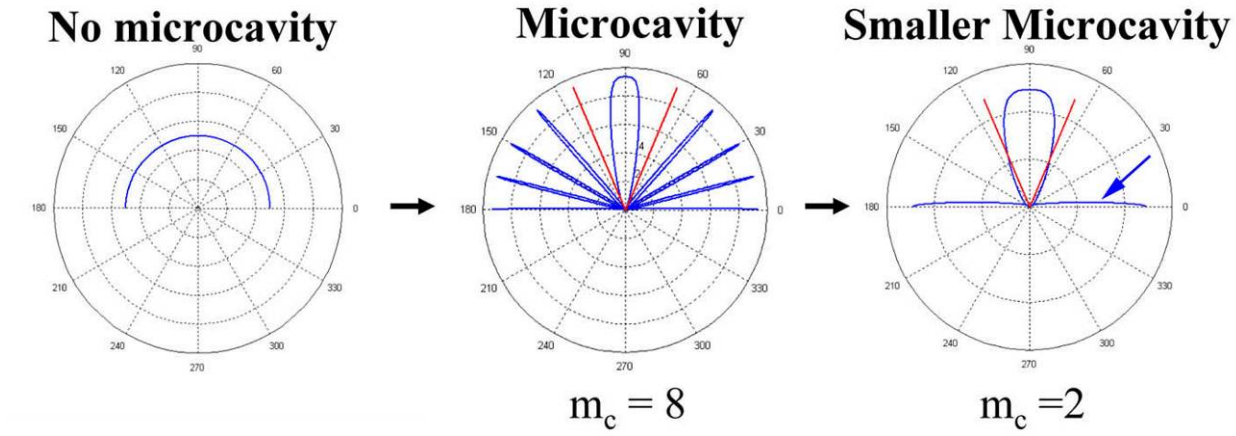


Fig. 29. Angular dependence of emission for a conventional LED (left), a microcavity with a cavity order of 8 (center), and a thinner microcavity with an order of 2 (right). The red lines delineate the extraction cone, which depends on the difference in refractive indices between the LED and its surroundings.

Although a thin cavity is desirable, there are practical difficulties that must be dealt with to achieve even a cavity with an order of 2 or 3. In this case, there are one or more 'guided' modes

which do not directly escape the LED through its top surface, as indicated by the blue arrow on the right in Fig. 29. In fact, it has been calculated that guided modes may limit the single-step extraction efficiency to about 40%, thus they must be extracted [Weisbuch 2004]. An effective way to extract these modes is through the use of scattering or diffraction (coherent scattering). One example of this would be a concentric ringed grating etched into the film around the active region. However, as shown schematically in Fig. 30 below, since the active region is not a true point source, only light rays that meet the rings normally would be optimally extracted via diffraction.

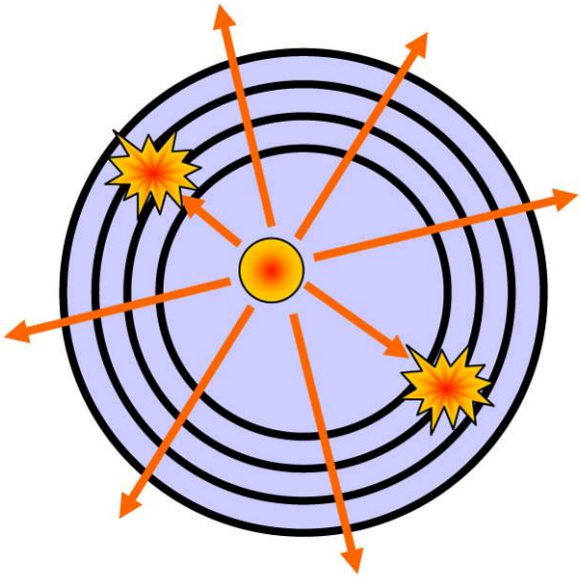


Fig. 30. Schematic of concentric etched ring extraction scheme.

In order to diffract guided modes more isotropically, a 2-D photonic crystal of etched circular holes (for example) would be required. One of the simplest such arrays is a triangular lattice, such as shown in Fig. 31. We fabricated a sample etched-hole lattice using focused-ion beam (FIB) etching, wherein a collimated Ga ion stream was directed at a GaN sample in a 'direct write' process. The FIB technique offers the advantages of high spatial accuracy and smooth etched sidewalls, and although it introduces localized beam damage below each 'pit' that is formed, this damage is located well outside the quantum well active region. Despite these advantages, FIB etching is inherently a slow process, since holes must be etched one at a time. In addition, the field size is relatively small, so that the sample must be frequently translated, and overall pattern periodicity may be lost. Thus we are planning to move to a more 'global' etch process such as inductively coupled plasma (ICP) etching. Since our desired feature size is often on the order of 100 nm or less, this will require the development of fine-scale lithography techniques such as e-beam or holographic lithography.

Analysis of such a triangular lattice reveals that for higher-order diffraction patterns, diffraction is not truly uniform with respect to the in-plane direction of light propagation, as exhibited in the Ewald diagrams of Fig. 32. Figure 32(b) indicates that for a second-order diffraction pattern, diffraction into the light cone occurs for $\theta = 0°$ and 60°, but not 30° (or angles in its vicinity).

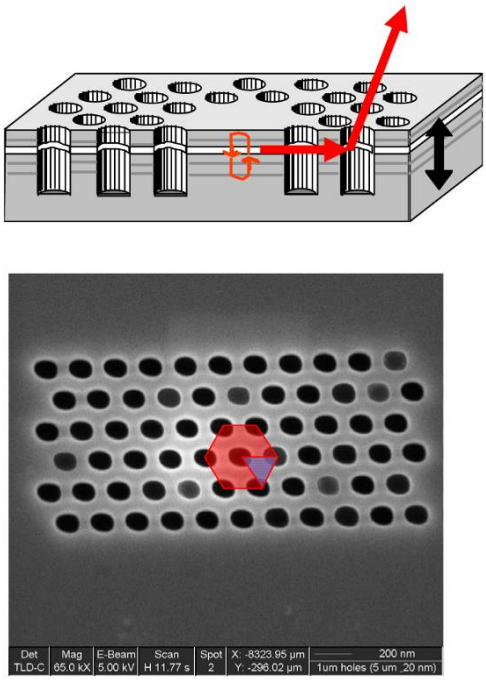


Fig. 31. Schematic of a triangular photonic crystal surrounding an active region (above), and an SEM micrograph of holes etched into GaN with a focused ion beam (below).

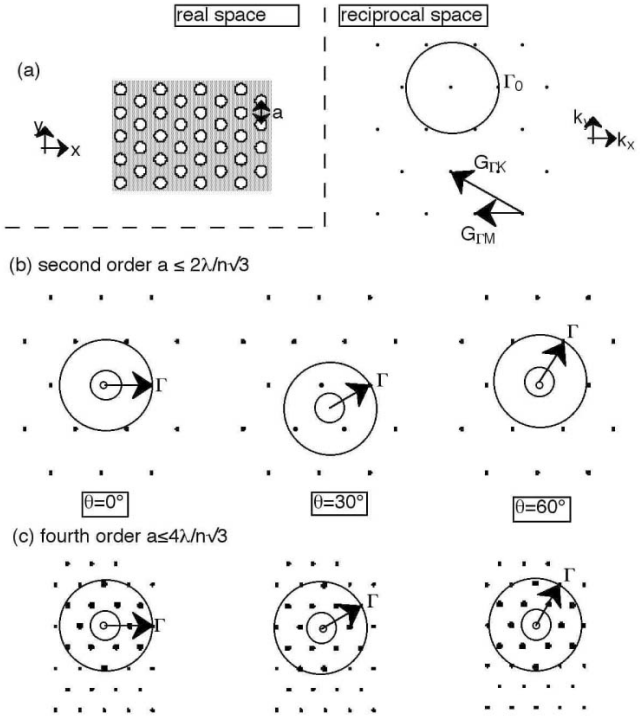


Fig. 32. Ewald diagrams of light diffraction in triangular 2-D photonic crystals as a function of direction (θ = 0, 30, or 90°).

Instead of a simple 2-D triangular lattice, direction-independent diffraction of guided modes may be best achieved with a non-trival lattice whose Fourier transform (*i.e.* form in reciprocal space) has a 'ring'-like character, and thus quasi-isotropic diffraction. Such features are theoretically offered by Archimedean tilings, which essentially consist of supercells of circular openings arranged in a periodic manner [David 2000, Rattier 2003], as shown in Fig. 33. A ring-like reciprocal space map favors single-pass extraction and close to ultimate 'compactness' (a few microns penetration into the lattice), which is important for high-brightness devices. As done for a simple triangular lattice, we have fabricated an etched Archimedean tiling using FIB, whose micrograph is shown in Fig. 34. In the next few months we will attempt to fabricate an RCLED with a periphery of such periodically etched features, in an attempt to increase extraction efficiency. As mentioned above, since FIB may be useful for individual 'before-and-after' comparisons for single devices but is too slow for etching of multiple devices, we will likely optimize dry etching techniques for photonic crystal formation.

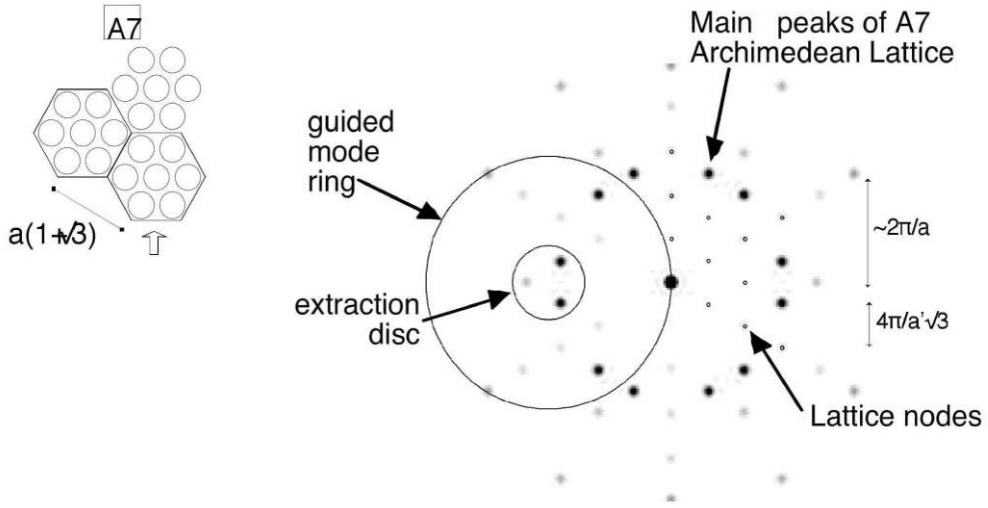


Fig. 33. Schematic of an A7 Archimedean tiling (left), and its associated diffraction pattern (right).

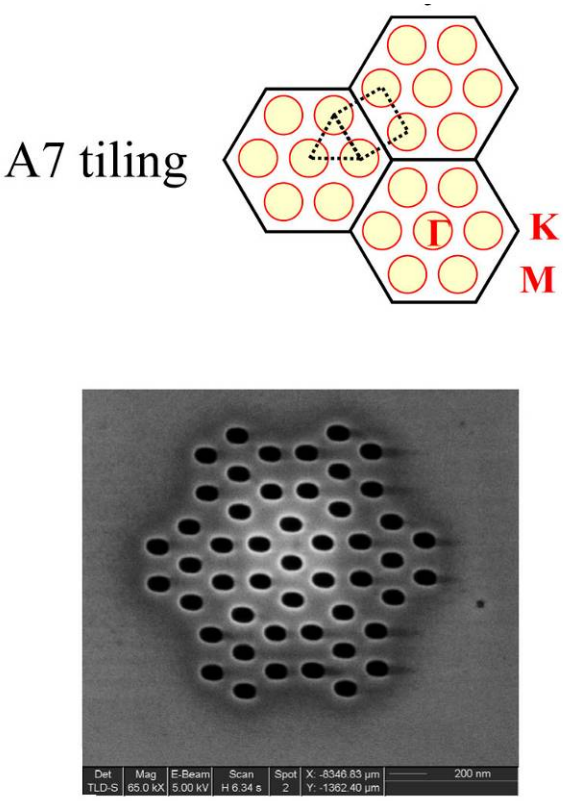


Fig. 34. Schematic of an A7 Archimedean tiling (above), and an SEM micrograph of this tiling etched into GaN with a focused ion beam (below).

Recently we have achieved what we believe to be the first true GaN-based MCLED, *i.e.* a device that operates in the micro-cavity regime due to its extremely low thickness. In Fig. 35, we show the electroluminescence (EL) spectrum for the GaN-based MCLED, overlaid with the EL spectrum for a standard LED processed from the same epitaxial film. The devices were tested on the wafer (*i.e.* unpackaged), and light from each device was coupled at normal incidence into a multi-mode silica optical fiber feeding into a spectrometer. The standard LED had a peak emission wavelength of 480 nm and a spectral full width at half maximum (FWHM) of 47 nm, while the MCLED had a peak emission wavelength of 498 nm and a FWHM of 23 nm. The cavity quality factor (Q) for a planar cavity device is given by:

$$Q = \frac{\lambda}{\Delta\lambda} = 2\pi \frac{L_c}{\lambda}\left(-\ln\sqrt{R_1 R_2}\right)^{-1}$$

where $\Delta\lambda$ is the FWHM of the emitted light. This yields a calculated spectral full width at half maximum of 20 nm, which is in good agreement with our experimental data. The positions of the primary peak at a wavelength of 498 nm and the secondary peak at 450 nm in the collected spectrum were used to arrive at a calculated cavity length of approximately 830 nm, which was again in good agreement with the experimentally determined cavity length.

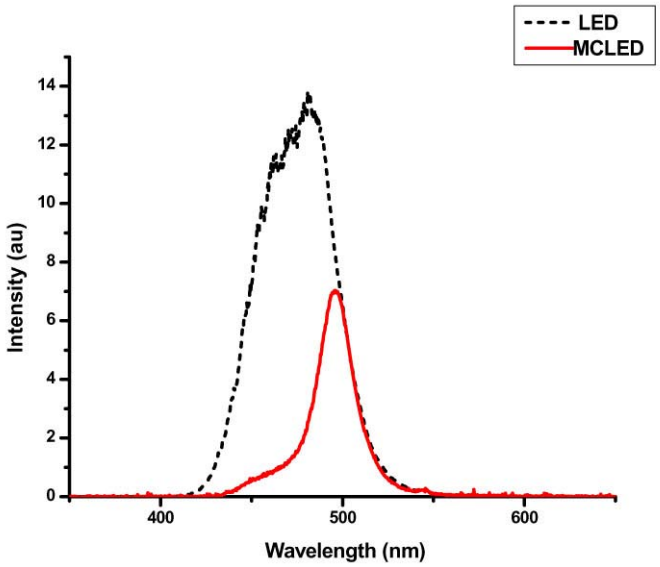


Fig. 35. Emission Spectra of a standard LED (black) and an MCLED (red) processed from the same epitaxial film.

Figure 36 shows a contour plot of the far-field emission pattern for the MCLED. These data were taken by gathering angle-dependent spectra from the bare MCLED device. From Fig. 36, we see that only a single mode was emitted into the extraction cone of the device. The two lobes, observed at +/-16° with respect to normal incidence, produced a symmetric emission profile known as 'rabbit ears', and are indicative that the device was indeed operating within the micro-cavity regime. Additionally, they indicate that the resonant emission wavelength was slightly detuned from the resonant wavelength of the cavity, which improved the extraction efficiency by increasing the amount of light within the extraction cone [Blondelle 1995, De Neve 1997, Dill 1998]. The angular position of the lobes in the emission pattern in our device indicated only a small difference (10 nm) between the peak emission wavelength and the cavity resonant wavelength.

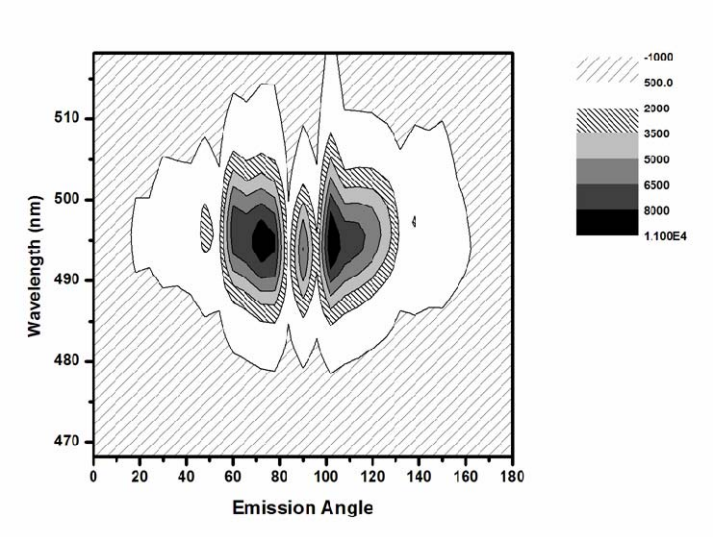


Fig. 36. Contour plot of the MCLED far-field emission, expressed as wavelength at various emission angles.

In summary, we have fabricated a true GaN-based MCLED that emits at a wavelength of 498 nm, using a laser lift-off and etch-back fabrication process. The cavity length of the fabricated micro-cavity device was approximately 830 nm, which resulted in a cavity that was slightly detuned from the peak emission wavelength. This detuning was manifested in the far-field emission pattern as a pair of peaks at +/-16°, thereby providing information about the cavity length of our device and attesting to the fact that the device was operating within the micro-cavity regime. The extraction efficiency of the device was determined through modeling of the far-field emission pattern and the device structure, and a value of approximately 10% was calculated, thus establishing that we observed a definite enhancement in the extraction when compared to a standard LED. The simple design and fabrication process we used is promising for future GaN-based micro-cavity devices.

R.4 A-plane GaN Lateral Overgrowth by HVPE

Figure 37(a) shows a Nomarski optical contrast micrograph of a 20 µm-thick coalesced LEO film formed by $[10\bar{1}0]$-oriented stripes. The faint "fish scale"-like feature on the right side of the image demonstrates that the film's surface is in focus, while the refractive index contrast from the SiO_2 allows the out-of-focus mask pattern to be observed. Similar, near-featureless surfaces are observed for masks consisting of arrays of circular apertures. Atomic force microscopy (AFM) was performed to compare the surface quality in the window and wing regions of the *a*-plane LEO films. Figure 37(b) shows a 40 x 40 µm AFM micrograph spanning multiple stripes. The window region appears as the band of heavily pitted material, with the coalescence front a few micrometers to the left of the windows. This pitted region is shown in detail in Fig. 37(c). The broad, light band between the pitted regions is the Ga-face wing, enlarged in Fig. 37(d). The overgrown material exhibits virtually no pitting and surface roughness on the order of 0.7 nm.

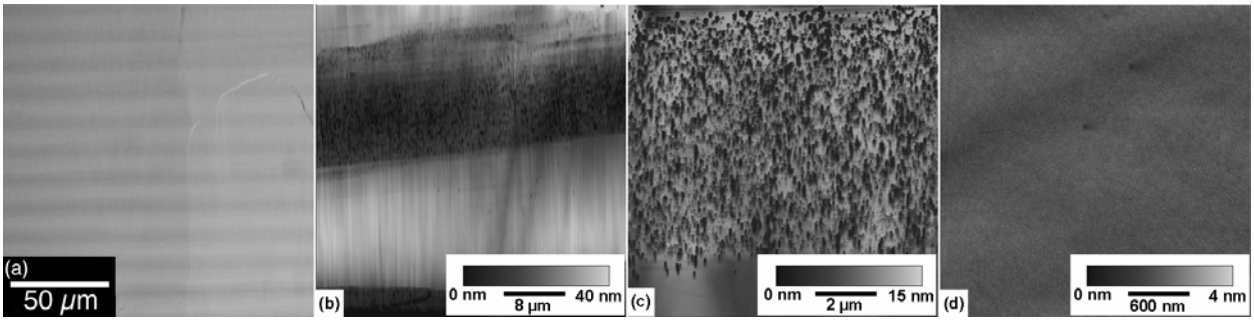


Fig. 37. **(a)** Nomarski optical contrast micrograph of a coalesced LEO *a*-plane GaN film. The stripes are oriented along the $[10\bar{1}0]$ direction. **(b-d)** AFM images of coalesced $[10\bar{1}0]$-oriented GaN stripes: (b) 40 x 40 µm image showing the relative surface quality of the window and wing regions. **(c)** Magnified view of the window region. **(d)** Magnified view of the overgrown region.

Figures 38(a) and (b) are cross-sectional SEM images of LEO wafers patterned with a periodic array of $[10\bar{1}0]_{GaN}$- oriented SiO_2 stripes. Figure 38(a) demonstrates the sharply vertical {0001} sidewalls that are prevalent for $[10\bar{1}0]$-oriented stripes, and Fig. 32(b) shows an inclined cross-sectional view of three coalesced GaN stripes. The two arrows point to sub-micron voids that are frequently observed at the wing-mask interface at the coalescence front. These voids are observed to result when $\{11\bar{2}2\}$ facets form on the lower edges of the Ga-face (0001) planes

within the last 1 μm of lateral growth, possibly due to a mass transport-limited local shift in the V/III ratio. Figure 38(c) is a plan-view SEM image of a coalesced film, again with a mask of SiO_2 stripes oriented along the GaN $[10\bar{1}0]$ direction. The surface is flat and almost featureless, except for a few faint irregular ridges. These ridges manifest themselves in the corresponding cathodoluminescence (CL) image in Fig. 38(d) as dark lines due to scattering. Figure 38(d) is a monochromatic CL image of the surface in Fig. 38(c) imaged at 365 nm, with lighter shades of grey indicating greater luminous intensity. The window regions in the CL image are apparent as the dark horizontal bands. Higher-magnification CL images allow the fast-growing Ga-face [0001]-advancing wing to be distinguished from the slow-growing N-face $[000\bar{1}]$-advancing wing, as the Ga-face wing tends to grow approximately 8-12 times as fast as the N-face wing. As a result, the coalescence front resides within 1-2 μm of the windows and provides little defect-free surface area. The narrow, dark stripes oriented along the <0001> direction do not appear to correspond to surface features. The cause of this decreased luminescence is a point of ongoing investigation.

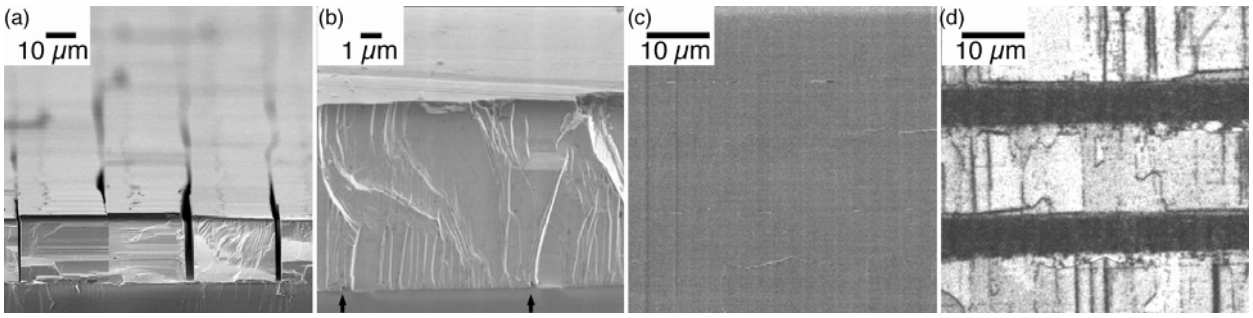


Fig. 38. (a) Cross-sectional SEM image of parallel LEO stripes approaching coalescence. **(b)** Cross-sectional SEM image showing coalesced stripes. The arrows mark sub-micron voids at the wing-mask interface where the stripes coalesced. **(c)** Plan-view SEM image of the coalesced region pictured in **(d)**, which is a monochromatic CL image of the region shown in **(c)** at 365 nm. The mask in each case consisted of parallel SiO_2 stripes along the GaN $[10\bar{1}0]$ direction.

The structural quality of the *a*-plane LEO films was characterized by x-ray diffraction (XRD) and TEM. X-ray rocking curves of the $11\bar{2}0$ GaN reflection taken perpendicular to the LEO stripe direction were single-peaked, indicating a lack of measurable tilt in the coalesced films. Furthermore, narrowing of both on- and off-axis reflections was observed in the LEO films compared to planar *a*-plane GaN films grown directly on *r*-plane sapphire. Typical full widths at half maximum for the $11\bar{2}0$ and $10\bar{1}0$ reflections were 0.21° and 0.35°, respectively. Figure 39 shows cross-sectional and plan-view TEM images of a coalesced a-plane LEO film. In good agreement with observations from AFM and CL, the window regions have high threading dislocation ($\sim 9 \times 10^9$ cm^{-2}) and stacking fault ($\sim 4 \times 10^5$ cm^{-1}) densities. In contrast, the overgrown regions appear to be largely free of both dislocations and stacking faults, indicating a reduction in extended defect density of at least four orders of magnitude.

The above results have demonstrated that substantial reduction in morphological and structural defects in *a*-plane GaN may be readily achieved by LEO with hydride vapor phase epitaxy. The reduction in threading dislocation density in the overgrown GaN is accompanied by a significant improvement in surface morphology compared to planar *a*-plane GaN. Coupling

LEO with the comparably high growth rates achievable by HVPE bodes well for the fabrication of free-standing, high-quality non-polar GaN substrates.

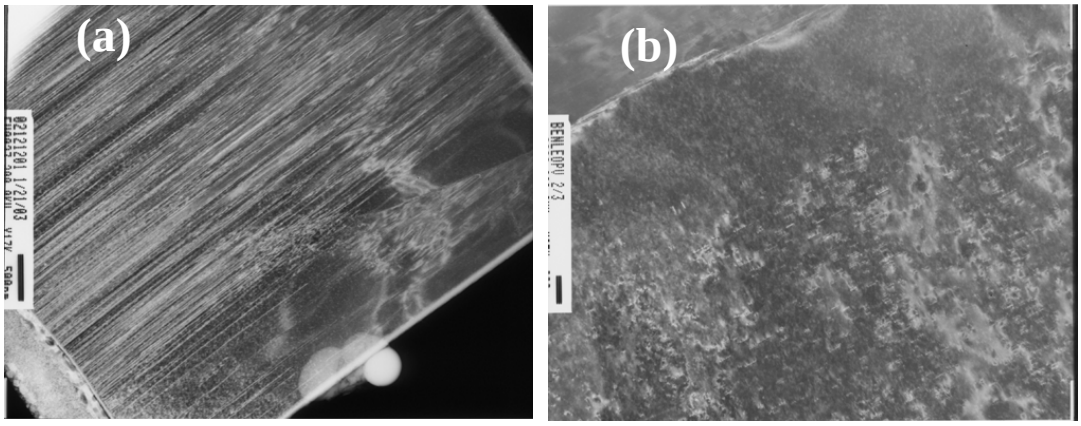


Fig. 39. **(a)** Cross-sectional TEM image of an *a*-GaN LEO stripe. **(b)** Plan-view TEM image.

R.5 A-plane LEDs on HVPE LEO Templates

The current-voltage (I–V) curve of the *a*-plane LED on HVPE LEO GaN exhibited a forward voltage of 3.3 V with a low series resistance of 7.8 V. Nonpolar *a*-plane GaN p–n junction diodes grown under identical conditions on planar *a*-plane GaN templates exhibited similar forward voltage but had higher series resistances, on the order of 30 Ω. The lower series resistance in these LEDs can be attributed to the higher conductivity in the defect-free overgrown region of the LEO GaN template. The electroluminescence (EL) spectra of the devices were studied as a function of the dc drive current. Emission spectra were measured at drive currents ranging from 10 to 250 mA. The devices emitted in the violet spectral range at 413.5 nm for all drive currents, with minimal linewidth broadening (Fig. 40). The absence of blueshift in the emission peak with increasing drive currents is in contrast to the commonly observed phenomenon of blueshift in c-plane LEDs working at this wavelength range and similar drive current range. We attribute the absence of blueshifted emission to the absence of polarization-induced electric field in the nonpolar *a*-plane QWs. The linewidth increased almost linearly with the drive current, starting from a minimum of 23.5 nm at 20 mA to27.5 nm at 250 mA. This minimal linewidth broadening with an increase in drive current suggests that the device heating was low in this current regime.

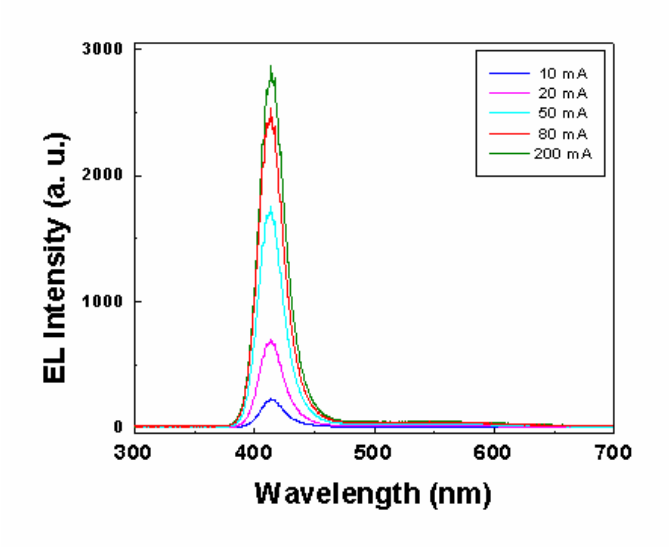


Fig. 40. Electroluminescence spectrum of an *a*-plane LED as a function of drive current. Note the negligible shift of peak wavelength over this current range.

The dependence of the output power on the dc drive current was then measured. The output power increased sub-linearly as the drive current was increased from 10 mA until it began to roll off at a current level close to 250 mA (see Fig. 41). The saturation of the output power can be attributed to heating effects, thereby causing a reduction in the quantum efficiency. The output power at 20 mA forward current was 0.24 mW, corresponding to an external quantum efficiency (EQE) of 0.4%. DC output power as high as 1.5 mW was measured for a drive current of 250 mA. The EQE increased as the drive current was increased, attaining a maximum of 0.42% at 30 mA, and then decreased rapidly as the forward current was increased beyond 30 mA. The comparably low EQE for these LEDs can be attributed partially to the poor reflectivity of the p-contact and partially to the "dark" defective window regions of the LEO, which emit little light. We anticipate significant improvement in EQE by optimization of all aspects of the LED structure.

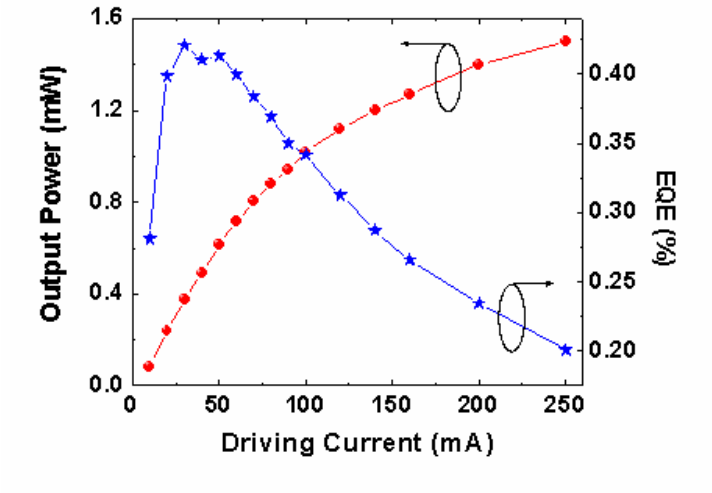


Fig. 41. Output power (left) and external quantum efficiency (right) of an *a*-plane LED as a function of drive current.

R.6 M-plane LEDs on Free-Standing HVPE GaN

Figure 42(a) is a digital photograph of a 250 μm-thick free-standing *m*-plane GaN film. This wafer spontaneously separated from the $LiAlO_2$ substrate, consistent with previous reports [Vanfleet 2003]. Both sides of the wafer were specular and mirror-like, with no evidence of bulk or surface defects. The brownish color of the wafer was attributed to impurity incorporation in the back-side of the HVPE GaN due to the decomposition of the $LiAlO_2$ substrate in the HVPE growth environment. Figure 42(b) is a Nomarski optical contrast micrograph of this film's surface. The surface is characterized by long-range non-crystallographic textures having peak-to-valley heights of less than 200 nm over 500 μm+ lateral extents. Near complete elimination of bulk crystallographic defects, such as pits and "arrowheads," was observed in this and similar films.

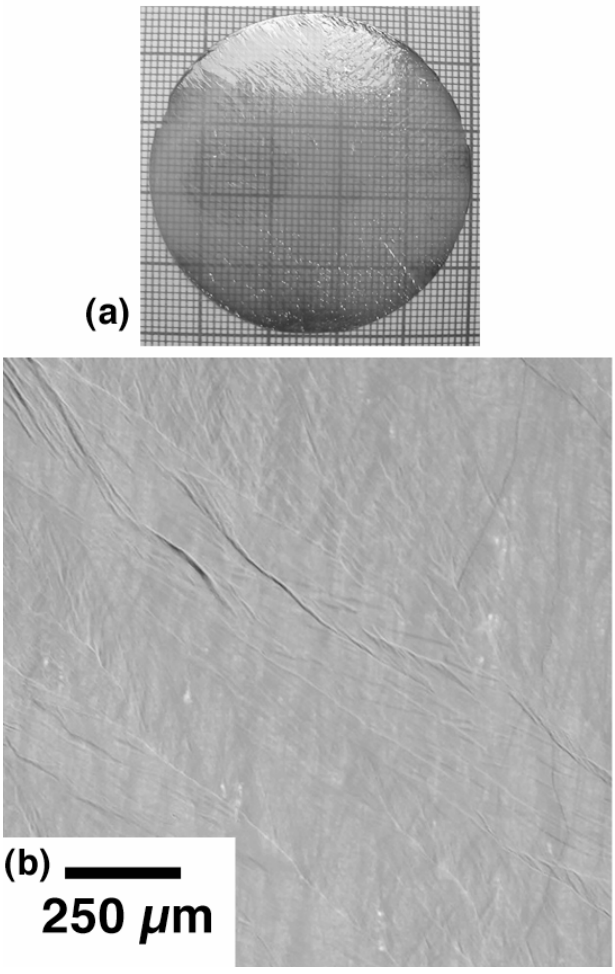


Fig. 42. (a) Digital photograph of a free-standing *m*-plane GaN wafer on a 1 mm^2 grid. (b) Nomarski optical contrast micrograph of the *m*-plane GaN film surface.

Figure 43 shows three 5×5 μm atomic force micrographs of representative *m*-plane GaN film surfaces. Figure 43(a) shows an irregular, non-crystallographic morphology that is infrequently observed in *m*-plane GaN films. The scalloped surface was reminiscent of a defective *c*-plane GaN film having a very high density of threading dislocations and step edges. This sample had a RMS roughness of 0.909 nm over the 25 μm^2 area shown in the image. Figure 43(b) shows the most commonly observed morphology in *m*-plane GaN films. This striated, or "slate" morph-

ology is dominated by ridges oriented along the GaN <11$\bar{2}$0> direction. The linear density of these ridges along the <0001> direction averaged ~10^5 cm^{-1}. This image also revealed regions dominated by pits that are likely related to screw- or mixed-character threading dislocation terminations at the free surface. The 0.894 nm RMS roughness of this surface was comparable to that shown in Fig. 43(a) despite the differences in morphology between the two surfaces. The surface morphology shown in Fig. 43(c) also exhibited fine ridges oriented along the GaN <11$\bar{2}$0> direction, but lacked the pitting that is commonly observed in films possessing the "slate" morphology. This surface was significantly smoother than those shown in Fig. 43(a) and (b), with an RMS roughness of 0.636 nm. All three of the morphologies shown in Fig. 43 have been observed on single wafers regardless of growth conditions, though the "slate" morphology shown in Fig. 43(b) was most prevalent.

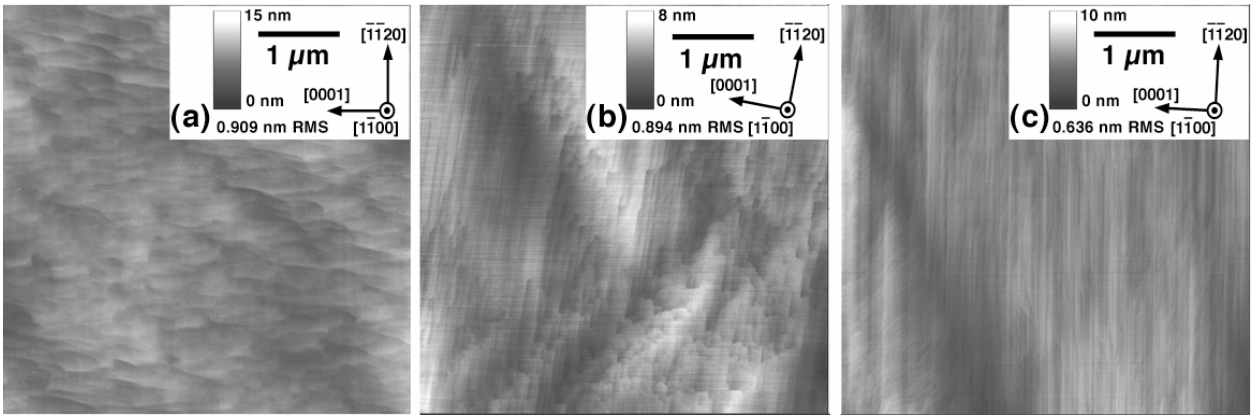


Fig. 43. Atomic force micrographs of representative *m*-plane GaN film surfaces.

Electroluminescence (EL) spectra of the *m*-plane LEDs were measured for dc drive currents ranging from 10 to 200mA (Fig. 44(a)). The devices emitted in the blue spectral range with an emission peak ranging from 460 nm at 5mA to 449.6 nm at 200 mA. There was a small blue-shift (shown in Fig. 44(b)) in the emission peak for drive current between 5mA to 50 mA. This initial blue shift, also observed in some planar a-plane InGaN/GaN LEDs, can be attributed to the band-filling of the localized states induced by alloy fluctuation in InGaN quantum wells [Chichibu 2004]. However, there was minimal blue shift at higher drive currents (in excess of 70 mA, corresponding to a current density of 77.7 A/cm^2), indicating the absence of polarization-induced electric fields in the *m*-plane quantum wells. A linewidth of 38 nm was measured for the spectrum at 20 mA drive current.

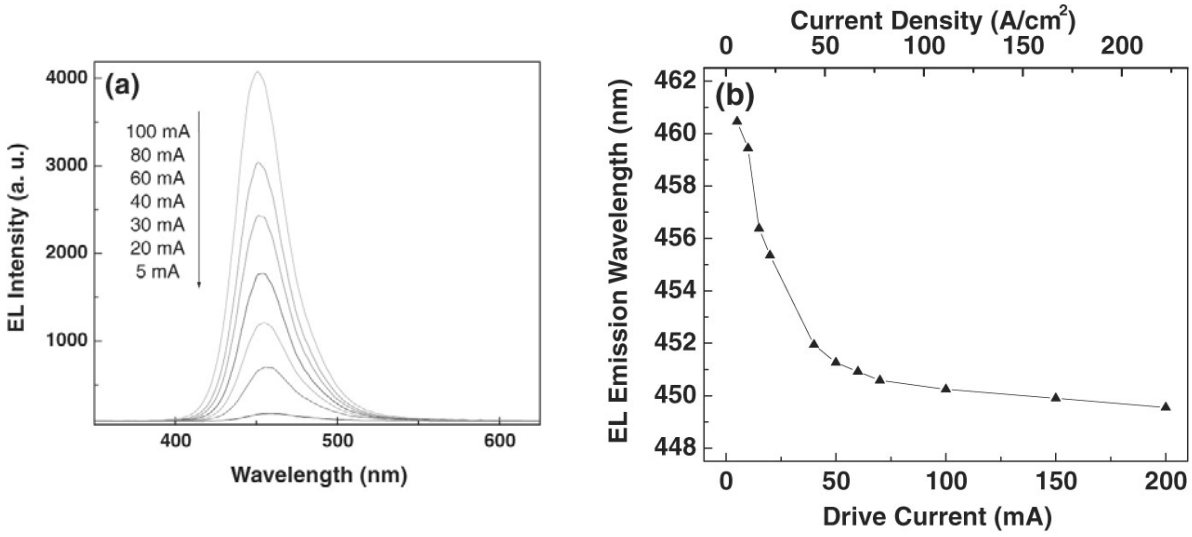


Fig. 44. (a) *m*-plane GaN LED electroluminescence vs. wavelength for various drive currents. (b) Peak wavelength vs. drive current.

The *m*-plane LED on-wafer (unpackaged) output optical power increased almost linearly as the drive current was increased from 10 mA to 250 mA (Fig. 45). There was no indication of 'roll-off' of the output power with increasing drive current, as was observed in LEDs grown on lateral epitaxially overgrown a-plane GaN on r-plane sapphire, described above. This suggests that there is improved heat dissipation in the m-plane device on free-standing GaN because of the higher thermal conductivity of GaN substrate compared to sapphire. The output power at 20mA forward current was 0.24 mW, corresponding to an external quantum efficiency (EQE) of 0.43%. An unsaturated continuous wave (cw) output power as high as 2.95 mW was measured for a drive current of 300 mA, which represents the highest reported on-wafer output power for any nonpolar GaN-based LED. The drop in the EQE for drive currents in excess of 50mA is probably a result of reduced radiative recombination efficiency at high currents due to device heating. Optimization of the quantum well parameters and the growth conditions are in progress to further improve the performance of the nonpolar m-plane light emitters.

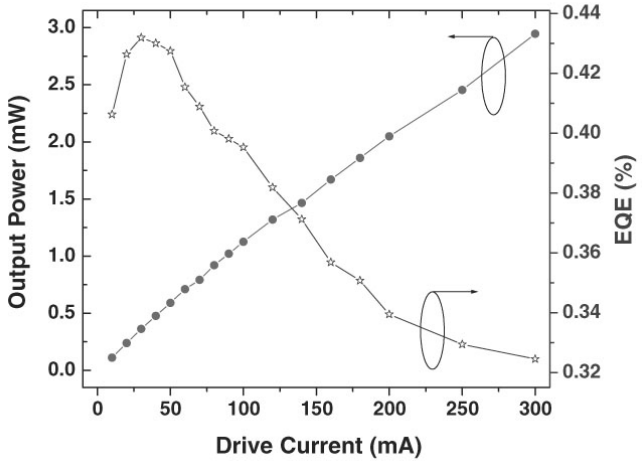


Fig. 45. Unpackaged *m*-plane LED output power and external quantum efficiency vs. drive current.

In summary, we have demonstrated for the first time *m*-plane blue LEDs grown on free-standing m-plane GaN substrates. An EL emission peak of ~450 nm was observed for drive currents in excess of 70 mA. An unsaturated continuous-wave output optical power as high as 2.95 mW was measured for a drive current of 300 mA. The linear dependence of output power with drive current suggested minimal device heating, due to the superior thermal conductivity of the free-standing *m*-plane HVPE GaN substrate.

R.7 Source Modeling

Three packaging issues were considered during the source modeling study.

- How does emission wavelength impact RCLED light extraction efficiency?
- How does the index of refraction of the epoxy material impact RCLED light extraction efficiency?
- What die placement within the epoxy allows for the maximum collection of edge-emitted light from the RCLED?

Impact of wavelength emission on light extraction efficiency

The impact of emission wavelength on light extraction efficiency was analyzed using LightTools ray-tracing software. The modeling assumptions/parameters included:

- 350 μm aperture RCLED
- Emission pattern similar to InGaAs RCLED internal emission pattern
- An epoxy cone (1.515 refractive index, 60° taper angle, 180 μm radius and 1000 μm height)
- Ten-thousand rays traced for each condition

The modeling results show light extraction efficiencies of 51.2% at 412 nm and 51.1% at 460 nm. In this model, the wavelength dependency of the refractive index was not included because the information was not available.

Impact of epoxy refractive index on light extraction efficiency

Next, the impact of the epoxy material's index of refraction on RCLED light extraction efficiency was analyzed in LightTools. The modeling assumptions included:

- 350 μm aperture RCLED
- Emission pattern similar to InGaAs RCLED internal emission pattern
- An epoxy cone (60° taper angle, 180 μm radius and 1000 μm height)
- Ten-thousand rays traced for each condition

The modeling was conducted at various epoxy refractive indices. Table 1 shows the results.

Table 1. Initial modeling results investigating various epoxy refractive indexes and their effect on light extraction efficiency.

Epoxy refractive index	1.40	1.515	1.56	1.75
Light extraction efficiency	48.0%	51.2%	51.6%	51.2%

Overall, the highest efficiency occurs when the refractive index of the epoxy matches with the SiO_2 material refractive index (1.56 - the last layer of the DBR).

Impact of die placement on edge-emitted light collection

Discussions with the UCSB team indicated that RCLEDs have a strong edge-emitting property. In last year's modeling study, the RCLED was placed at the bottom of the epoxy cone. This resulted in edge-emitted rays being uncollected by the epoxy cone (Fig. 46(a)). Figure 46(b) illustrates that when the RCLED was placed inside the epoxy cone (fully immersed into the epoxy), all the rays were collected by the epoxy cone.

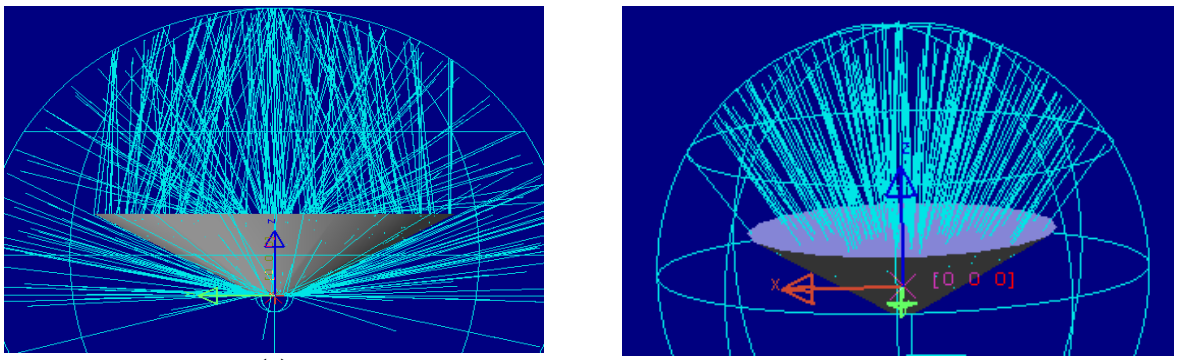


Fig. 46. Placement of the RCLED: (a) RCLED placed at the bottom of the epoxy cone; (b) RCLED placed inside the epoxy cone).

Summary

In general, wavelength (in the range 410 to 460 nm) did not impact light extraction from the RCLED. However, in this analysis wavelength dependency of the index of refraction of the semiconductor layers or the epoxy were not considered. The highest extraction efficiency occurs when the refractive index of the epoxy matches the index of refraction of the last distributed Bragg reflector (DBR) layer. Edge-emitted light from the RCLED can be collected to increase overall efficiency by fully immersing the die in a conical-shaped epoxy optic.

R.8 Phosphor Characterization and Secondary Optics Studies

Phosphor Characterization

The LRC conducted a phosphor characterization study to better understand the interaction between short-wavelength light and phosphor and to quantify the amount of light reflected back to the die in a phosphor-converted white LED package. Several 2-inch diameter circular glass plates were coated by OSRAM SYLVANIA (Dr. Madis Raukas) with YAG:Ce phosphor in different densities, ranging from 2 mg/cm^2 to 8 mg/cm^2. The plates were positioned between two integrating spheres, with the phosphor coating facing the right sphere (Fig. 47). A 5-mm blue LED, placed inside the right sphere and positioned 1-inch away from the glass plate, excited the phosphor material, and a spectrometer measured the light output from each sphere through the measurement ports. Measurements from the left sphere indicated the amount of light transmitted through the phosphor layer of the glass plate; measurements from the right sphere indicated the

amount of light reflected off the phosphor layer and back toward the LED. The light output data were analyzed for the amount of flux in the blue and yellow regions, corresponding to the radiant energy emitted by the LED and the converted energy from the YAG:Ce phosphor.

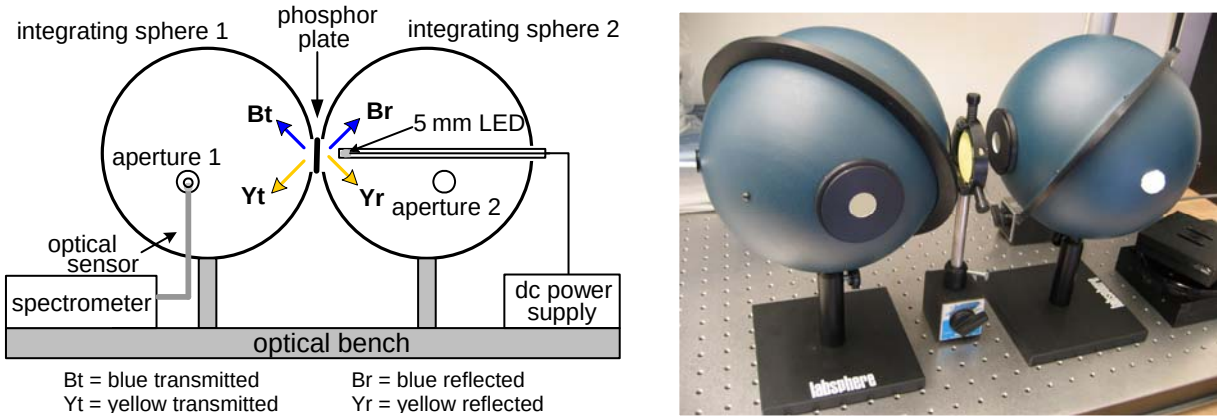


Fig. 47. Experimental setup used for measuring the transmitted and reflected light off the phosphor (Left: schematic of the experimental setup; Right: experimental setup).

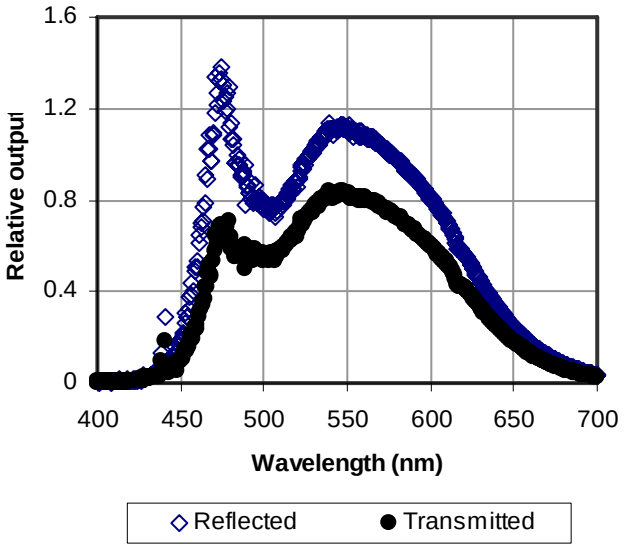


Fig. 48. Spectral power distributions for the transmitted and reflected radiations of one phosphor-coated plate (7mg/cm^2).

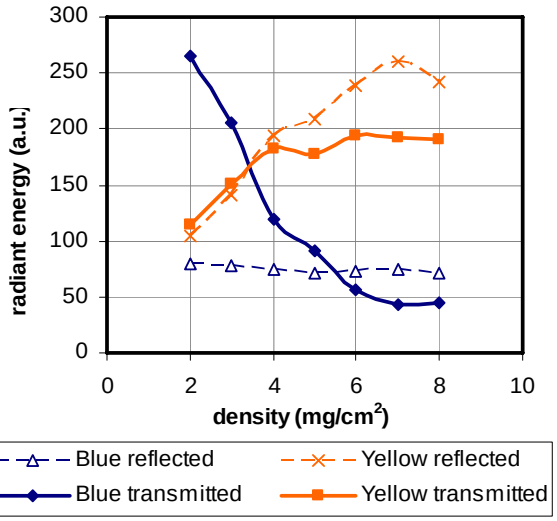


Fig. 49. Reflected and transmitted blue and yellow energy as a function of phosphor density.

Figure 48 presents data for one phosphor plate, 7 mg/cm^2. At this density, the spectral power distributions for the transmitted and reflected light are different, especially the amount of blue-to-yellow ratio. Figure 49 shows the amount of transmitted and reflected radiant energy for both blue and yellow as a function of phosphor density. This figure indicates that the amount of radiation transmitted and reflected changes with the phosphor density, with lower densities allowing a higher percentage of radiation to be transmitted. The phosphor density in a typical white LED package is controlled so that the transmitted blue and yellow light are in the correct

proportion to produce white light of a suitable chromaticity. From the data gathered, we estimated that approximately 40% of the light is transmitted and the remaining 60% is reflected when creating a balanced white light. This estimate is in line with the findings of Yamada *et al.* [Yamada 2003]. In general, the components surrounding the die absorb a high percentage of the reflected light, causing the low luminous efficacy of typical white LED packages.

Scattered distribution measurement

The next issue is to understand whether YAG:Ce phosphor scatters (emit) light in any preferred direction. To enable this study, the LRC built a small goniometer, depicted in Fig. 50. The results from these measurements were useful also to refine the computer simulations of the packaging devices using more realistic phosphor properties.

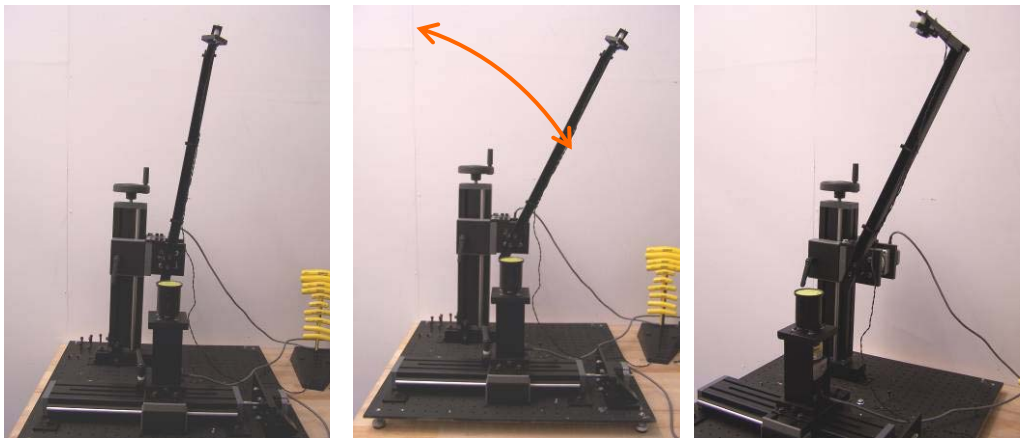


Fig. 50. Two-axis goniometer to measure beam profiles of phosphor-coated plates and LED prototypes.

Based on the results from multiple measurements, it appears that the light emitted from the phosphor layer on the glass plates is very close to a lambertian emitter. Figure 51 shows a polar plot of two distributions. The red line represents the normalized distribution of a phosphor plate, whereas the blue line represents a normalized Lambertian distribution. As it can be seen from this figure, the phosphor distribution closely resembles a Lambertian emitter.

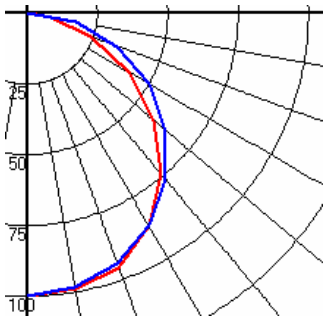


Fig. 51. Normalized intensity distribution of a YAG:Ce phosphor-coated glass plate (red line) and a normalized Lambertian distribution (blue line).

Possible solutions for improving source efficacy

The high percentage of backscattered light from the phosphor layer offers the potential to increase the overall efficiency if some of that light could be recovered to eventually exit the LED package. The next logical step in our research was to design a method to extract as much of the reflected light as possible. Figures 52 to 54 illustrate some of the LED packages that would make it possible to extract more light out of the LED by means of secondary optics and a phosphor layer remote from the LED die. In general, we refer to scattered photon extraction (SPE) as the method of recovering the backscattered light from the phosphor and directing it to exit the LED package.

Unlike typical commercial white LED packages, where the phosphor is spread around the die, the SPE solution requires that the phosphor layer be moved away from the die. In order to demonstrate the SPE concept, SPE Package 3 in Fig. 54 was selected from a variety of SPE packaging options. SPE Package 3 employs a secondary optic with a phosphor coating on the top surface to extract the reflected light.

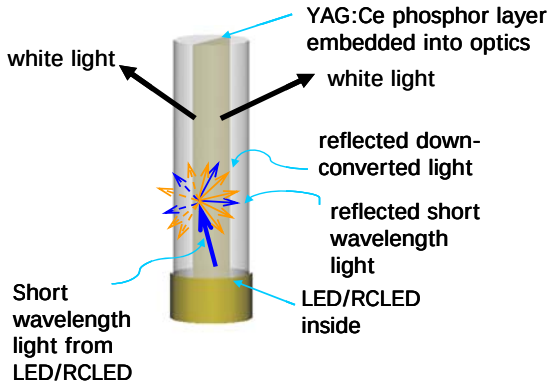


Fig. 52. Schematic of SPE Package 1: the phosphor layer is embedded in the middle section of the distributing optics, as if splitting it into two pieces.

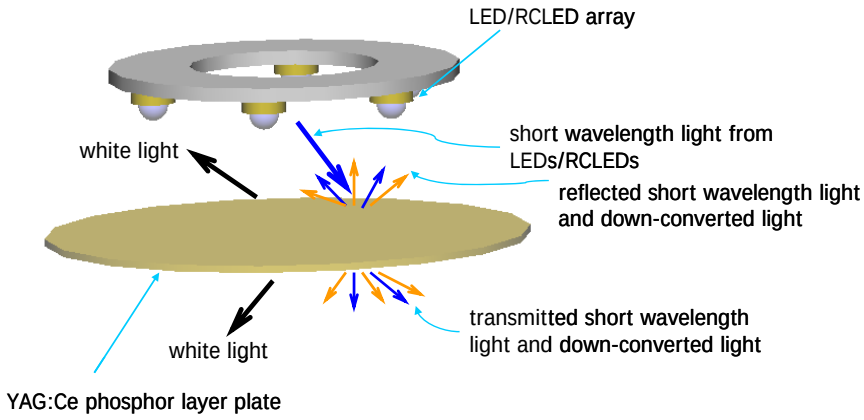


Fig. 53. Schematic of SPE Package 2: a phosphor plate is hanging below the LED/RCLED array.

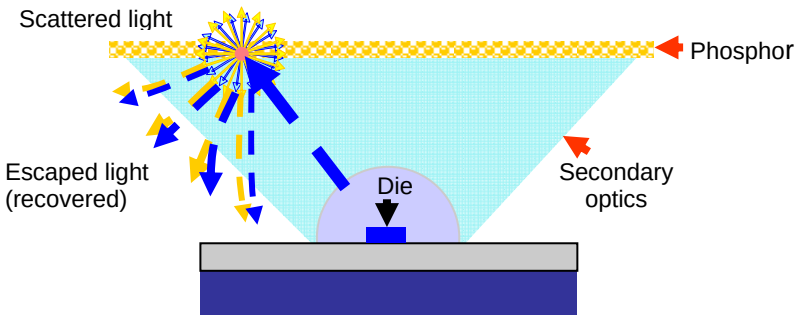


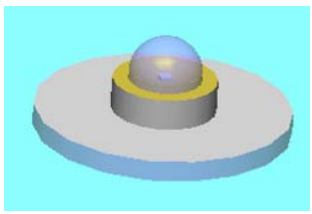
Fig. 54. Schematic of the SPE Package 3: a phosphor layer is coated on top of a secondary optic.

Secondary optic simulation

The geometry of the secondary optic was designed specifically to transfer the light exiting the LED die to the phosphor layer and allow most of the backscattered light from the phosphor layer to escape the optic. To find the optimum profile for the secondary optic, SPE Package 3 was modeled using LightTools.

Source modeling

Because the RCLEDs were still under development by UCSB when the LRC began designing the SPE package, an alternate light source was used to develop the white light source package. The LED source chosen for the package was the Luxeon III Star by Lumileds Lighting. Its simulated luminous intensity distribution matched closely with both the distribution specification from the manufacturer and the LRC goniometric measurements (Fig. 55).



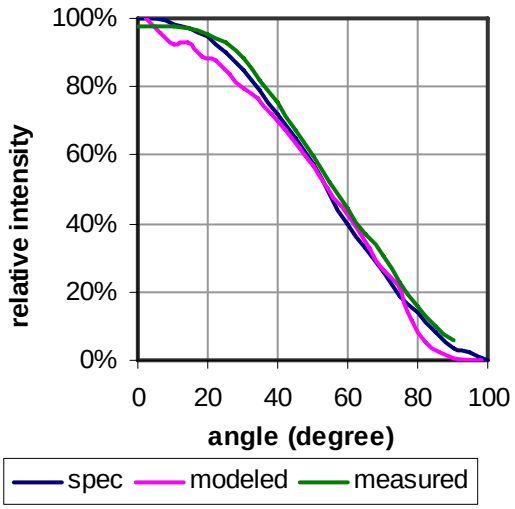


Fig. 55. Luxeon III Star LED LightTools model and its luminous intensity distribution.

Optical modeling: Setup

Five potential secondary optic profiles for SPE Package 3 were designed and evaluated through ray-tracing. Figure 56 shows the setup of the optical model, which consisted of the LED light source, the secondary optic, a far-field receiver, and a circular receiving plane close to the top surface of the optic. The far-field receiver was useful in calculating the overall efficiency of the optic and its intensity distribution. The circular receiving plane counted the percentage of rays exiting from the top surface of the secondary optic, where the phosphor would be placed. To decrease Fresnel losses, the epoxy dome of the LED was embedded into the bottom of the secondary optic. Acrylic was chosen as the optic's material. Because LightTools is limited in its ability to simulate phosphor properties, TIR (total internal reflection) was selected as the optical property for all surfaces of the secondary optic. Fresnel losses were considered in the simulation as well.

The number of rays exiting from the top surface of the model is proportional to the number of rays that have a chance of hitting the phosphor plane, increasing the efficiency of the SPE package. The optical model was run to trace one million rays, which is sufficient to attain results accurate within 5%.

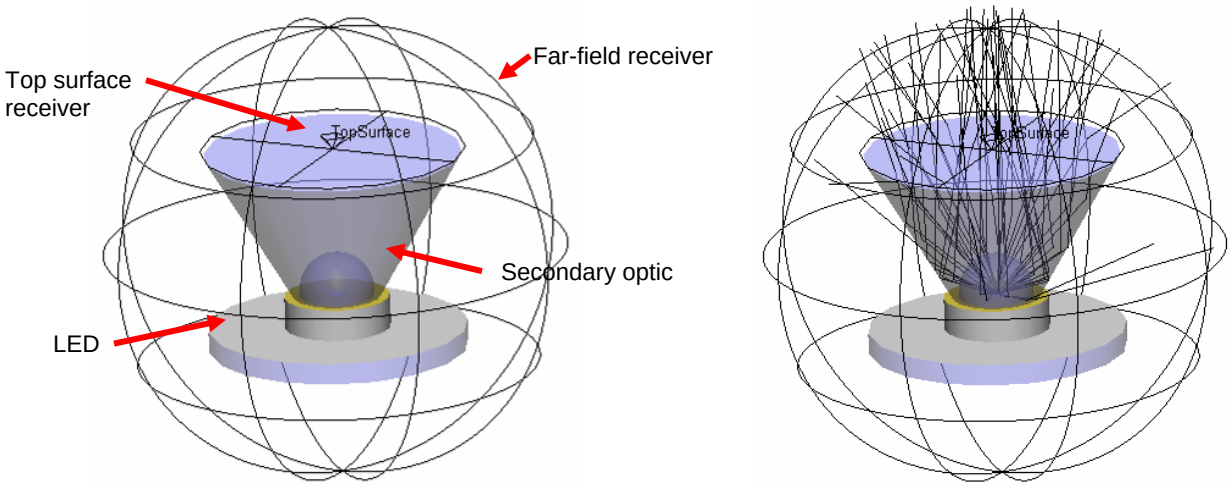
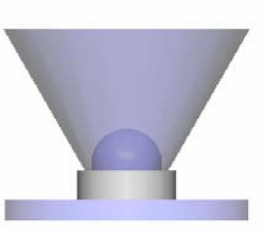
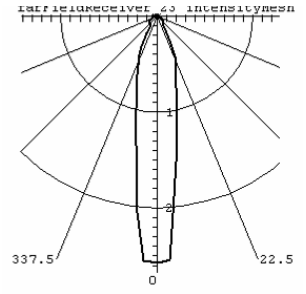


Fig. 56. Optical modeling setup (left) and ray-tracing for the setup (right).

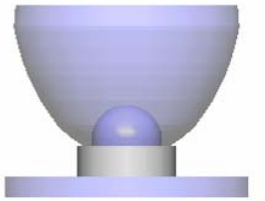
Optical modeling: Results

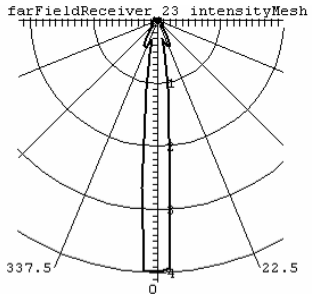
Figure 57 illustrates the five designs (A to E) for the secondary optic and their corresponding intensity distributions. Table 2 compares the efficiency of each design and the percentage of rays exiting from the top surface. Optic A was chosen as the best profile because of its highest number of exiting rays, its acceptable optic efficiency, and its ease of manufacturing. Therefore, Optic A was expected to have the highest number of blue rays hitting the phosphor surface, and hence the highest number of white rays exiting the optic, if the phosphor layer were applied to its top surface.



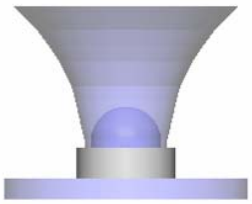

337.5
22.5
0

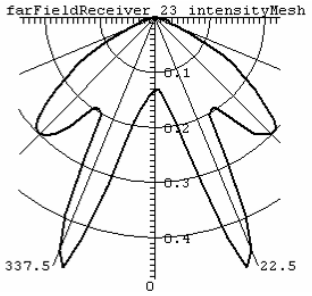
(A)



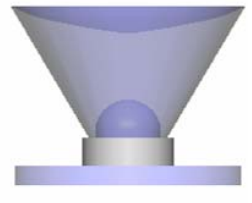

farFieldReceiver_23_intensityMesh
337.5
22.5
0

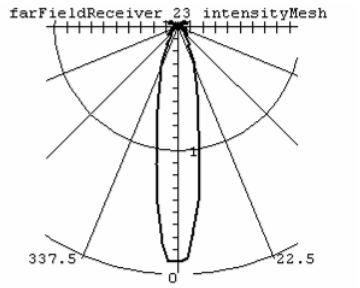
(B)



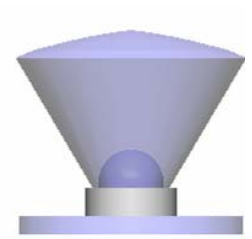

farFieldReceiver_23_intensityMesh
0.1
0.2
0.3
0.4
337.5
22.5
0

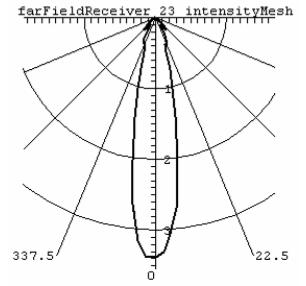
(C)




farFieldReceiver_23_intensityMesh
337.5
22.5
0

(D)




farFieldReceiver_23_intensityMesh
337.5
22.5
0

(E)

Fig. 57. Possible designs for the secondary optic and their corresponding intensity distributions.

Table 2. Optic efficiency and exiting rays for each optic.

	optic efficiency (%)	rays exiting from top surface (%)
A	93	87
B	94	84
C	92	73
D	91	66
E	95	85

Proof of concept

Two packages were prototyped to verify the hypothesis that overall light output and luminous efficacy of a phosphor-converted white LED can be significantly increased by extracting the backscattered photons through the SPE concept. For demonstration purposes, SPE Package 3 and secondary optic A were chosen. Package A (blue LED plus Optic A) combines a commercial blue LED with phosphor around the epoxy dome and an uncoated optic, as shown in Fig. 58. Package B, or the SPE package, combines the same blue LED and the same profile optic with a phosphor layer on the top surface (Fig. 59). The phosphor density applied to both packages (*i.e.*, A and B) is the same. If Package B has a higher light output than Package A, then the SPE hypothesis will be supported.

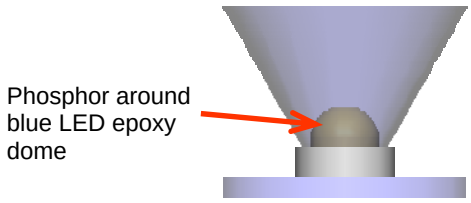


Fig. 58. Package A: Commercial blue LED with phosphor around the epoxy dome and a clear optic.

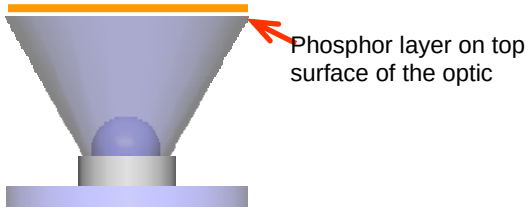


Fig. 59. Package B: SPE package with a commercial blue LED and phosphor coated on the optic.

A commercial optic, illustrated in Fig. 60, that fit the profile requirements of simulated Optic A was found, and several were acquired for experimentation. Inside this commercial optic, a hollow space was available to fit the LED dome. However, this caused an air gap between the LED and the optic, decreasing the optic efficiency to 91% according to simulation. Nevertheless, the commercial optic design was sufficient to verify the hypothesis.

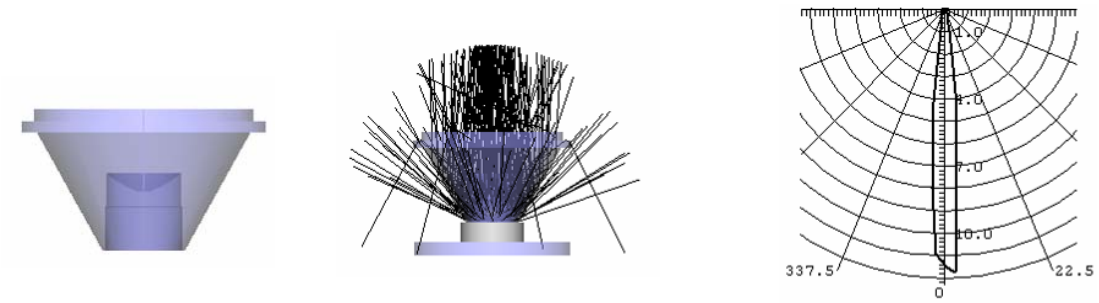


Fig. 60. Profile of the commercial optic (left); the optic's ray-tracing (middle); and the optic's intensity distribution (right).

The top flat portion of one optic was coated with YAG:Ce phosphor. Inside an integrating sphere, this coated optic was placed over a blue LED. The light output and the spectrum of this SPE package were measured at the LED's rated current (700 mA). The light output and the spectrum of the phosphor-coated LED and uncoated optic package were measured at the same LED drive current. The measurements showed that the efficacy for Package A was 26 lm/W, and the efficacy for the SPE package was 43 lm/W. Both packages had similar chromaticity values. Therefore, the SPE hypothesis seems to be supported: more photons are recovered with the SPE package compared with the typical commercial package.

Phosphor density effect

As observed in Fig. 49, the ratio for blue and yellow energy changes as a function of phosphor density. Therefore, the phosphor density of the SPE package can affect its chromaticity value and luminous output. Hence, another experiment was conducted to determine the optimum phosphor density by systematically varying the amount of phosphor and analyzing the resulting chromaticity.

Figure 61 illustrates chromaticity value and efficacy change as a function phosphor density. This experiment used a blue Luxeon I Star LED with a 455 nm peak wavelength, which had the same physical characteristics as the Luxeon III Star used in the optic modeling simulation. The phosphor densities were increased from 4 mg/cm^2 to 11 mg/cm^2 at a 1 mg/cm^2 interval. The results show that the package output color shifts to greenish-yellow when the density increases. As a result, the efficacy of the package increases with increasing density and then stabilizes around 11 mg/cm^2. It was also observed that the chromaticity values drift from the blackbody locus at low and high density values. For general illumination applications, it is almost always desirable to have a light source with a chromaticity near the blackbody locus; thus, there seems to be a trade-off between the chromaticity value and efficacy of a phosphor-based LED light source. The 8 mg/cm^2 density was selected as the best compromise because its chromaticity values are right next to the blackbody locus and its efficacy is just slightly lower than that at higher phosphor densities. Additionally, the SPE package with this density had a chromaticity very close to that of the Luxeon III Star white LED used as a reference for comparisons.

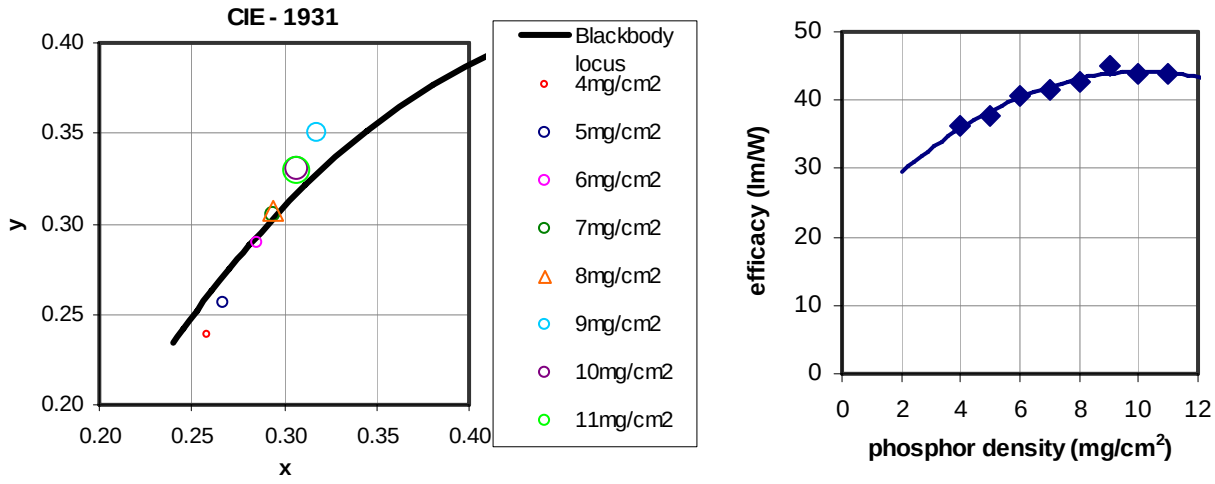


Fig. 61. Chromaticity values (left) and efficacy changes (right) as a function of phosphor density. (Source: 1-watt LED with 455 nm peak wavelength.)

White LED package comparison

The next step was to compare the SPE package with a commercial white LED package to determine the light output and efficacy gain for the SPE package. Twelve Luxeon III Star LEDs were purchased, six 3 W royal blue (455 nm peak wavelength) and six 3 W white. The white LEDs were fitted with an uncoated commercial optic, similar to Package A shown in Fig. 58. Their light output and spectrum were measured in the same integrating sphere used in previous testing, and the current and the voltage required to power the LEDs were also recorded. The same measurements were repeated for the SPE packages, which consisted of the blue LEDs fitted with a phosphor-coated optic at a density of 8 mg/cm^2.

Table 3 shows the results for all twelve white LED packages, typical and SPE, at equal power use. Figure 62 compares the efficacies of the individual packages. The average luminous flux and the corresponding average efficacy for the SPE LED packages are 90.7 lm and 36.3 lm/W, respectively. The average luminous flux and the corresponding average efficacy for the typical white LED packages are 56.5 lm and 22.6 lm/W, respectively. Therefore, the SPE LED packages on average have 61% more light output and 61% higher luminous efficacy. The variation of luminous flux and corresponding efficacy between similar LEDs was small, with a standard deviation of less than 4%.

Table 3. Photometric and electrical data for the twelve LEDs.

	Current (mA)	Voltage (V)	Power (W)	Luminous flux (lm)	Efficacy (lm/W)	CIE x	CIE y
SPE #1	700	3.568	2.50	91.0	36.5	0.2878	0.2960
SPE #2	700	3.561	2.49	90.9	36.5	0.2907	0.3097
SPE #3	700	3.586	2.51	92.0	36.6	0.2889	0.2986
SPE #4	700	3.594	2.52	93.2	37.1	0.2900	0.3000
SPE #5	700	3.571	2.50	89.4	35.8	0.2907	0.3107
SPE #6	701	3.539	2.48	87.9	35.5	0.2893	0.2984

Typical #1	645	3.891	2.51	58.3	23.2	0.3198	0.3335
Typical #2	665	3.759	2.50	55.8	22.3	0.3217	0.3336
Typical #3	655	3.818	2.50	54.3	21.7	0.3156	0.3243
Typical #4	640	3.917	2.51	54.8	21.9	0.3158	0.3239
Typical #5	640	3.897	2.49	56.2	22.5	0.3213	0.3357
Typical #6	675	3.716	2.51	59.6	23.8	0.3153	0.3277

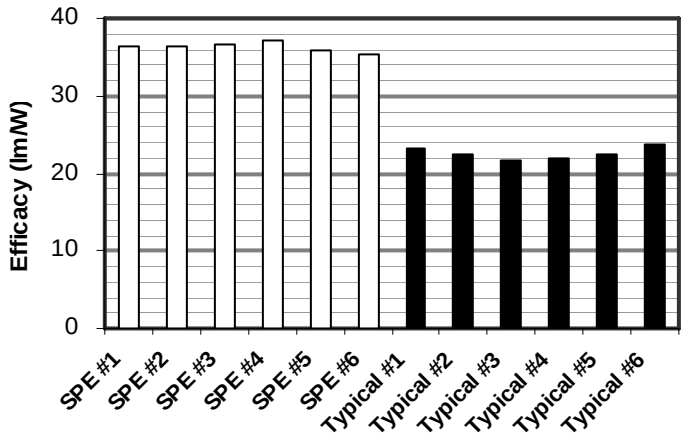


Fig. 62. Efficacy for the twelve packages, SPE and typical.

To study the impact of current on light output and efficacy, two LED packages from the above twelve, one typical white LED and one SPE package, were selected. These two LEDs were subjected to the same light output measurement procedure, but their input current was decreased from 700 mA to 50 mA in several steps, and the corresponding photometric and electrical data were gathered. Figure 63 illustrates the light output and efficacy of these two LED packages as a function of input current. At very low currents, the SPE package exceeds 80 lm/W, compared to 54 lm/W for the traditional package.

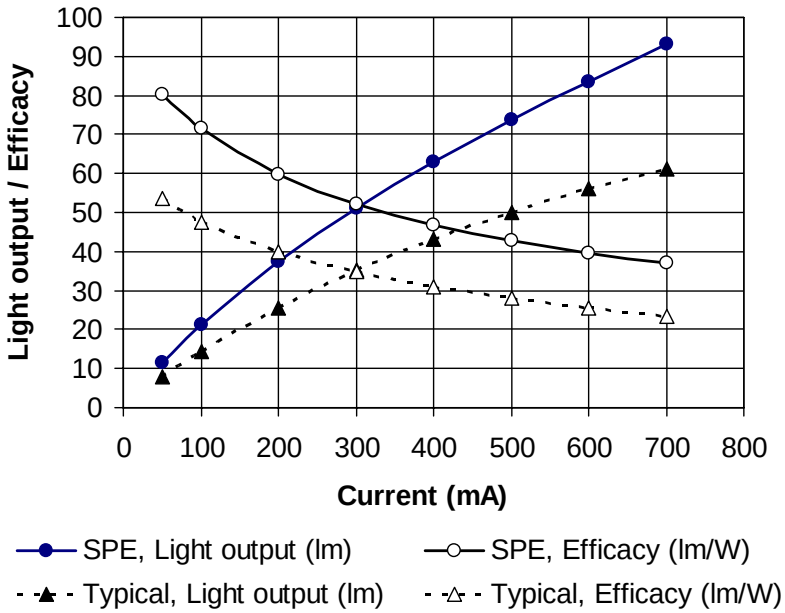


Fig. 63. Light output and efficacy of the two types of LED packages as a function of current.

LED fixture using SPE packages

Multiple SPE LEDs were packaged into a fixture and its performance was measured. The goal was to create an efficient and reliable white light source package using the SPE concept. Six 3 W blue LEDs were fitted with YAG:Ce-coated secondary optics and mounted inside a fixture housing with an aluminum heat sink and electronic driver (Fig. 64). The fixture array consisted of a machined reflector with 94% efficiency and a micro-lens diffuser with 93% efficiency. The reflector and micro-lens diffuser combined increase mix uniformity and direct light output in the desired direction. The interior mounting space for the SPE LEDs (*i.e.*, the reflector) was painted with a high-reflectance paint (>97%).

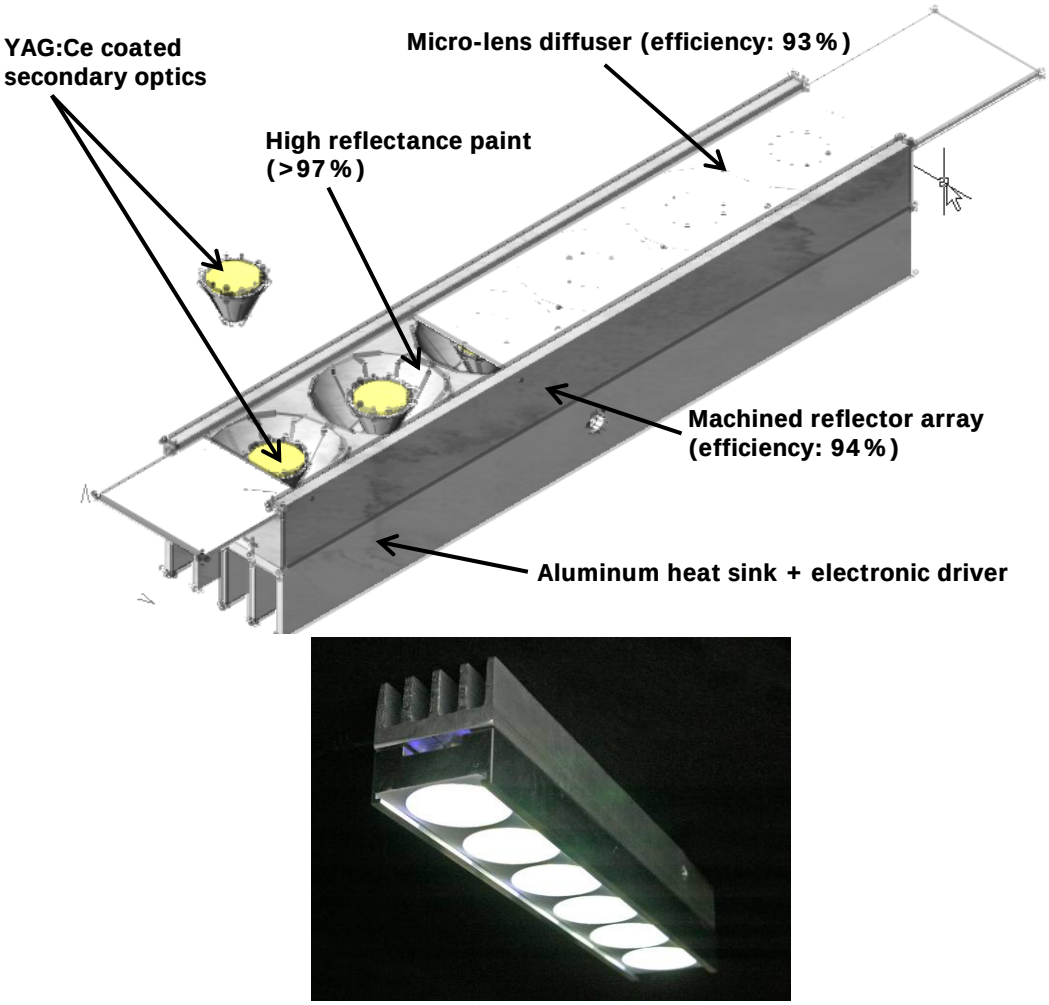


Fig. 64. Fixture incorporating six SPE LED packages. The micro-lens diffuser is not shown in the picture for clarity.

The efficacy, luminous flux, chromaticity coordinates (*x*,*y*), correlated color temperature (CCT), and color rendering index (CRI) of the SPE fixture were measured with an integrating sphere. Figures 65 and 66 illustrate the performance results. The fixture demonstrated the following:

- Efficacy: 36 lm/W (at 700 mA) to 78 lm/W (at 50 mA)
- Luminous flux: 66 lm (at 50 mA) to 541 lm (at 700 mA)
- CCT: ~6500 K
- CRI: > 70
- CIE x,y: x: 0.3084, y: 0.3414 without diffuser and
  x: 0.3139, y: 0.3513 with diffuser (at 700 mA in both cases)

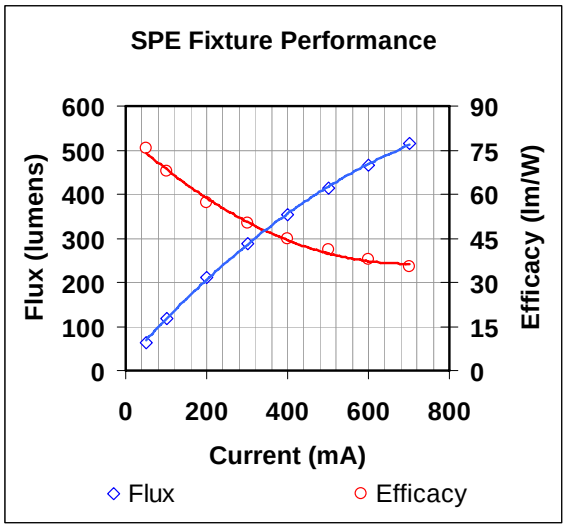


Fig. 65. Measured efficacy and flux for the SPE fixture.

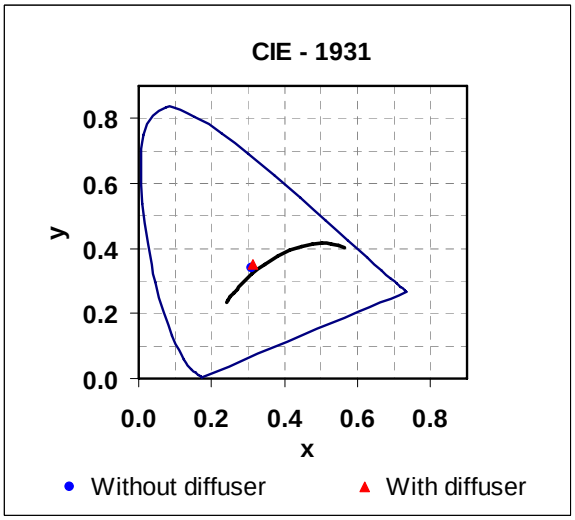


Fig. 66. Chromaticity coordinates of the SPE fixture with and without the micro-lens diffuser.

R.9 Understanding Source Form Factors for General Illumination

Task I: Ray-tracing analysis

As mentioned earlier, RCLEDs may be better suited for creating linear/tubular sources (like traditional linear fluorescent lamps). The goal of this task was to quantify and compare the efficiencies of a linear light source created by a RCLED and a traditional LED. LightTools software package was utilized to perform the ray-tracing analysis.

In this analysis, two types of packages were considered. In the first case, the die (RCLED or the traditional LED) was immersed inside a circular acrylic rod; in the second case, an encapsulated LED (RCLED and traditional LED) was placed in front of the acrylic rod to couple the light efficiently into the rod.

A) Die immersed inside the acrylic rod

A RCLED or a regular LED die was immersed inside one end of a 2-inch length circular acrylic rod. Figure 67 shows the setup of the optical model, which consists of the RCLED or traditional LED die, the acrylic rod, a far-field receiver, and a circular receiving plane close to the end surface of the rod. The far-field receiver estimated the overall light exiting the rod. The circular receiving plane estimated the light exiting the rod at the opposite end. All optical surfaces were set to have a TIR (total internal reflection) property in the software package. The ratio of the rays reaching the circular receiving plane to the far-field receiver shows the coupling efficiency of the die and rod package.

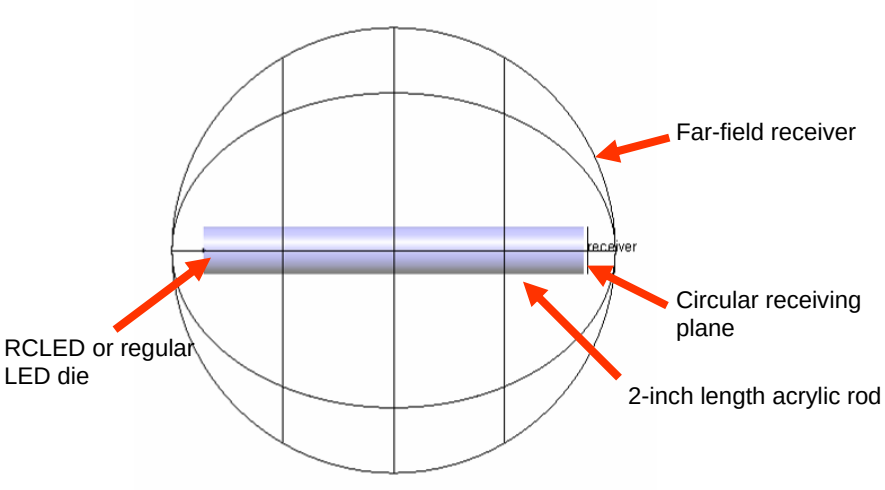
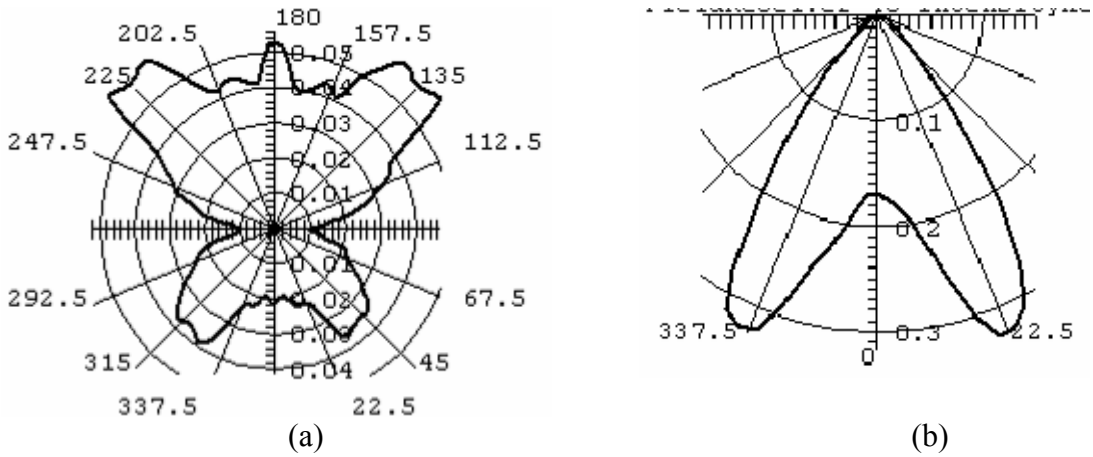


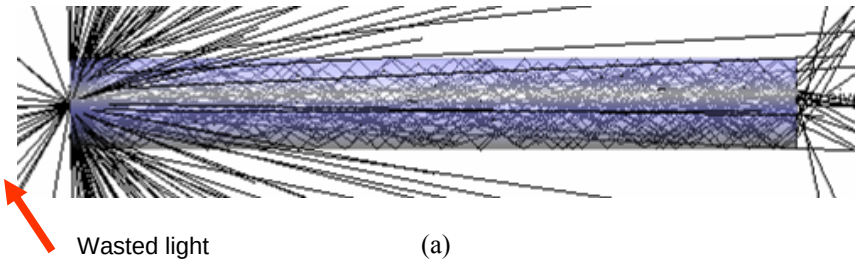
Fig. 67. Optical modeling setup.

Figure 68 shows the intensity distribution of a regular LED die and an RCLED die. Their optical modeling was covered in the second-year report. Figure 69 illustrates ray-tracings for the two setups. For a regular LED die, light can exit from all six surfaces. Therefore, part of the light exits from the left end of the rod and is wasted. However, for an RCLED, which has a narrow beam emitting in one direction, more light is coupled into the rod, allowing more light to exit from the right end of the rod.

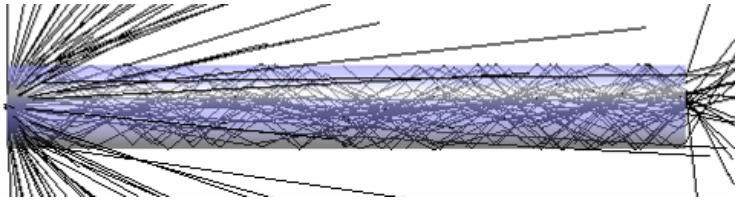


(a) (b)

Fig. 68. Intensity distribution (a) traditional LED die and (b) RCLED die.



(a)



(b)

Fig. 69. Ray-tracing for the modeling of (a) traditional LED die and (b) RCLED die with 0.25-in diameter acrylic rod.

Because the coupling efficiency depends very much on the diameter of the acrylic rod relative to the size of the LED, the coupling efficiency was estimated as a function of rod diameter. Figure 70 illustrates the results (coupling efficiency as a function of rod diameter) for both the RCLED and traditional LED packages. As seen in Fig. 70, the rod diameter affects the coupling efficiency for both packages. However, overall the RCLED package is about 60% more efficient than the traditional LED package. The coupling efficiency reaches a maximum value when the rod diameter reaches 0.1 inch, and remains constant beyond that for the RCLED. For the traditional LED, maximum efficiency is reached at 0.25 inch. This means that to obtain maximum efficiency with a traditional LED, the rod diameter must be at least 0.25 inch. With the RCLED, the rod diameter can be smaller, 0.1 inches.

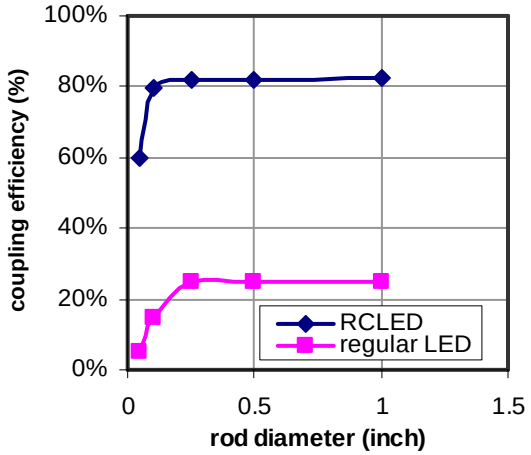


Fig. 70. Coupling efficiency as a function of rod diameter.

The above results are not surprising. For the traditional LED, the light exits the die in all directions and the angle at which the rays exit the die is larger than that of the RCLED. Furthermore, the beam of the RCLED is much narrower, and all the light exits in one direction.

B) Die immersed inside a typical epoxy dome

Usually, traditional LEDs (5-mm and HBLED) are packaged by placing the die inside a small reflector and covering it with an epoxy dome. This allows most of the light exiting the die to be captured and directed toward one direction. In this part of the study, the die was immersed inside a typical epoxy dome and was placed near the left end of the rod. Figure 71 shows the optical setup used in this analysis. In this setup, the far-field receiver estimated the rays from

both the rod and the encapsulated LED (RCLED and the traditional LED). Figure 72 illustrates the beam distributions of the two dies immersed inside the epoxy dome. The ray-tracing of the optical models are shown in Fig. 73.

Figure 74 illustrates the simulation results. Again, rod diameter is critical for the coupling efficiency of both encapsulated dies. With a larger diameter, more rays are coupled into the rod, and therefore, more rays exit from the right end of the rod. Once the rod reaches a certain diameter, the coupling efficiency will remain constant. As seen in Fig. 74, to achieve maximum coupling efficiency, the rod diameter has to be 0.25 inch for an encapsulated RCLED and 2 inches for a traditional LED.

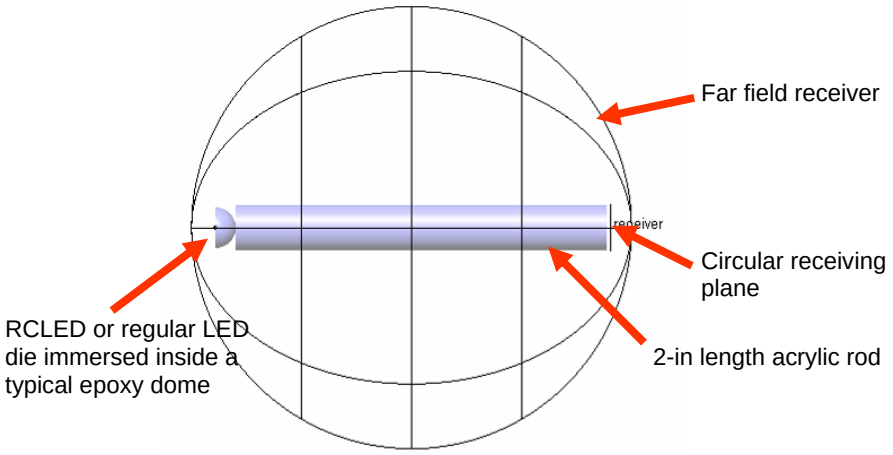
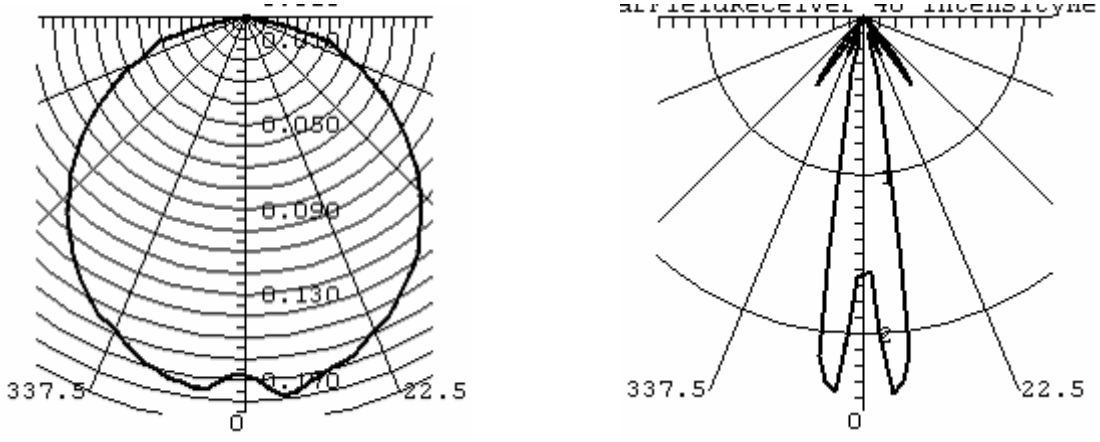
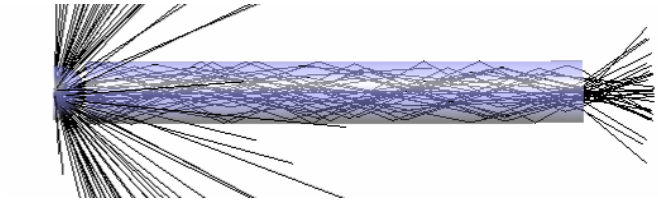


Fig. 71. Optical modeling setup.

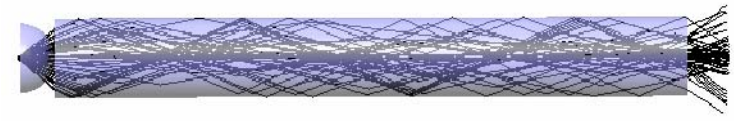


(a) (b)

Fig. 72. Intensity distributions of (a) regular LED die and (b) RCLED die immersed inside a typical epoxy dome.



(a)



(b)

Fig. 73. Ray traces for (a) regular LED die and (b) RCLED die with 0.25-inch diameter acrylic rod.

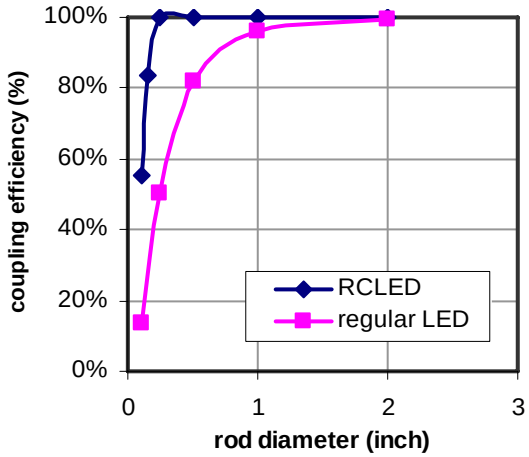


Fig. 74. Coupling efficiency as a function of rod diameter.

From this analysis we can infer that it is possible to achieve similar optical efficiencies with both types of LEDs (RCLED and traditional HBLED). However, the linear light source created with a traditional LED will be much larger in diameter, 2 inches or larger, compared to the one created with the RCLED, about 0.25 inch.

It is possible to create a high-efficiency, smaller-diameter linear light source with traditional LEDs by adding more optical components, like a reflector or a secondary lens. However, every time an additional optical component is included, it not only reduces the overall efficiency but also adds cost to the final system.

Finally, we can conclude that the RCLED offers greater benefits when creating a linear light source compared to the traditional LED, especially if smaller-diameter tubular sources are needed.

Task II: Human factors study

Typically, an office room in a commercial space is lighted using either point light sources (downlights) or linear/tubular light sources (light pipes), and both methods of lighting have their merits and demerits. As shown in Fig. 75 below, the room can be lighted with many small light fixtures (MR16 size HBLED fixtures), fewer medium size fixtures (PAR lamp size HBLED fixtures), even fewer large fixtures, or just one or two diffused linear fixtures (mimicking RCLED fixtures using HBLEDs and light pipes).

Human subjects can react differently to such application styles with different sizes and number of fixtures. The question is what type of lighting is optimum for the target application. Therefore, an experiment was designed to determine the optimum dimension of a fixture for general lighting in a commercial setting. Gaining a better understanding of occupants' preferences for lighting application styles would make the implementation of solid-state lighting systems, including RCLEDs and HBLEDs, to commercial lighting applications practicable.

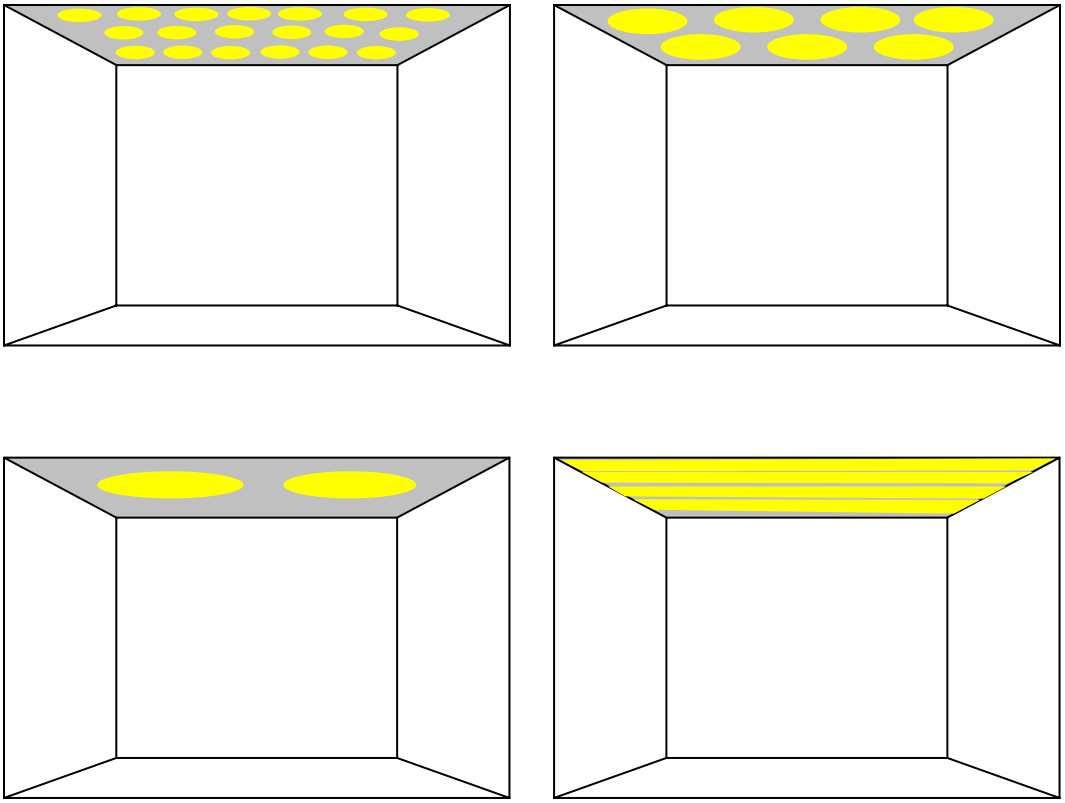


Fig. 30. Different general lighting configurations.

Lighting requirements

To achieve good-quality interior lighting with LED luminaires, it is first essential to satisfy lighting requirements for visual tasks by providing appropriate illuminance while avoiding negative factors such as glare, reflections, and harsh shadows. Creating a good mood in an interior space also is necessary, and many studies already have identified brightness perception and visual interest as key factors that influence the mood of lighting [Flynn 1975], [Flynn 1977],

[Bernecker 1985], [Loe 1994], [Tiller 1995]. In interior spaces where verbal communication is important, lighting also should provide appropriate facial modeling.

Considering these issues, the question then is which type of the LED application can best satisfy these lighting requirements? One merit of using an LED light pipe is that it can create a uniform illuminance distribution over the room. Conventional applications of light pipes typically have been restricted to large, high-bay spaces, including subway stations and factories, where the relatively large light source, around 5-6 inches in diameter, can be regarded as a linear source. Therefore, an LED light pipe may not be suitable to a smaller space such as an office room due to its oversize profile. However, it is necessary to identify if the merits of light pipes can overcome the downside of its size in an office context.

On the other hand, downlights are already used in offices and may be a more suitable way to apply LEDs to interior lighting. However, LED lamps are different from conventional light sources used for downlights, such as incandescent lamps and fluorescent lamps. Each LED lamp has a lower output, a more directional distribution, and a higher maximum luminance than conventional lamps. Therefore, it is necessary to use a larger number of LED lamps with carefully designed optics to provide an appropriate luminous flux, reduce the maximum luminance, and widen the distribution. However, it is not clear how LED lamps should be integrated into each downlight unit. To provide a certain luminous flux with LED lamps, it is possible either to put all LED lamps into a single, larger downlight or to scatter the same number of LED lamps over the ceiling with a series of smaller downlights. Generally, as the size of a light source increases, the light source becomes more glaring [Petherbridge 1950]. At a certain luminance, the smaller the size of the light source, the less glare it will produce [Einhorn, 1991]. However, using smaller light sources necessitates the use of many light sources to achieve a certain illuminance. Many light sources recessed in the ceiling may visually annoy people. A large number of light sources also requires a lot of luminaires, which is not a practical, efficient way to illuminate an office. Therefore, the optimization of the number, and therefore the size, of light sources is the key to successfully applying LEDs to general lighting.

Objectives

To identify the most appropriate way to apply LEDs to general interior lighting, this study consisted of two experiments—a mockup experiment and a scale model experiment. The mockup experiment compared point and liner sources, or downlights and light pipes. For downlight applications, appropriate ranges of aperture size and number of fixtures were addressed in terms of preference and glare. To verify the validity of the results of the glare evaluations, they were compared with calculations using the glare standard formula.

The second experiment used a scale model to easily control independent variables including number, size, and density (spacing) of downlight luminous elements. Finally, recommendations for developing LED downlights and designing interior lighting with LED downlights are provided.

Mockup experiment

To compare the two application styles—downlight (point source) and light pipe (linear source)—a mockup experiment was conducted. Another objective of this study was to identify the optimal number of downlight fixtures and their aperture size.

Experimental setup

This experiment took place in a corner of a laboratory room at the Lighting Research Center in Troy, N.Y. Figure 76 shows the plan and a general view of the experimental setup. The dimensions of the corner were 7'10" (2.4 m), 7'4" (2.23 m), and 8'11" (2.72 m) for the length, width, and height, respectively. The corner had walls on two adjacent sides and a ceiling-to-floor fabric partition on the third, longer side. The fourth side was left open for the subjects to enter and evaluate the different conditions. All wall surfaces were white, with a reflectance of 80%. The floor was carpeted, with a reflectance of 25%, and the ceiling consisted of generic acoustic mineral-fiber tiles with a reflectance of 75%.

In the ceiling, two types of LED applications, the downlights and the light pipes, were presented. Because LED lamps do not easily maintain sufficient luminous flux while varying the size and number of the luminaires, this experiment used fluorescent lamps in place of LED lamps. A correlated color temperature (CCT) of 6500 K was chosen for the fluorescent lamps because current white LED lamps typically produce higher CCTs than those of conventional fluorescent lamps. For the downlight application, the fluorescent lamps were housed inside two 2' by 4' rectangular luminaires centrally located on the ceiling and placed side by side to form a 4' by 4' luminaire. A diffuser panel was mounted to the opening of each luminaire to create a uniform, broad light distribution in the room. Each luminaire had six T8 fluorescent lamps to create a high luminance of 3500-4500 cd/m^2, equivalent to that of an LED downlight prototype using 3W LED lamps with a diffuser (transmittance = 50%) when the diffuser surface is measured at an angle of 45 degrees from the nadir. Below the diffuser panel was mounted a white foam board panel with square openings cut out to create a downlight layout. Five panels, or five different downlight layouts, were prepared. By replacing the panels, the downlight layout was changed. The panels were mounted with the help of Velcro tape along the outer periphery of the luminaire and panel.

For the light pipe application, two light pipes were suspended from the ceiling. Each light pipe was composed of a transparent polycarbonate tube with a diameter of 4" (10 cm) and a length of 4'1" (1.32 m), a pair of sockets, a pair of plastic end-caps, two layers of diffuser films, and a fluorescent lamp with a CCT of 6500 K (OSRAM SYLVANIA). The surface of the light pipe had an approximate luminance of 3500 cd/m^2, which was about half that of the downlight conditions. Figure 77 shows a view of the light pipe condition.

A 49 cm × 39 cm mirror was hung on the wall at a height of 150 cm measured at the center of the mirror and opposite to the entry point, allowing participants to evaluate facial modeling in their own faces.

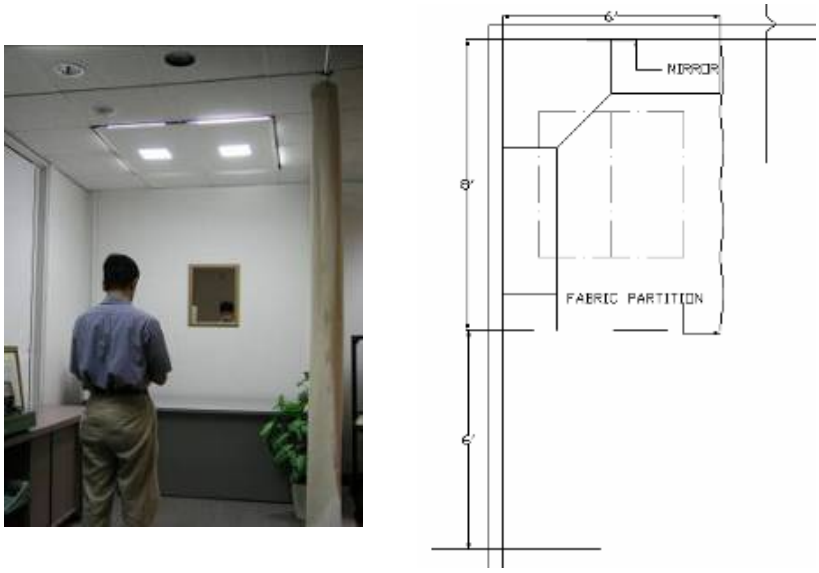


Fig. 76. The plan and view of the experimental setup.



Fig. 77. A view of the light pipe condition.

Experimental conditions

The independent variable employed in this experiment was the luminaire type (the light pipe and the downlight). The size and number of downlights were synchronized to keep the total luminous surface area constant across all downlight conditions, therefore maintaining a constant total luminous flux and horizontal average illuminance. As the number of downlight luminaires increased, the size of each fixture decreased. Table 4 shows the six experimental conditions—five different downlight arrangements and one light pipe arrangement. Appendix 1 shows a view of each arrangement.

Table 4. Lighting conditions used in the experiment.

Luminaires*[1]	**1 DL-2**	**2 DL-6**	**3 DL-12**	**4 DL-24**	**5 DL-48**	**6 LP-2**
Number	2	6	12	24	48	2
Side (cm)	20.4	12.0	8.5	6.0	4.2	D*[2]: 10
Area (cm^2)	416	144	72.25	36	17.64	L*[3]: 124
Spacing (cm): widthwise	61	61	30.5	30.5	15.2	100
lengthwise	-	30.5	30.5	20.5	15.2	-
Total area (cm^2)	832.32	864	867	864	846.72	NA
E_{avg} (lx)	275	265	261	250	220	260

*1: DL = downlights and LP = light pipe
*2: D is the diameter of the light pipe
*3: L is the length of the light pipe

Square openings were cut out on a 4’ by 4’ white foam board to resemble LED downlight luminaires. Five arrangement patterns were created with the foam board panels. For each pattern, the total surface area of the openings was kept as constant as possible to 128 square inches (82,500 mm^2). The opening sizes were chosen because they consistently produced an average illuminance of approximately 250 lx on the desk. Measured illuminance levels are also shown in Table 4. Each value is the mean of nine measurements.

Procedure

To minimize the time needed for evaluation and therefore reduce the fatigue of subjects, this experiment was divided into two sessions—one for the downlights and the other for the light pipes. In the first session (downlight evaluation), 20 subjects, 12 males and 8 females aged between 22 and 60 years, participated and evaluated Condition 1 (DL-2) through Condition 5 (DL-48). In the second session (light pipe evaluation), 22 subjects evaluated Condition 1 (DL-2), Condition 4 (DL-24), and Condition 6 (LP). Conditions 1 and 4 were evaluated again with the light pipe condition for a comparison with the evaluation results from the first session. This comparison allowed for identification of the consistency of subject evaluations between the first and second sessions. The order of the experimental conditions was counterbalanced across subjects as much as possible.

This evaluation used a questionnaire (Appendix 2). Each questionnaire sheet had two parts. The first part of the questionnaire was composed of 12 contrasting word pairs to describe the mood of the room. Each word pair had a seven-point scale, from -3 to +3, and subjects were asked to evaluate the lighting condition using the word-pair scale. The second part of the questionnaire asked detailed questions about appropriate applications, shadows, facial modeling, and the appropriateness of the number of light sources. Each of the four detailed questions used a five-point scale from -2 to +2.

In each session, subjects were divided into groups of four. Before the arrival of each group, two experimenters set the first experimental condition into the ceiling. At the arrival of each group, the experimenters gave the subjects instructions and a set of questionnaire sheets. Then, the subjects moved to the experimental setup with the questionnaire. During the evaluations, the subjects were allowed to stand outside of the experimental setup so that they could view the whole room. The subjects also were allowed to walk around the inside of the experimental setup so that they could investigate shadows and facial modeling under a given lighting condition. However, the subjects were not allowed to talk about the lighting with each other.

After all subjects completed the questionnaire, the experimenters changed the experimental condition to the next one while the subjects waited in the adjacent area. The participants were again asked to evaluate the lighting with the new condition. This procedure was repeated until all five conditions were evaluated. The entire session took about 15 minutes for each group of subjects—1.5 minutes to change each panel and about 2 minutes for the subjects to evaluate the lighting and fill out the questionnaire. The second session, which had only three conditions, took subjects less than 15 minutes to complete.

Results

For each of the 12 contrasting word pairs on mood and four detailed questions, subjective evaluations were quantified by calculating a mean rating on a seven-point scale from -3 to 3. Table 5 summarizes the results, means, and standard deviations for the 12 statement pairs. Appendix 3 depicts a graph for each contrasting word pair using the same data listed in Table 5. Appendix 3 also shows the results of the detailed questions. The mean ratings in Table 5 do not indicate any strong tendencies, *i.e.*, all mean responses on a seven-point scale (-3 to +3) are around neutral, ranging from -0.4 to 1.68. This suggests that all lighting conditions used in this study were fairly acceptable.

Table 5. Results of evaluations.

	1:DL-2		2:DL-6		3: DL-12		4:DL-24		5:DL-48		6:LP-2	
	Mean	**S.D.**	**Mean**	**S.D.**	**Mean**	**S.D.**	**Mean**	**S.D.**	**Mean**	**S.D.**	**Mean**	**S.D.**
Dim/Bright	1.30	1.17	1.05	1.05	1.40	0.88	0.90	1.41	0.50	1.47	0.09	1.41
Non-uniform/Uniform	1.65	1.18	1.35	1.18	1.35	1.04	1.60	1.19	1.35	1.23	1.68	1.04
Boring/Interesting	-0.40	1.14	0.25	1.41	0.75	1.12	0.38	1.41	0.85	1.73	0.05	1.29
Private/Public	0.40	1.67	0.45	1.23	0.60	1.50	0.35	1.46	-0.25	1.52	0.32	1.04
Simple/Complex	-1.05	1.15	0.05	1.32	0.15	1.31	0.65	1.42	0.60	1.98	-0.73	1.35
Unpleasant/Pleasant	-0.10	1.29	0.45	1.32	0.65	1.35	0.25	1.33	0.55	1.47	0.14	1.28
Somber/Cheerful	-0.35	1.35	-0.05	1.19	0.45	1.28	0.20	1.15	0.10	1.41	-0.36	1.36
Confined/Spacious	0.25	1.62	0.00	1.17	0.60	1.43	0.15	1.50	-0.30	1.53	0.55	1.44
Gloomy/Radiant	0.20	1.28	0.10	1.29	0.50	1.15	0.40	1.43	0.15	1.35	-0.23	1.11
Subdued/Stimulating	-0.10	1.33	0.05	1.32	0.10	1.29	0.13	1.36	0.25	1.37	-0.43	1.08
Glary/Comfortable	-0.25	1.48	0.45	1.39	0.50	1.43	0.70	1.53	0.70	1.53	0.86	1.25
Dislike/Like	-0.20	1.40	0.40	1.47	0.65	1.57	-0.05	1.76	0.30	1.84	0.00	1.45

To avoid redundancy of analyses, this report focused on four pairs: “Dim / Bright,” “Boring / Interesting,” “Glary / Comfortable,” and “Dislike / Like” among the 12 word pairs. These four were selected because to achieve good-quality lighting, it is first important to remove the negative factor: glare. Second, to provide good mood through lighting, two factors, brightness perception and visual interest, are important, as many studies have suggested [Bernecker 1985], [Flynn 1975], [Flynn 1977], [Loe 1994], [Tiller 1995]. Finally, as comprehensive evaluations, subjective preferences of subjects were investigated though the evaluations of “dislike / like.” Other evaluations showed similar tendencies to these four representative factors (the similarity is discussed later in *Classification of evaluations*). Therefore, analyses on those evaluations were omitted from this report.

To answer the question of what application style is preferred (point sources or linear sources), the evaluations of the light pipe (linear source) were first compared with those of the downlight (point source).

Downlight (point source) and light pipe (linear source) comparison

To identify an appropriate application style, the results of the evaluations for the above-described four requirements—glare, brightness, visual interest, and preference—were compared between downlights and light pipe lighting applications. The evaluations of “appropriateness for office” also were analyzed as another comprehensive evaluation. Figure 78 (a), (b), (c), (d), and (e) show the results, and suggest that the light pipe was the least appropriate for an office, the dimmest condition, and less interesting and less preferred than most downlight conditions. Reasonably, regarding glare the light pipe condition ranked as the most comfortable lighting condition among the six experimental lighting conditions. This is because the luminance of the luminous element, or the light pipe surface, was lower in this condition than in the other conditions. Statistical analyses supported the results of the study.

These results led to the conclusion that the light pipe is not appropriate for commercial applications. Thus, further analyses on the appropriate number and size of fixtures focused on the results for downlights. In the future studies, however, it is still important to prove these tendencies with various sizes and luminances of light pipes, since this experiment used limited variations of the light pipe application style.

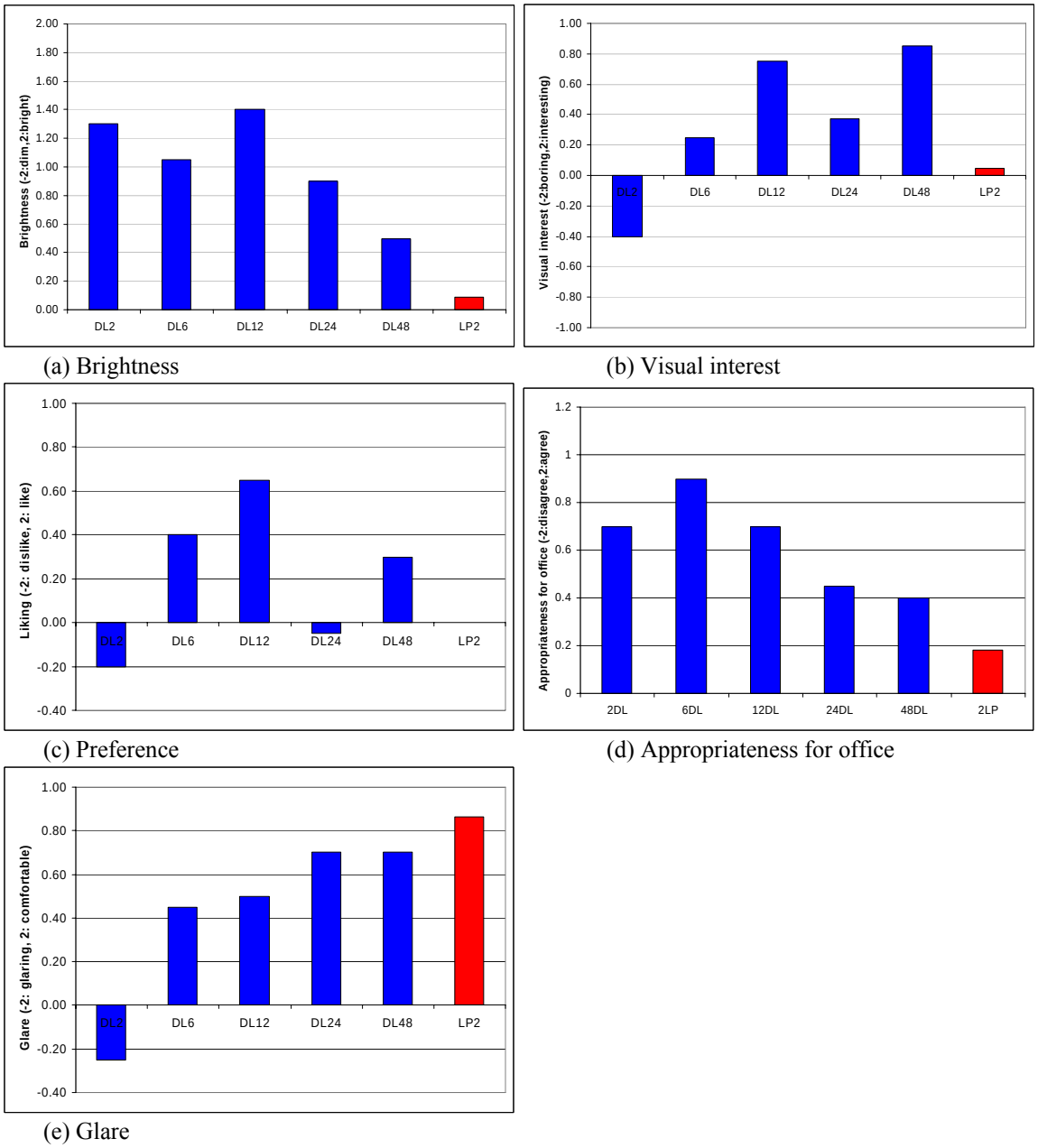


Fig. 78. Comparisons of evaluations between light pipe with downlights.

General tendencies of evaluations for downlights

Prior to investigating the appropriate number and size of fixtures, the four word pairs on brightness, visual interest, glare, and liking were addressed to understand the general tendencies of evaluations for only downlights (see Fig. 78). To investigate how significantly the experimental lighting conditions affected each evaluation, a one-way analysis of variance (ANOVA) was applied to all subject ratings for the downlights. Table 6 summarizes the results (p-values) of the ANOVAs.

(1) Dim / Bright

The results of the ANOVA showed there is a statistically significant effect of lighting on the brightness perception ($p<0.05$). The evaluation results clearly show that the room appeared dimmed when it was illuminated by the light pipes. The third condition with 12 luminous elements gained the highest rating among the six lighting conditions. After the peak, perceived brightness decreased as the number of luminous elements increased.

(2)Boring / Interesting

Overall, as the number of the luminous elements increases, the room appears more interesting. The fifth lighting condition (DL-48) with 48 luminous elements in the ceiling obtained the highest rating among the six lighting conditions. Although the results of the overall ANOVA suggested no significant main effect of the lighting conditions, Condition DL-48 was rated as a significantly, visually interesting condition compared to other lighting conditions, such as the DL-2. This implies that the fewer the number of luminous elements, the less interesting the room will appear.

(3) Glare / Comfortable

An overall tendency found was that as the number of luminous elements increased (*i.e.*, the size of each element decreased), the room became more comfortable. This tendency is consistent with that of existing studies [Petherbridge 1950], [Einhorn, 1991]. Although the ANOVA suggested no statistically significant main effects of the element number on the glare evaluations, results of t-tests suggested that Condition DL-48 was rated as a more comfortable condition than Condition DL-2 ($p<0.05$). On the other hand, the differences between DL-48 and DL-24, DL-12, and DL-6 were not significant.

(4) Dislike / Like

There appears to be a peak at a number of fixtures of 12. However, if the number exceeds the peak, the preference ratings become worse. The worst rated fixture number was 24. This rating is probably because in this condition, the fixtures were not evenly distributed over the ceiling, which increased the luminance contrast and made the background where no fixtures were located appear dim and gloomy.

Table 6. Results (p-values) of ANOVAs in the first and second sessions. P-values below 0.05 indicate significance.

Subjective evaluations		p-value
Dim/Bright		0.030*
Non-uniform/Uniform		0.841
Boring/Interesting		0.007**
Private/Public		0.075
Simple/Complex		<0.001**
Unpleasant/Pleasant		0.184
Somber/Cheerful		0.104
Confined/Spacious		0.090
Gloomy/Radiant		0.462
Subdued/Stimulating		0.705
Glary/Comfortable		0.092
Dislike/Like		0.207
Appropriate applications	**Office**	0.309
	Residential	0.483
	Commercial	0.406

Shadows	0.710
Facial modeling	0.751
Number	<0.001**

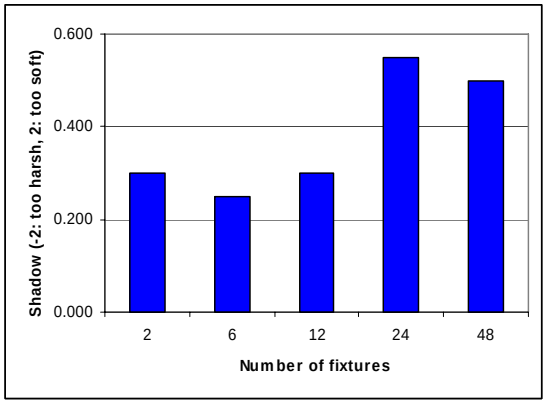
(5) Other detailed questions

In addition to the 12 word pairs, four detailed questions on appropriate applications, shadows, facial modeling, and number of light sources were given to subjects. The results of the four detailed questions were also quantified by calculating a mean rating on a five-point scale. Figure 79 (a), (b), and (c) show the results of those questions. The responses to the questions on appropriate applications were shown in Figure 78(d).

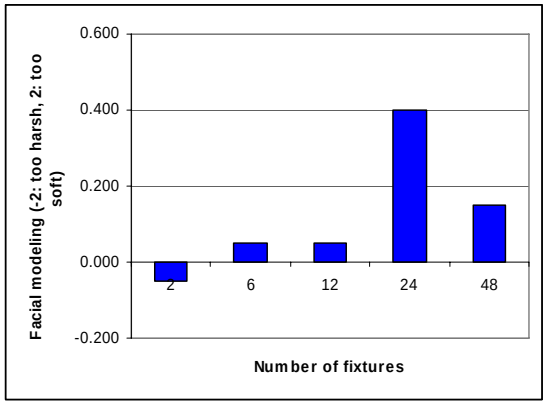
On the appropriateness of lighting conditions for office applications, Conditions 1 (DL-2), 2 (DL-6), and 3 (DL12) were rated as the most appropriate lighting conditions; the condition with six luminous elements was rated as the best.

With regard to the shadow and facial modeling evaluations, both evaluations showed a similar tendency in that as the number of luminous elements increased, the shadows and facial modeling became softer. Interestingly, the peak of the softness was placed at a luminous element number of 12 instead of 48. Condition 6 (LP-2) was rated as the harshest shadow and facial modeling condition. This may be because of the low mounting heights of the suspended light pipes, whereas the other luminaires of Conditions 1 to 5 were all recessed in the ceiling. Overall, most downlight conditions except Conditions 4 (DL-24) and 5 (DL-48) seem to provide appropriate shadows and facial modeling.

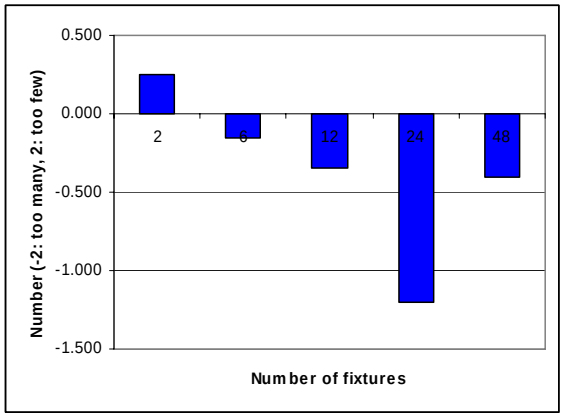
As for the final question on the appropriateness of the number of luminous elements, all lighting conditions except Condition 4 (DL-24) were rated as appropriate. In general, as the number of luminous elements increases, the room starts appearing to hold too many luminous elements. However, it is not clear why the fifth condition (DL-48) with the largest number of luminous elements was rated better than Condition 4 (DL-24).



(a) Shadow



(b) Facial modeling



(c) Appropriateness of light source number

Fig. 79. Results of detailed questions.

Appropriate number of fixtures and aperture size for downlights

To identify an appropriate range of downlight number and aperture size, the probability (percentage) of agreements were calculated for brightness, visual interest, preference (liking), glare, and appropriateness of number of fixtures. The first four of the five were selected for the same reasons as described above. The appropriateness of number of fixtures was chosen because it is the most important for this analysis. Figure 80 shows the probability of agreements as functions of the number of fixtures.

Figure 80 shows that as the number of fixtures increases, ratings of both perceived brightness and glare reduce, while ratings of both "too many" and visual interest increase. In terms of preference ("liking"), there appears to be a peak for the number of fixtures. The peak is located at a fixture number around eight.

To identify the most appropriate range in number of fixtures, the 70th percentile values were compared between the five subjective evaluations. The comparisons led to a range between 6 and 15 as the optimum number of fixtures. The green shade in Figure 80 indicates the range in which all five ratings exceed the 70th percentile.

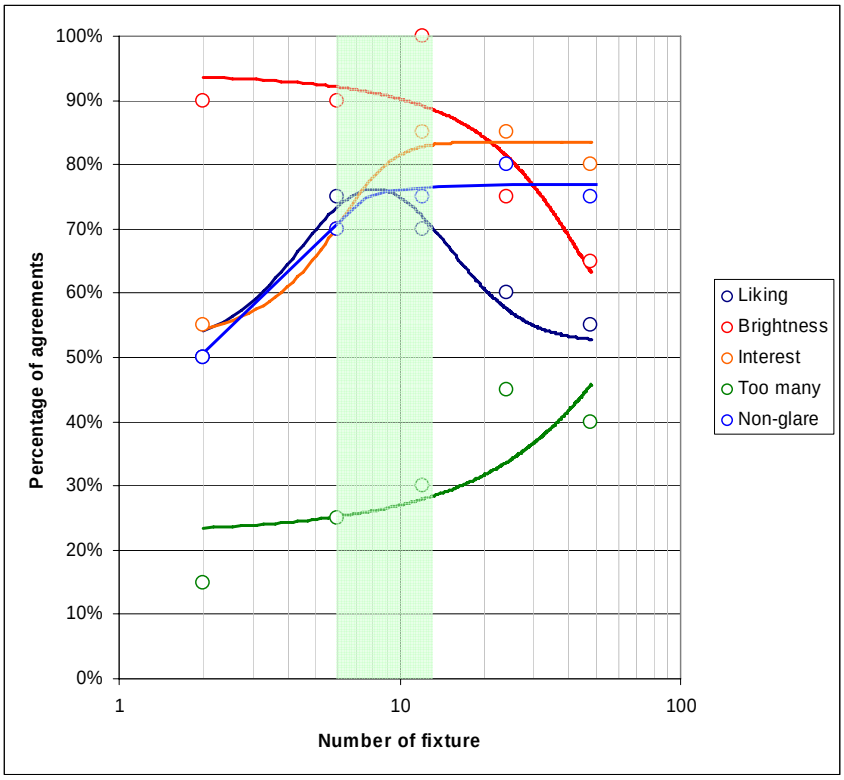


Fig. 80. Results of probability of agreements. The green shade in the graph shows the range in which all five ratings exceeded the 70th percentile.

Classification of evaluations

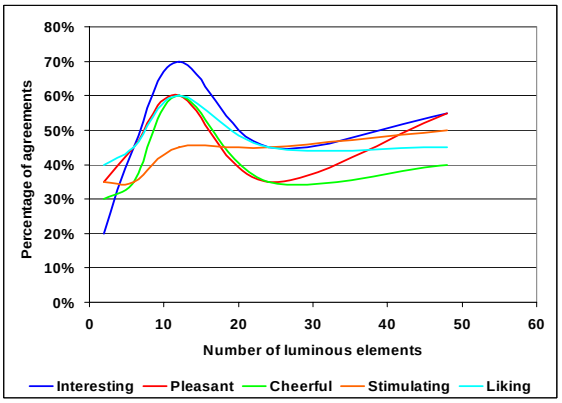
To better understand the tendency of subjects' agreements with each contrasting word pair, the probability of agreements was calculated in such a way that all responses above "0: neutral" were treated as positive responses. Then, a hierarchical cluster analysis was applied to all contrasting word pairs. The results of the analysis clustered them into four groups—Group 1: "boring/interesting," "unpleasant/pleasant," "somber/cheerful," "subdued/stimulating," and "liking"; Group 2: "private/public," "spacious," and "gloomy/radiant"; Group 3: "simple/complex" and "too-few/too-many"; Group 4: "dim/bright," "non-uniform/uniform," and "glaring/comfort." Each diagram in Fig. 81 shows one of the four clustered groups. The characteristics of groups are listed below:

Group 1: First, as the number of luminous elements increases, ratings are raised. However, each probability line declines after a peak at an element number of 12. The word "interesting" may represent this group. Too few or too many downlight luminous elements bore subjects but if the element number equals 12, the layout of downlights seems to interest them the most.

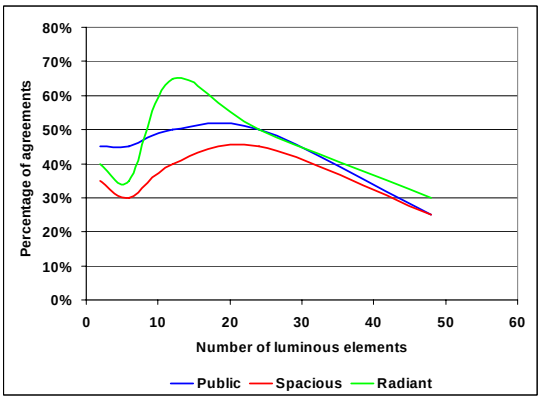
Group 2: The word "spacious" may represent this group. The peak comes a little slower than in Group 1 as the number of luminous elements increases. When the number of elements becomes too many, the feeling of spaciousness is reduced.

Group 3: This group seems to directly connect to the number of elements. As the number increases, the evaluations improve.

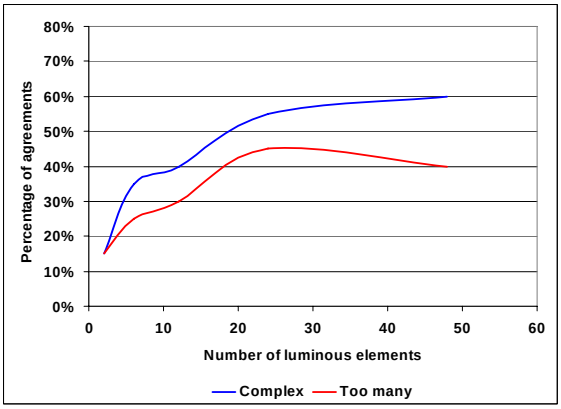
Group 4: The words in this group relate to each other more subtly than those in the other groups. The uniformity and brightness evaluations seem to gradually decline as the number of elements increases. The sensation of glare is also, but more sharply, decreased as the number of elements increases. This is because the size of elements is reduced as the number of elements increases in this experiment. The relationship between the size and glare sensation will be discussed later.



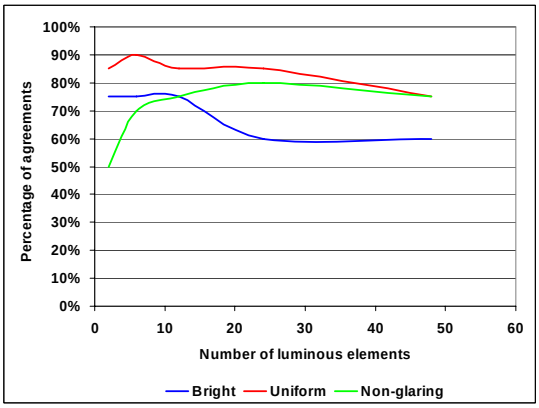
(1) Group 1



(2) Group 2



(3) Group 3



(4) Group 4

Fig. 81. Results of clustering.

Evaluations of glare

To identify how the number and size of LED light fixtures affect glare sensation and to find an effective way to minimize glare by manipulating the number and size of LED light fixtures, glare calculations were conducted by using the Unified Glare Rating (UGR).

Unified Glare Rating (UGR)

Over the last five decades, many studies attempted to identify factors determining glare sensation and developed glare functions to quantify glare experiences [Hopkinson 1957], [Luckiesh 1949]. Based on the results of the studies, the UGR was approved as a standard glare evaluation system by the International Commission on Illumination (CIE) in 1995 [CIE 1995].

Appendix 4 shows the UGR formula. The UGR suggests the following general tendencies on glare sensation:

- Determinants of glare caused by a light source are the luminance, size, and background luminance of the light source and the angular displacement of the light source from the line of sight.
- Glare sensation from a light source increases as the luminance and the size increases.
- Glare sensation from a light source increases as the background luminance and the angular displacement decreases.
- The contribution of luminance of a light source to glare sensation is larger than the contribution of the size or the background luminance.
- Glare sensation is additive, *i.e.*, glare from multiple light sources in a space is equivalent to the sum of glare of individual light sources in the space.

However, the UGR can be applied to light sources larger than 0.005 m^2 only. The UGR, if it is applied to smaller light sources, often overrates glare from a very small light source. Many studies have already addressed this problem on such small light sources [Hopkinson 1957], [Putnam 1951], [Einhorn 1991]. Based on a recent study [Paul 1999], a supplemental UGR formula has been recommended by the CIE [CIE 2002].

Recommendation of supplemental UGR formula for very small light sources

The CIE has recommended a modified UGR formula for small light sources [CIE 2002]. This modification was done based on the study conducted by Paul and Einhorn (1999) as described above. The results of the study showed that for interior lighting distances, small light sources have a constant effective area, as seen by the average observer, when viewed off the line of sight. One can assume for normal interior lighting dimensions that the effective area of a small source does not change and can be taken as 0.005 m^2—this area corresponds to a downlight diameter of 8 cm when an observer looks at it from just below. Glare from small light sources positioned >5° off the line of sight is determined by their intensity (I) toward the eye. Their luminance (L) in the UGR glare formula is defined as:

$$L = I / 0.005 = 200I \qquad (1)$$

$$\omega = 0.005 / R^2 \qquad (2)$$

where ω is the solid angle size of a small light source as seen, and R is the distance of the light source from the eye. Therefore, the glare defining term in the UGR formula can be transformed:

$$L^2\omega / p^2 = 200I^2 / (R^2 p^2) \qquad (3)$$

where p is the position index, which provides a weighting index as a function of displacement of a tested light source from the line of sight.

Potential measures to reduce glare

The most effective way to ease glare from an LED downlight is to reduce its luminance. However, to make the best use of the flexibility in the size of LED lamps, the use of small-sized LED downlights is an option for glare reduction. As already described, to provide a certain

luminous flux with LED lamps, it is possible either to put all LED lamps into a single, larger downlight, or to scatter the same number of LED lamps over the ceiling with a series of smaller downlights.

At a certain luminance, the smaller the size of the light source, the less glare it will produce. However, using smaller light sources necessitates the use of many light sources to achieve a certain illuminance. According to the UGR formula, the additive feature of glare sensation means that the glare in both cases may not significantly differ from one another. However, as the modification of the UGR formula for very small light sources describes, if the size of the LED downlights is smaller than the threshold for "very small" light sources, glare would be reduced significantly.

Glare calculation

This calculation refers to the CIE supplemental recommendation of the UGR for small light sources [CIE 2002] — Equations (1), (2), and (3). To apply the above described recommendation for the UGR of small light sources to LED downlight evaluations, this study used five of the six conditions employed in the first experiment. This allows for a comparison between the results of the calculations and the evaluations. Table 7 shows the details of these five experimental conditions, corresponding to the conditions of DL-2, DL-6, DL-12, DL-24, and DL-48 (see also Appendix 1).

Table 7. Lighting conditions used in the experiment.

Luminaires	**1** **DL-2**	**2** **DL-6**	**3** **DL-12**	**4** **DL-24**	**5** **DL-48**
Light source number	2	6	12	24	48
Side of source (mm)	204	120	85	60	42
Area ($\times 10^{-3}$ m^2)	41.6	14.4	7.2	3.6	1.8
Total area ($\times 10^{-3}$ m^2)	83.2	86.4	86.7	86.4	84.7
E_{avg} (lx)	275	265	261	250	220
Luminance (cd/m^2)	4,000	4,000	4,000	4,000	4,000
UGR	25.1	25.0	25.2	24.0	21.9

In the above described recommendation, a "small" light source is defined by a projected area $A_p < 0.005$ m^2. Hence, among the experimental conditions, the light sources for DL-24 and DL-48 can be regarded as "small" light sources. Equation (3) was applied to these conditions. For the other conditions, the conventional UGR formula was applied. In the calculations, it was assumed that the luminance of the light sources is constant at a luminance of 4000 cd/m^2. This luminance approximately corresponds to the median luminance of the light sources used in the first experiment and also corresponds to the average luminance of a diffuser surface (reflectance = 50%) of a current LED downlight prototype with 3W white LED lamps when it is measured at an angle of 45 degrees from nadir. It was also assumed that observers stood below the center of the ceiling plate and looked up at the central point. This assumption on the observation represents the most critical scenario, allowing the highest UGR value for each experimental condition. The luminous intensity of the light sources for the conditions of DL-24 and DL-48 was calculated using Equation (4):

$$I = L \cdot A_p \qquad (4)$$

where A_p is a projected area of each light source.

The results of the calculations are shown in Table 7. Figure 82 compares the results of the UGR calculations with the results of the glare evaluations. With regard to the relationship between subjective glare ratings and UGRs, a study found the borderline between comfort and discomfort (BCD)[1] to be around a UGR of 19 [Luckiesh 1949]. A UGR of 28 represents "just intolerable" glare [Akashi 1996]. On the other hand, a rating of 0 is neutral in this glare evaluation. Thus, both rating scales were arbitrarily adjusted in such a way that a UGR of 19 can correspond to the neutral subjective glare rating of 0, and a UGR of 29 can match with the worst subjective glare rating of -2. The results of the subjective evaluations in Fig. 82 suggest that both UGR and subjective glare rating are reduced as the number of fixtures increases. However, the correlation between UGR and glare evaluation is low. Most subjects appear to not have strong feelings of glare from most conditions, while the UGR values indicate all lighting conditions are supposed to be glaring. This may be because subjects evaluate glare in a different way from summing up the glare of all light sources.

Observations of behavior while subjects evaluated glare from lighting installations with multiple light sources indicate that the typical subject looks at a light source for a time while rating the glare of a lighting installation. Thus, glare sensation is likely to correspond to glare caused by a single light source with the maximum degree of glare that probably has the highest luminance and/or the largest apparent size among the visible light sources in the visual field. Since luminance and apparent size of fixtures were similar to each other within these experimental conditions, glare from the central fixture represented the overall glare from the entire visual field. The UGR of the central fixture was compared with the subjective glare rating under each condition.

Figure 83(a) and (b) compare subjective glare ratings and UGR values under the five experimental conditions with different numbers of fixtures. In these UGR calculations, it was assumed that overall glare sensation would correspond to the degree of glare from the central light source. Figure 83 suggests that as the number of fixtures increases, glare sensation from those fixtures is reduced. The comparison of the two graphs suggests that UGR from the single central source correlates well to overall glare sensation. The point of intersection of each curve with the glare threshold line (0 for subjective evaluations or 19 for UGR calculations) suggests that to avoid glare, the number of fixtures should exceed 4-9 (6 on average; 4 was derived from the subjective evaluations and 9 was from the UGR calculations) for the source luminance of 4000 cd/m^2 used in this study.

[1] If the luminance of a light source exceeds the BCD luminance, the light source is supposed to cause glare to 50% of people.

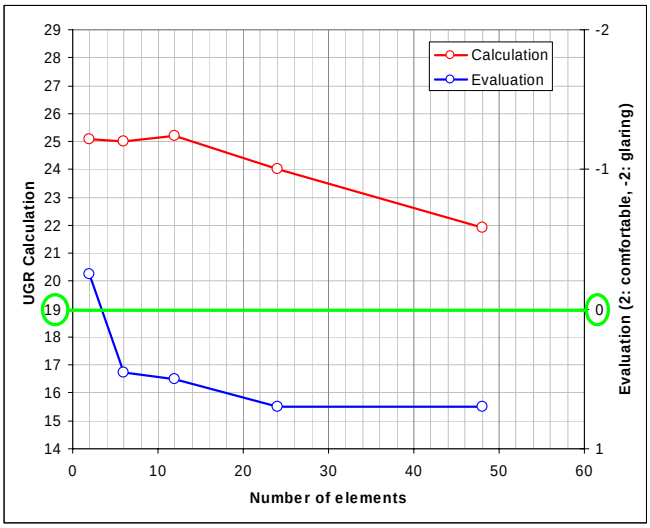
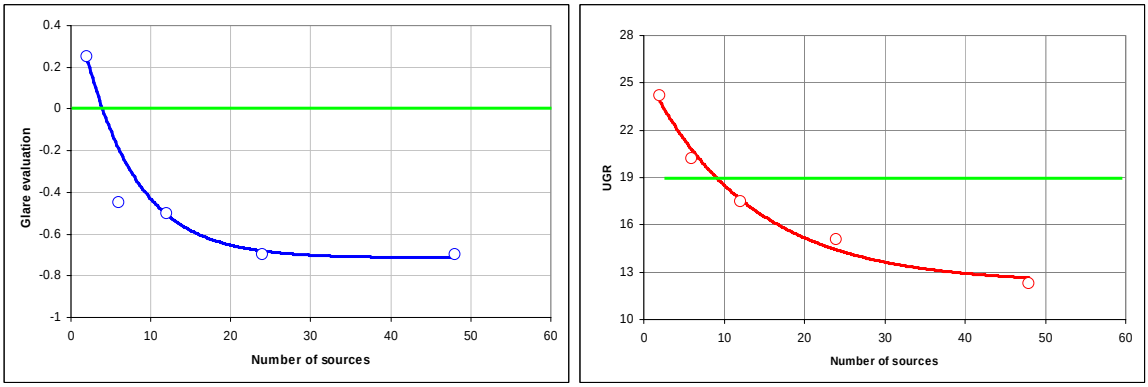


Fig. 82. Comparison of glare evaluations and UGR calculations.



(a) Subjective, overall glare evaluation (b) UGR calculation

Fig. 83. Comparison of UGR and subjective glare rating.

By extension, it is also possible to develop a design tool to help lighting designers select an appropriate size of light sources so that the light source does not cause glare to occupants. The following section introduces an example of such design tools.

Lighting design tool for glare reduction

Figures 84 and 85 show an example of lighting design tools developed for reducing glare. These diagrams will assist lighting designers in figuring out the limitation in apparent size of fixture, which provides glare on the borderline between comfort and discomfort.

The selection of the limitation in apparent size uses Figs. 84 and 85. Figure 84 shows UGRs as functions of the number of fixtures for different luminances of fixtures. By using the UGR of 19, or the glare threshold, it is possible for lighting designers to determine an appropriate number of fixtures to avoid glare. The green, straight lines in the diagram indicate that to prevent fixtures with luminances of 2000, 4000, and 8000 cd/m^2 from causing glare, the numbers of fixtures should not exceed 3, 8, and 21, respectively. Contrarily, fixtures with a luminance of 1000 cd/m^2 will not cause glare for any number of fixtures.

Figure 85 illustrates how to identify an appropriate aperture size for a fixture. Since the number of fixtures is synchronized with the fixture aperture size, once a number of fixtures is identified, it can be converted into an aperture size by using the bottom graph of Fig. 85. The example in Fig. 85 shows that the appropriate aperture size is approximately 0.001 sr. This size is equivalent to that of an 11 cm diameter downlight viewed at a distance of 6.5 m.

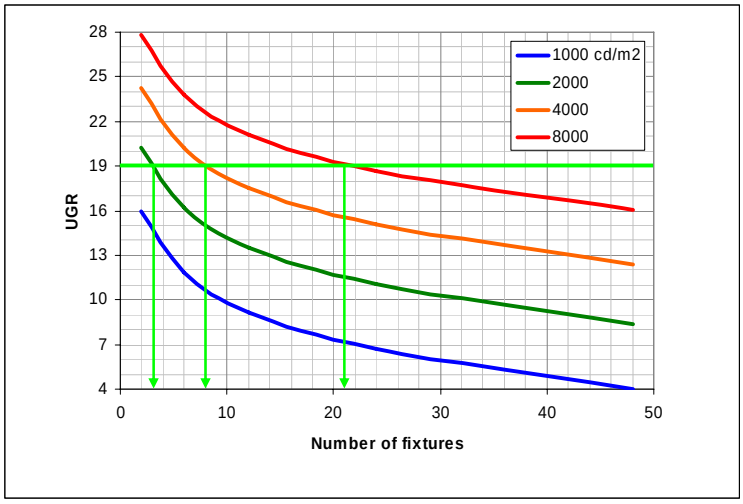


Fig. 84. Appropriate numbers of fixtures with different luminances.

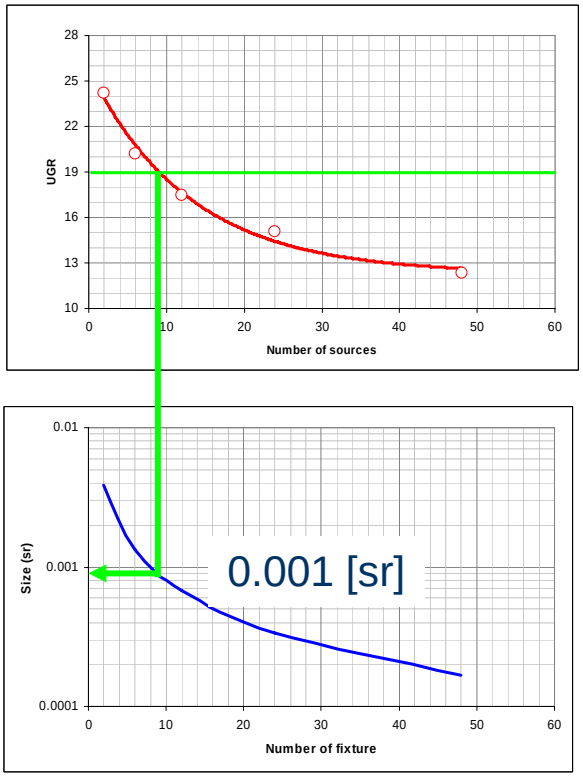


Fig. 85. Lighting design tool to avoid glare.

General conclusions

The results of the experiment suggested that within the range of lighting conditions employed in this experiment:

- The light pipe considered in this study was less appropriate compared to downlights. However, further investigation is needed to study how light pipe diameter affects preference.
- The lighting conditions with 6 to 15 luminous elements in the field of view were rated as the most appropriate for office applications.
  - As the size of luminous elements is reduced, while the number increases, glare sensation is reduced.
  - The lighting condition with 48 luminous elements was rated as the least glaring downlight condition.

Overall, the range between 6 and 15 in number of fixtures was the most appropriate for the office application. However, the number of luminous elements and the density (spacing) were synchronized in the experimental conditions. It is not clear which is a more important determinant of preference: the number of luminous elements or the density (spacing) of luminous elements. To address this question, another experiment was conducted using a scale model.

Scale model experiment

The use of the 1/12 scale model allowed for easy control of experimental conditions. By using the scale model, various layout patterns were prepared to explore the important determinants of the perception of space between the number and spacing of luminous elements.

Experimental setup

The 1/12 scale model was located in a laboratory at the Lighting Research Center. The scale model simulated an office room. Figure 86 shows a view of the experimental setup. The dimensions of the scale model were 16" (40.6 cm), 16" (40.6 cm), and 9" (22.9 cm) for the length, width, and height, respectively, corresponding to 16' (4.9 m), 16' (4.9 m), and 9' (2.8 m). The model room had three walls and the fourth side was left open for the subjects to view the different conditions. All wall surfaces were white with a reflectance of 80%, and the floor was painted gray with a reflectance of 35%. The interior of the model was furnished with miniature desks and chairs, and a miniature figure sat on one of the chairs. The miniature furniture and figure helped observers recognize the scale of the model and downlights in the ceiling. For several conditions presented in this experiment, the office model was scaled down to one-quarter of the size of the entire office by using an L-shape partition.

Above the scale model was a light box equipped with three fluorescent lamps (OSRAM SYLVANIA, OCTRON 32W T8, CRI=80). A correlated color temperature (CCT) of 6500 K was chosen because current, typical white LED lamps produce higher CCTs than those of conventional fluorescent lamps. The 4' T8 lamps were selected because their dimming capability allowed the illuminance of the room to be adjusted as needed. The box was internally painted white with a reflectance of 90%, so it acted as an "integrating sphere" and provided diffuse light. Below the lighting box and above the scale model was a ceiling plate made of cardboard with a thickness of 3 mm. The plate was painted white on both sides with a reflectance of 90%. The

ceiling plate had one or more openings, mimicking one or more downlight luminaires. On the top of the plate was a thin plastic diffuser. Light that came through the openings was diffused by the plastic diffuser to allow the "luminaires" to provide a nearly constant luminance in all directions.

Eight different opening patterns were prepared using the ceiling plates. By changing the ceiling plates, different "luminaire" layouts were presented to observers. For quick changes of the plates, four hinges joined the scale model and the light box. This allowed an experimenter to slide a ceiling plate in between the scale model and the light box.

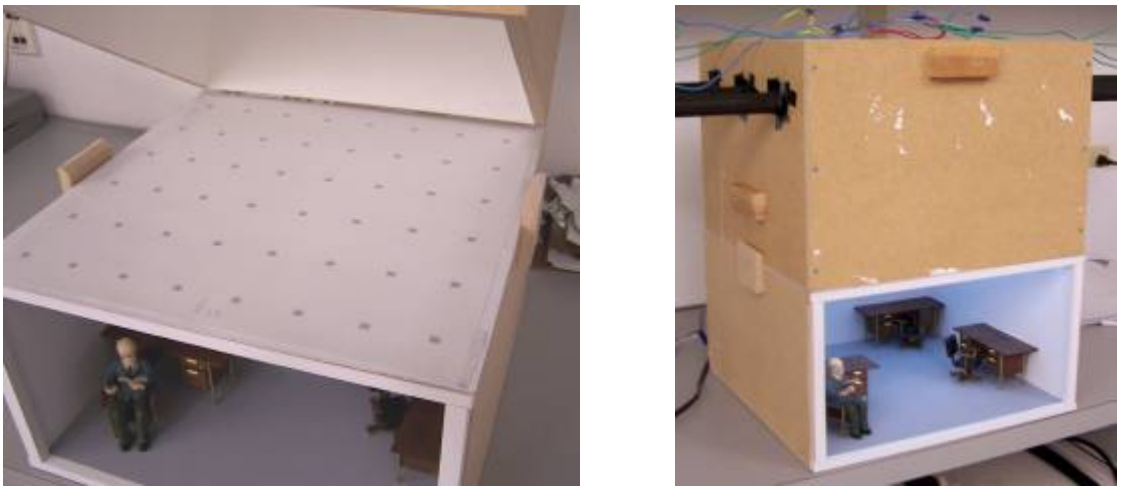


Fig. 86. View of scale model experimental setup.

Experimental conditions

The independent variables employed in this experiment were the size, number, and layout of the ceiling downlights, and the size of the room. The size and number of downlights were synchronized to keep the total luminous surface area constant across all downlight conditions, therefore maintaining a constant total luminous flux and horizontal average illuminance for each ceiling size. As the number of downlight luminaires increased, the size of each fixture decreased. Table 8 shows the eight experimental conditions. Appendix 5 shows layouts of the luminous elements used in the experiment and views of the large and small room conditions. Measured illuminance levels are also shown in Table 8. Each value is the mean of nine measurements. Illuminances under the sixth, seventh, and eighth conditions using the small, partitioned room were lower than the others. The difference in illuminance may affect the perception of brightness.

To quantify the density of luminous elements in the ceiling, spacing between luminous elements was used as a metric. When the lengthwise spacing was different from the widthwise spacing, the average of the two spacing values was used. For Conditions 1 and 6 with a single luminous element, the spacing was considered to be equal to the room width.

Conditions 1 and 6 with a single luminous element were used to avoid the effect of the range of experimental conditions on evaluations. This is because the range of experimental conditions often exaggerates differences in ratings among experimental conditions, even if the experimental conditions do not differ from each other. To avoid such so-called "range effects," a wider range of conditions is often chosen in experiments. Condition 7 with 12 luminous elements in the smaller room corresponds to Condition DL-12 in the mockup study. The illuminance level under Condition 7 was lower than that under Condition DL-12 though.

The average luminance of the light sources was adjusted to approximately 4000 cd/m^2 by means of a dimmer. This luminance corresponds to the median luminance in the mock-up experiment.

Table 8. Lighting conditions used in the experiment.

Condition	1	2	3	4	5	6	7	8
Room size (one side of square) (cm)	Large 40.6	Large 40.6	Large 40.6	Large 40.6	Large 40.6	Small 20.3	Small 20.3	Small 20.3
Number of Sources	1	12	12	48	48	1	12	12
Size of Sources (cm)	4.3*5.7	1.4*1.4	1.4*1.4	0.7*0.7	0.7*0.7	2.1*2.8	0.7*0.7	0.7*0.7
Total luminous area (*10^{-3} m^2)	2.43	2.43	2.43	2.43	2.43	0.61	0.61	0.61
Spacing in scale model (cm)	40.6	5.8	11.6	2.9	5.8	20.3	2.9	5.8
Spacing in real (m)	4.87	0.70	1.39	0.35	0.70	2.44	0.35	0.70
Illuminance (lx)	251	272	237	254	225	155	162	149

The ideas behind this plan were:

- *Determinant of preference*: The comparisons among Conditions 2, 4, and 7 allowed for investigation of the question of which is a more important determinant of lighting evaluations: the number of luminous elements or the density (spacing) of luminous elements. The spacing of luminous elements is constant under Conditions 4 and 7, while the element number of Condition 4 is four times larger than that of Condition 7. If there is a significant difference in preference ratings between Conditions 4 and 7, this would suggest that the luminous element number is more important for preference ratings than the spacing of luminous elements. The number of luminous elements is constant between Conditions 2 and 7, while the element spacing of Condition 2 is larger than that of Condition 7. Therefore, if there is a significant difference in ratings between Conditions 2 and 7, this would mean that the spacing of luminous elements is a more important determinant of preference. The comparisons among Conditions 3, 5, and 8 also examined the same question with different luminous element layouts.
- *Spacing*: The comparisons between Conditions 2 and 3, between Conditions 4 and 5, and between Conditions 7 and 8 investigated whether the spacing of luminous elements affects subjective evaluations for the same room size.
- *Number (or Size)*: The comparisons among Conditions 1, 2, and 4 and among Conditions 1, 3, and 5 investigated whether the number (or size) of luminous elements affects subjective evaluations for the same room size.

These ideas will be discussed later in the Discussion section.

Procedure

In the experiment, 18 subjects, ten males and eight females aged between 22 and 44 years, volunteered their participation to evaluated the eight ceiling downlight patterns. The order of the experimental conditions was randomized.

This evaluation used a questionnaire (Appendix 6). Each questionnaire sheet had two parts. The first part of the questionnaire was composed of five contrasting word pairs to describe the mood of the room. Each word pair had a seven-point scale, from -3 to +3, and subjects were requested to choose one of the seven points to evaluate the perception of the space. The second part of the questionnaire asked four questions about the appearance of downlights in the ceiling with regard to brightness, dimness, appropriateness of downlight number, and preference of luminous element layout. Each of the four questions used a five-point scale from -2 (disagree) to +2 (agree).

In this experiment, one subject participated at a time. Before the arrival of each subject, the experimenter set the first experimental condition in the scale model. Upon the subject's arrival, the experimenter gave the subject instructions, an informed consent form, and a set of questionnaire sheets. Then, the subject moved to the experimental setup with the questionnaire. Prior to the evaluations, the subject's eye height was adjusted to approximately 10 cm from the floor in the scale model, corresponding to 1.2 m. The viewing distance was set at 15 cm from the edge of the box, corresponding to 1.8 m. During the evaluations, the subject sat on a chair and was allowed to look around the scale model.

After the subject completed the questionnaire, the experimenter changed the experimental condition to the next one. During the change of the conditions, the subject looked away from the scale model. The subject was again asked to evaluate the lighting with the new condition. This procedure was repeated until all eight conditions were evaluated. The entire session took about 15 minutes for each subject.

Results

The evaluation data for each question and experimental condition were averaged. Table 9 and Figs. 87 and 88 show the results of the evaluations. The evaluations of the perception of the space and the appearance of the luminous elements used seven-point scales and five-point scales, respectively. To analyze whether there was a significant difference between each combination of the experimental conditions, t-tests were applied to all pairs of experimental conditions (Appendix 7). In the t-tests, a p-value less than 0.05 between a pair of conditions indicates a significant difference in evaluation between the pair.

Generally, Condition 1 (large room with a single luminous element) and Condition 6 (small room with a single luminous element) were the most negatively rated in most questions. The results of the t-tests also suggested this tendency. Condition 3 (large room with 12 luminous elements) was the most favorably evaluated in most questions. This tendency confirmed that of the mock-up experiment.

The following analyses focused on brightness perception ("dim / bright"), visual interest (boring / interesting), preference ("dislike / like"), glare ("too bright"), number ("too many / too few"), and layout preference ("dislike layout / like layout"), as the mock-up experiment did.

Table 9. Results of the evaluations.

	1	2	3	4	5	6	7	8
Perception of space								
Dim / Bright	-0.22	0.22	0.94	0.33	0.44	0.44	-0.22	-0.22
Non Uniform / Uniform	-1.44	-0.33	1.67	0.28	2.06	0.22	1.00	1.67
Boring / Interesting	-1.22	-0.17	0.94	0.56	1.44	-1.22	0.33	1.00
Unpleasant / Pleasant	-0.72	0.00	0.94	0.33	0.89	-0.50	0.56	0.89
Dislike / Like	-1.33	-0.22	1.00	0.11	0.83	-0.72	0.39	0.89
Luminous element appearance								
Too Bright	0.33	-0.06	-0.06	-0.61	-0.33	0.17	-0.78	-0.83
Too Dim	-0.72	-0.39	-0.94	-0.44	-0.67	-0.83	-0.06	-0.67
Number of Sources	1.50	0.50	-0.17	-0.56	-0.78	0.94	-0.06	-0.44
Like Layout	-1.06	-0.33	0.83	-0.06	0.44	-0.72	0.44	0.67

Dim / Bright

Condition 3, 12 luminous elements with a larger spacing in the large room, gained the highest rating among the eight conditions. This finding is confirmed by the results of t-tests, suggesting the perception of brightness under Condition 3 was rated higher than brightness perception under Conditions 1, 2, 7, and 8.

Condition 1, a single luminous element in a large room, and Conditions 7 and 8 (both 12 luminous elements in a small room) were evaluated as appearing dimmer than the other conditions, although the result of the t-test did not show any significant differences. The lower brightness perception under Conditions 7 and 8 probably reflects the lower illuminances in those conditions.

Non-uniform / Uniform

Subjects perceived more uniformity with larger luminous element spacing for a fixed room size and a fixed luminous element number. The results of t-tests between conditions 2 and 3, between Conditions 4 and 5, and between Conditions 7 and 8 supported this tendency.

Boring / Interesting

Overall, as the number of luminous elements increases, the room appears more interesting. This tendency was supported by the result of the t-test comparing Conditions 2 and 4, while another t-test comparing Conditions 3 and 5 showed a p-value (0.083) close to being significant. Rooms with a single luminous element obviously bored observers.

A new finding from this experiment compared to the mock-up is that with the same number of luminous elements, the wider the luminous element spacing, the more interesting the room appears. This was supported by the results of t-tests comparing Conditions 2 and 3 and Conditions 7 and 8. However, the t-test between Conditions 4 and 5 failed to prove a significant difference while providing a p-value (0.06) that was close to the significance criterion (0.05).

Unpleasant / Pleasant

Subjects expressed unpleasantness with a single luminous element, namely Conditions 1 and 6. Comparisons between Conditions 2 and 3, between Conditions 4 and 5, and between Conditions 7 and 8 suggested a tendency that the larger the spacing of luminous elements, the

more pleasant the room appears, although the t-tests did not support this tendency. The details of the perception of pleasantness will be discussed later.

Dislike / Like

Subjects disliked conditions with a single luminous element, namely Conditions 1 and 6. Contrarily, Condition 3 with 12 luminous elements gained the higher score. This tendency may support the finding of the mock-up experiment. The effects of the spacing on preference will be discussed later.

Glare—"Too bright" evaluation

There is the same overall tendency here as in the mockup experiment that as the number of luminous elements increased (*i.e.*, the size of each element decreased), the luminous elements became more comfortable (not "too bright"). The result of the paired t-test between Conditions 2 and 4 also supports this tendency. This tendency is also consistent with the glare calculations. The spacing of luminous elements did not affect the glare evaluations, as the results of the t-tests between Conditions 2 and 3 and between Conditions 4 and 5 indicate. Interestingly, the comparisons between Conditions 4 and 7 and between Conditions 5 and 8 showed that an increase in the number of luminous elements increases the sensation of glare very little.

Appropriateness of luminous element number

As the number of luminous elements increases, the room starts appearing to hold too many luminous elements. Conditions 3 and 7, with 12 luminous elements, were rated to hold the most appropriate number of luminous elements. This is consistent with the results of the mock-up experiment. This may lead to an interesting recommendation that 12 luminous elements may be the most appropriate to illuminate a room, regardless of the room size. Of course, this tendency should be verified by further research using larger rooms. The density (spacing) also seems to affect the appropriateness evaluations. A more compact layout with a higher density (shorter spacing) may make the room appear to hold a smaller number of luminous elements. Those results will be discussed later.

Preference of luminous element layout

The general tendency for layout preference is consistent with that of the "dislike / like" evaluation in the first experiment. Again, subjects disliked conditions with a single luminous element such as Conditions 1 and 6. Contrarily, Condition 3 with 12 luminous elements gained the highest score. This suggests the validity of the magic number "12" as the downlight number appropriate for an interior space. These tendencies will be discussed later.

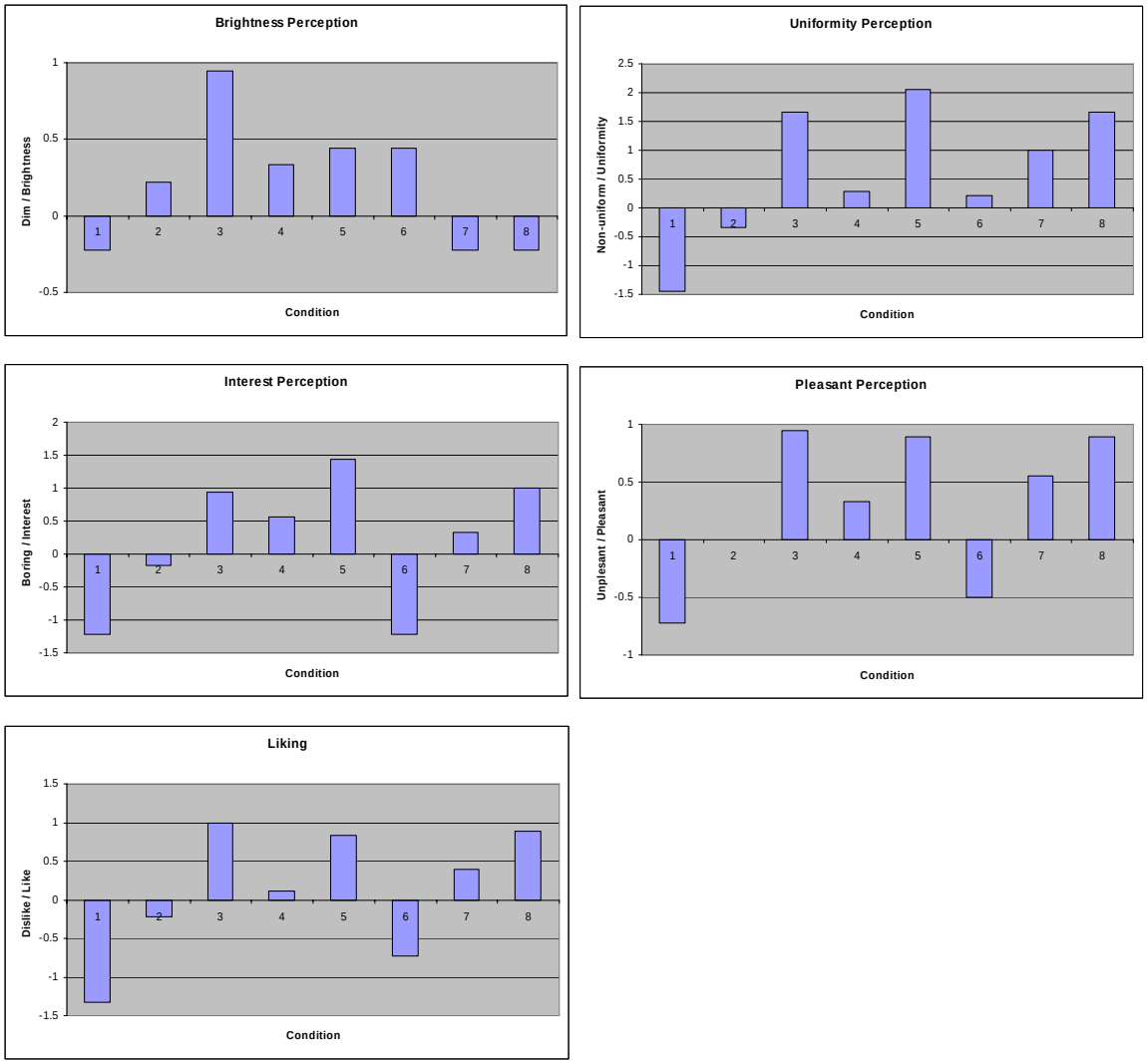


Fig. 87. Results of evaluation—perception of space.

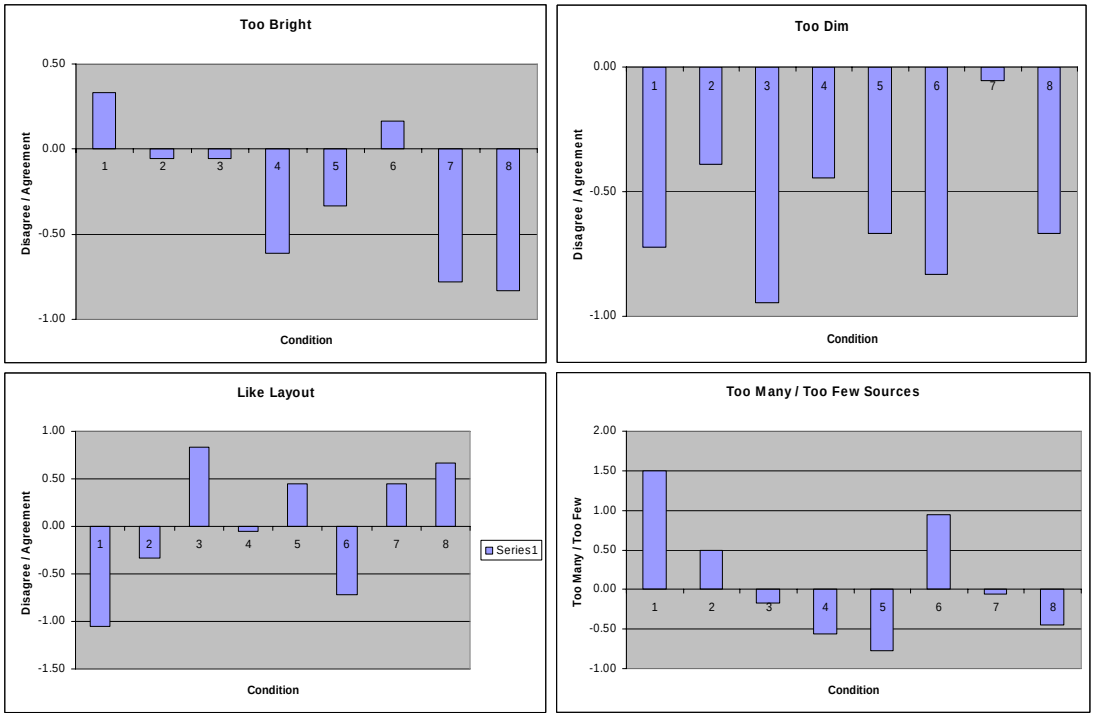


Fig. 88. Results of evaluations—appearance of ceiling.

Discussion

Determinants of lighting quality

In this section, the above described ideas behind the experimental design are discussed.

(1) Determinant of lighting evaluation: The comparisons among Conditions 2, 4, and 7 were conducted to address the question of which is a more important determinant of lighting evaluations: the number of luminous elements or the density (spacing) of luminous elements. The comparisons focused on preference evaluations including the pleasantness ("unpleasant / pleasant"), liking ("dislike / like"), and layout preference. The results of the t-tests suggested significant differences only between Conditions 2 and 7 for the pleasantness and layout preference evaluations. This implies that since the number of luminous elements is constant but the spacing is different between Conditions 2 and 7, the spacing of luminous elements is more important for preference evaluations than the number of elements. Contrarily, no significant difference between Conditions 4 and 7 with the same spacing was found. Since the spacing of luminous elements is constant but the number of elements is different between Conditions 4 and 7, the results again rejected the importance of the number effect on preference. There is still a possibility that the spacing could influence preference.

For the same reason, the comparisons among Conditions 3, 4, and 8 were conducted. However, there were no significant differences in the pleasantness, liking, and layout preference evaluations among those conditions. This implies that both the spacing and number could be determinants of preference.

Unfortunately, from these comparisons, it was difficult to identify which is more important between the spacing and number of luminous elements.

(2) Spacing: The comparisons between Conditions 2 and 3, between Conditions 4 and 5, and between Conditions 7 and 8 were conducted to investigate whether the spacing of luminous elements affects preference of lighting and space for the same room size. These comparisons also used the results of the pleasantness, liking, and layout preference evaluations. The results of the t-tests suggested that there were significant differences between Conditions 2 and 3 for the pleasantness, liking, and layout preference. However, the other combinations, Conditions 4 and 5, and Conditions 7 and 8, did not show any significance in the preference evaluations. Due to the inconsistency among the results of the t-tests, it was difficult to determine for certain that people like large spacing between luminous elements. However, in all three combinations, there was a common tendency that the preference became higher as the spacing of luminous elements increased.

To identify whether the spacing of luminous elements affects glare sensation and appropriateness of luminous element number for the same number and size of luminous elements, the comparisons between Conditions 2 and 3, and between Conditions 4 and 5 were done based on the results of the t-tests. The results suggest there is no significant difference for both pairs. This implies that the spacing does not affect glare sensation or appropriateness of luminaire number.

(3) Number (or size): The comparisons among Conditions 1, 2, and 4 and among Conditions 1, 3, and 5 were conducted to investigate whether the number (or size) of luminous elements affects subjective evaluations for the same room size and same spacing. Tendencies in t-test results were consistent among all three preference evaluations (pleasantness, liking, and layout preference). They all showed that Condition 1 was rated as the worst lighting condition—there were significant differences in evaluations only between Condition 1 and the other conditions.

With regard to the appropriateness of the number of luminous elements, the results of the t-tests suggested significant differences among all combinations of experimental conditions. Since Conditions 2 and 3 were rated as the most neutral conditions (meaning not "too many" or not "too few"), or the most appropriate conditions in luminous element number, it can be concluded that the number "12" is the most appropriate for luminous elements in a room. These results confirmed those of the mock-up experiment.

Only a few studies have addressed the question of what is an appropriate number of luminous elements in a room. One study conducted an experiment using a 1/12 scale model to optimize the number of sparkling luminous elements [Mukai 1997]. The results of the study suggested that more than 20% of people may start complaining of too many sparkling luminous elements when the density of the luminous elements in the ceiling exceeds 20 units / steradian (sr)[2]. If the criterion used by Mukai *et al.* is applied to our study, the element number of 12 for our experimental setup corresponds to approximately 22 units / sr. This means that the results of our study are consistent with the findings in Mukai *et al.*'s study.

Development of model

Based on the above discussion, to generalize the accomplishments of this experiment to the lighting applications, a model was finally considered for the preference of luminous element

[2] Steradian (sr) is the unit of solid angle. The solid angle of a luminous element can approximately be calculated by dividing the projected area of the luminous element by the square of the viewing distance.

layout. The results of the experiment suggested that the size, spacing, and number of luminous elements affected the preference of the luminous element layout. However, the number of luminous elements was synchronized with the size of the luminous elements (to obtain the same light output from the different combinations of number and size). Since the results of the experiment did not show a simple linear relationship between each determinant and the layout preference, a nonlinear regression analysis was applied to this modeling. Table 10 shows the data used for this modeling. Since the distances to the center of the ceiling from an observer, and therefore the apparent sizes and spacing of luminous elements, are different between the smaller and larger rooms, the sizes and spacing were relatively expressed by subtended angles (in degrees). The results of the nonlinear regression led to Equation (5),

$$P = 16.1 \times (A_{spacing} / A_{size})^{0.67} + 1.33 \times e^{\frac{-(N-12)^2}{2\times 3^2}} \qquad (5)$$

where P is the percentage of occupants who like the luminous element layout, and $A_{spacing}$, A_{size}, and N are the angular spacing of luminous elements, the angular size of luminous elements, and the number of luminous elements.

The R squared value was 0.91 with this function. The first term represents the effect of the density of downlight luminous elements in the ceiling on layout preference, and the second term describes the effect of the number of luminous elements. The structure of the second term was introduced from the preliminary analysis based on the mock-up experiment. Comparisons in coefficients between the first and second terms suggest that the contribution of the number of luminous elements is much smaller than that of the density of luminous elements. The balance of coefficients between the first and second terms is subject to change depending on the experimental conditions and the contexts of the applications.

Consequently, Equation (5) suggests the importance of the two determinants, the number and density of luminous elements, to predict the preference of downlight layout. The tendency is that as the density becomes lower, the downlight layout becomes more preferred. The medium number of luminous elements around 6 to 15 is appropriate for LED downlight applications. However, before implementing these equations to actual lighting applications, it is still important to conduct experiments using a wider range of experimental conditions.

Table 10. Parameters used to model the layout preference.

	1	**2**	**3**	**4**	**5**	**6**	**7**	**8**
Angular size (deg)	7.54	2.13	2.13	1.07	1.07	4.91	1.42	1.42
Angular spacing (deg)	7.54	8.83	17.67	4.42	8.83	4.91	5.87	11.74
Number of elements	1	12	12	48	48	1	12	12
Agreement of layout (%)	11	33	72	44	67	17	56	61

General conclusions

The above findings of the scale model experiment suggest that within the range of lighting conditions employed in this experiment:

- As the spacing of fixtures increases, the room tends to appear preferred.

- The scale model study confirmed the results of the full-scale mockup study and glare calculation.
    - As the size of fixtures decreases, glare sensation is reduced.
    - In the context of the experiment, a fixture number of 12 seems to be the most appropriate.

However, it is still not yet clear which is a more important determinant of lighting evaluations: the number of luminous elements or the spacing of luminous elements.

Conclusions and potential recommendations for LED downlights

The above-described experiments and calculations led to the following conclusions:

- The downlight application was more appropriate than the light pipe—further investigation is needed to study how light pipe diameter affects preference.

- The range of fixture number between 6 and 15 seems to be the most appropriate in an office lighting context, in terms of brightness, liking, visual interest, and glare.

- As the aperture size decreased while the number of downlight luminous elements increased, the light sources became less glaring for the same luminance. Glare calculations supported the minimum aperture number of 6, equivalent to the maximum downlight diameter of 11 cm.

- Larger luminaire spacing, which provides a more uniform illuminance distribution, may be preferred with an appropriate number of downlights.

Based on the above-described conclusions, the following steps are probably acceptable for developing LED downlights and designing interior lighting with LED downlights:

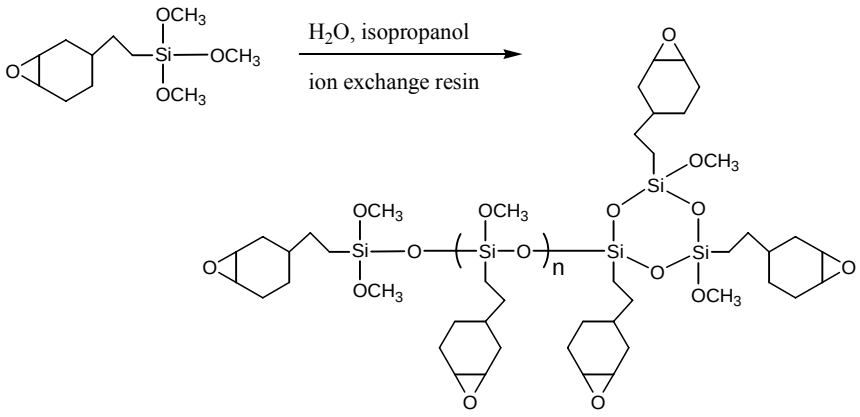
(1) Develop a downlight with a small diameter, less than 11 cm and ideally less than 8 cm, as long as the cost permits. However, the luminance shall not exceed 4,000 cd/m^2 at critical glare angles (>45 degrees) from the nadir. These criteria will make the best use of the features of small light sources and minimize glare. These requirements may be achieved with current white LED technology.
(2) Identify an appropriate downlight spacing to obtain appropriate illuminance on the working plane with the LED downlights.
(3) Determine a cutoff angle for the downlight so that only 6-15 luminous elements are visible (or conspicuous) to occupants when the LED downlights are laid out in a large space. Spread the LED downlights at the largest possible spacing over the ceiling.
(4) Design a luminous intensity distribution for the LED downlight to provide the determined glare cutoff.
(5) To optimize the luminous intensity distribution, several iterations from Steps (2) to (4) may be required.

However, further demonstration studies will be needed before implementing these recommendations. Additionally, these recommendations are subject to change when high-power, high-luminance LED lamps are developed.

R.10 Development of LED Encapsulants

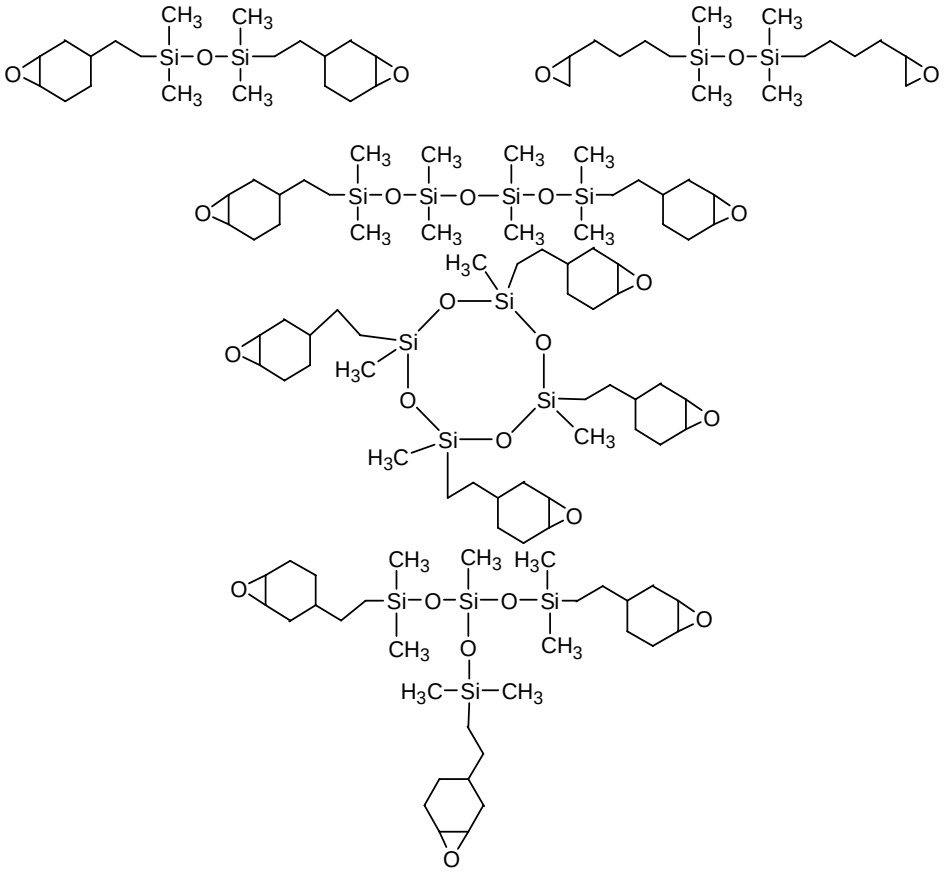
Initial Testing and Screening

Recently, a new class of multifunctional epoxy resins that incorporate silicon in their structures has been developed in our laboratories at Rensselaer [Crivello 1997a], [Crivello 1997b]. These materials are prepared by a novel reaction involving the controlled reaction of water with an epoxy functional trialkoxysilane. The general reaction is depicted below. Manipulation of the reaction conditions and the amount of water result in the generation of multifunctional epoxy resins bearing linear and cyclic siloxane backbone structures.

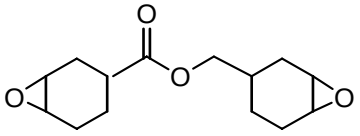


Resins with up to 12 pendant epoxy groups and molecular weights from 1,000 up to 7,000 g/mol have been prepared and characterized. The above chemistry has been demonstrated on a pilot scale and is currently being commercially scaled-up in 50 gallon reactors to provide these materials in kilogram quantities. Considerable variation in the structure of the resins is possible to generate a wide range of materials with differing mechanical and thermal characteristics. A number of additional applications such as optical adhesives, protective coatings, electrical laminates, interlayer dielectric materials, and holographic storage media are being pursued with these novel materials. It initially appeared that this novel class of epoxy-silicone materials was ideally suited for the previously outlined demanding LED applications. First, the resins are essentially transparent in both the visible and UV region of the spectrum. They are completely colorless, transparent viscous liquids. Since they contain no chromophors that absorb in these regions, they do not degrade either under the constant emission of a UV-emitting LED or on weathering. These resins are extraordinarily insensitive to oxidative attack either by ozone or by highly energetic atomic oxygen. This was demonstrated by exposure of the resins to oxygen plasma in a barrel etcher, and also by direct exposure of the resins to atomic oxygen in low earth orbit [Connell 1995]. Long-term exposure to the hard UV irradiation of space also produced no discoloration of the resins. Lastly, the resins contain very low levels of ionic impurities that can either result in corrosion or degradation of the semiconductor device itself or to interconnects. Finally, the above resins can be cured using methods that are compatible with current industry practice.

However, when the above resins were subjected to long-term oxidative exposure at 140°C, yellowing took place within two weeks. Accordingly, other silicone-epoxy resins prepared in this laboratory were evaluated using the same screening technique. The structures of these epoxy resins are depicted below.



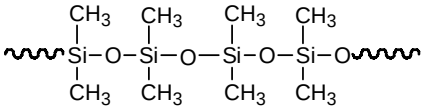
In all cases, observable yellowing occurred within two weeks at 140°C. Similarly, the commercial non-silicone resin, having the structure shown below, was evaluated. This resin also displayed pronounced yellowing characteristics before and after curing.



Analysis of the results suggested that in all cases, the epoxy group and related structures were responsible for the oxidative instability during aging and that consequently, no epoxy-based encapsulant would have sufficient stability for application in high-intensity LEDs.

Accordingly, a general screening program was initiated to evaluate resins that could potentially serve as LED encapsulants. Poly(methyl methacrylate) (Plexiglas) is used as a glass replacement in many applications because of its excellent light stability. Other acrylate and methacrylate polymers, including poly(butylmethacrylate), poly(isobutylmethacrylate), poly(ethyl-methacrylate), poly(butylmethacrylate-co-methyl methacylate) and poly(vinylbutyral),

were screened. All the polymers cited above underwent significant yellowing under the aforementioned conditions. An even more general screening protocol was conducted to evaluate well-known organic resins such as polycarbonate) and a variety of polyesters. Again, early failure due to pronounced yellowing was observed in all cases. It appears that there is no known simple, organic resin that could be considered a candidate encapsulant resin for LED encapsulants. Accordingly, the effort turned towards the silicone-epoxy resins initially screened in this study. It was reasoned that if the epoxy portion of the molecule were eliminated, it might be possible to achieve a reasonable level of thermal oxidative stability. Thus, several polydimethylsiloxane (silicone) resins were evaluated in the screening tests. The results were dramatic. Even after 4 weeks at 140°C in air, there was no observable yellowing.

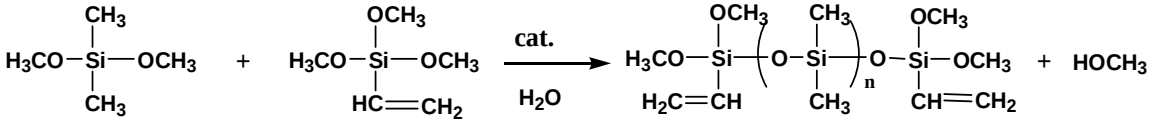


Polydimethylsiloxanes with the structure shown above appear to have excellent inherent oxidative stability. This is well-known in the literature and is due to the presence of only strong bonds in the molecular structure. However, on long-term exposure to heat, even these resins do undergo slow, degradative bond cleavage reactions. Apparently, the key to the ability of these resins to survive the screening test is due to the fact that despite this degradation, the products that are produced are not colored. Thus, a structure which incorporates primarily Si-C, Si-O and primary C-H bonds is required.

Silicone-based LED encapsulants

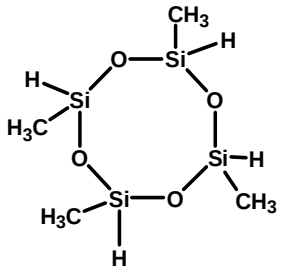
Having identified silicone resins as potential candidate materials for high-intensity LED encapsulants, it was necessary to address several other practical issues. Silicones are typically liquids at room temperature. When crosslinked (or cured), these polymers yield soft elastomers. However, LED applications require a hard, glassy-type of encapsulant. Therefore, neither type of conventional silicone material is suitable for an encapsulant. Therefore, the first task was to consider how to design a thermosetting silicone resin with the type of mechanical properties that were required. Equally important was the need to incorporate into that design a thermosetting reaction that meets the processing requirements that were previously discussed.

After several attempts, we focused on the chemistry shown in the following reaction sequence.

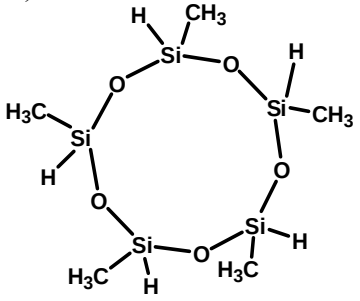


A short chain, multifunctional vinyl siloxane oligomer was prepared by the hydrolytic co-condensation of dimethyldimethoxysilane and vinyltrimethoxysilane. These readily available commercial compounds can be condensed using various ratios of the two starting materials to give a range of colorless, liquid resin precursors. By controlling this ratio, one can adjust the hardness and viscosity of the resulting resin. The best results were obtained using a resin prepared with a two-to-one ratio of vinyltrimethoxysilane and dimethyldimethoxysilane. The final encapsulation resin is produced by combining the above vinyl functionalized resin with

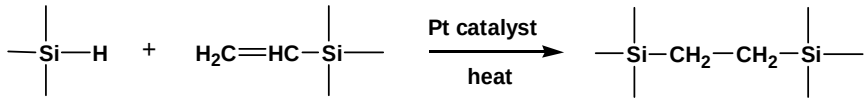
another silicone oligomer (a hardener) containing silicon-hydrogen (Si-H) groups. Cure is achieved by heating the above two-part system in the presence of a catalytic amount of a platinum complex. Only a few parts per million of the platinum catalyst is required. Cure takes place readily starting at approximately 50°C. In all cases, the two components of the resin must be over-designed with respect to the number of functional groups to achieve a rapid cure. Over the course of the past year, the structure of the Si-H containing oligomer has changed substantially. Initial work was carried out using a polydimethylsiloxane containing Si-H terminal groups. However, this gave cured resins with very poor mechanical properties. More recently, two alternative Si-H containing substrates have been used. First, the cyclic compound, 1,3,5.7-tetramethylcyclotetrasiloxane (D^H_4) was used.



It was quickly observed that volatilization of this resin component took place during curing, producing bubbles and also giving poorly reproducible results due to loss of stoichiometry. For that reason, this cyclic siloxane was replaced with the next higher homolog (1,3,5,7,9-pentamethylcyclopentasiloxane, D^H_5) with the structure shown below.



Both of these cyclic siloxane compounds are available in quantity from the Peninsular Chemical Company. Overall, the cure reaction involves the hydrosilation (*i.e.*, the addition of a Si-H group) across the carbon-carbon double bond of the vinyl group, as depicted in the equation shown below.



This reaction is ideal for encapsulant purposes for several reasons. First, the reaction proceeds without the formation of any by-products. Second, the rate of the reaction can be adjusted by several means (*e.g.*, catalyst structure and concentration) such that it can be carried out in a few hours at moderate temperatures. None of the resin components are corrosive to the electronic components of the LED. Lastly, the two-carbon crosslinking bridge that is formed is quite thermal-oxidatively stable and even if it is cleaved, the products are not colored. We have also

used the platinum-based Karstedt's catalyst, which is a stable, commercially available complex of platinum with a divinyl siloxane.

To test the viability of this approach to LED encapsulants, a casting block was used consisting of wells approximately 2 mm in diameter and 8 mm deep. The mixed resin together with the platinum catalyst was poured into the wells and a copper wire was added to simulate a LED device and its leads. This assembly was then placed in a forced-air oven for cure.

A variety of cure profiles were examined to optimize the cure conditions. As in the traditional epoxy encapsulants, a temperature ramping scheme was found to give the best results. We found that pregelling the resin at 90°C for one hour followed by raising the temperature to 120°C resulted in a hard, clear cylinder of the encapsulant. Pretreatment of the mold with a Teflon mold release was used to assist removal of the encapsulated prototype from the mold. The initial success described to this point was very encouraging, and we then moved on to the next step in the evaluation: the encapsulation of live devices. To this end, high-intensity LEDs without encapsulants were obtained from Opto Technology, Inc. These devices consist of an array of LED devices on a ceramic chip carrier that is mounted in a metal (brass) cup.

Immediately, difficulties arose. Since the chip carrier was mounted in such a manner as to be slightly above the metal base, it proved to be difficult to flow the resin under the chip carrier and to completely eliminate the air which became trapped under the flat chip carrier. Removal of the air bubbles during cure was a major problem. In addition, a serious cracking problem was encountered during and after cure, resulting from shrinkage and strain in the rather large encapsulant. In many cases, there was debonding from the sides of the metal package, indicative also of a mismatch in the coefficients of thermal expansion during cure. To overcome these problems, it was necessary to both change the encapsulant formulation and the overall processing conditions. To minimize shrinkage and to modify the thermal expansion characteristics of the resin, it was necessary to add filler to the encapsulation resin. We attempted to add as much filler to the resin as possible without also seriously compromising the viscosity and flow characteristics. Silica particles (50% by weight) were found to give nearly transparent cured resins with good index matching and reduced shrinkage. Again, the removal of bubbles proved to be a major source of difficulties. This was eventually, satisfactorily solved by conducting an initial degassing of the resin in a vacuum oven after adding the filler to the vinyl functional silicone resin. An additional degassing step was also incorporated after the Si-H resin was added and the encapsulant was poured onto the cup of the LED device and the curing step was carried out in a vacuum oven. Using this procedure, very slightly translucent encapsulated LEDs were obtained that were placed on test. At this point, life-testing was inconclusive due to electrical failure of the LEDs. Encapsulant materials were also supplied to the University of California Santa Barbara for testing. However, we have not received information on their status.

Future Work

We are confident that the chemical approach to the design of encapsulants using thermoset silicone resins for high-intensity LEDs is correct. Additional fine tuning may be necessary to adjust the processing parameters and to further refine the properties. The materials that have been used to design the present encapsulants are readily available and commercially attractive,

and the chemical process for preparing the vinyl functional resin is straightforward and easily carried out.

Approximately six months ago, we were contacted by the Rohm and Haas Company about the possibility of acquisition of this encapsulant technology. As of April 1, 2005, an agreement has been concluded between Rohm and Haas and Rensselaer to license the current silicone resin and any future technological developments in this area. Further, Rohm and Haas will sponsor additional work in this laboratory to continue the research effort. Efforts will be made to introduce further modifications of the encapsulant. For example, the refractive index will be adjusted by incorporation of small amounts of germanium or titanium-containing groups.

Experimental Procedures

We have incorporated into this report the optimized experimental procedures that were developed for the synthesis of the vinyl functional silicone resin and for the encapsulation of LEDs. This should provide detailed information that would enable others to reproduce our work.

Synthesis of Vinyl-functional Siloxane Resin

Vinyltrimethoxysilane (20.7 g, 0.14 mol) and dimethyldimethoxysilane (33.6 g, 0.28 mol) were placed in a 250 mL round bottom flask. Water (17.6 mL) was added and the solution was brought to reflux for 24 hours at 60°C. The mixture was cooled to room temperature, and two layers were formed. The biphasic mixture was transferred to a separatory funnel. The lower layer was transferred to a 100 mL round bottom flask and dried under vacuum using a rotary evaporator for 3 hours. The flask was removed and attached to an oil pump to remove any residual volatile impurities for 24 hours. A clear colorless liquid (26 g) was obtained (96% conversion).

To ensure reproducibility and to make certain that sufficient materials were available for more detailed encapsulation studies, the above synthesis was rerun three separate times. Identical results were obtained in each case, yielding approximately 70 g of encapsulant for future work.

Encapsulation and Cure

The polymerization was carried out as follows: Combined were 0.5 g of the vinyl-functional oligomer, 0.3 μL of Karstedt's catalyst, and 0.35 g of UVT Sunspheres (silica, size: 5 μm). This mixture was heated in an oven for 45 minutes at 90°C to degas the solution and to decrease the viscosity. While hot, 0.2 g of 1,3,5,7,9-pentamethylcyclopentasiloxane (D_5^H) was added and the mixture was gently swirled to avoid entrainment of air. The mixture was poured onto a LED array and the device placed in a forced-air oven at 90°C for 18 hours. The temperature was slowly ramped down to room temperature over the course of 3 hours. The encapsulated LED was translucent, hard, and crosslinked.

R.11 Benchmarking Current, State-of-the-art LED Devices

Continuation of previous benchmarking study

This benchmarking study evaluated five types of high-flux LEDs: single-die red, green, blue, and white, and multi-die white LED arrays. LED arrays were mounted in specially designed life-

test chambers and operated for 10,000 hours at combinations of two drive currents (350 mA and 450 mA) and two ambient temperatures (35 ºC and 50 ºC). The results show that:

1. Green and single-die white LEDs degraded slowly, even under increased drive current and ambient temperature.
2. Blue and multi-die white LEDs showed the highest rates of degradation.
3. Data extrapolation indicates that the single-die white LED will maintain 70% of its initial light output at 45,000 hours.
4. The individual white LEDs on each array exhibited large color variations from the beginning. However, their individual color shift over time was within a 4-step MacAdam ellipse.

Figure 89 shows the relative light output as a function of time for the LED arrays.

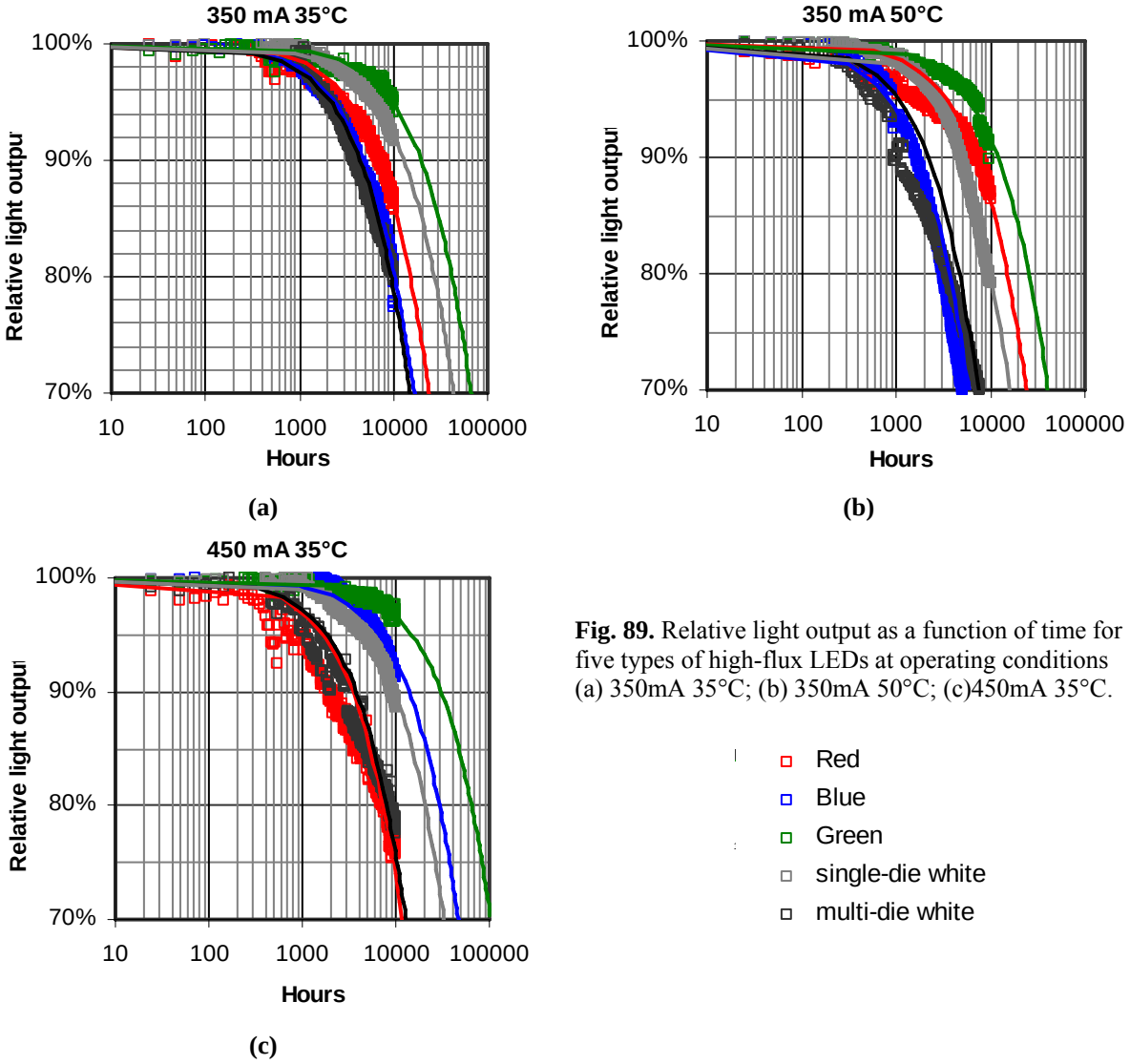


Fig. 89. Relative light output as a function of time for five types of high-flux LEDs at operating conditions (a) 350mA 35°C; (b) 350mA 50°C; (c)450mA 35°C.

New benchmarking study for high-flux LEDs

As white LEDs have rapidly evolved for use in general illumination applications, many high-flux white LEDs have entered the marketplace. The goal of the second benchmarking study was to report on how the different commercial high-power white LEDs perform when they operate under similar conditions. The experimental method for this study was very similar to the previous study. Altogether, 14 arrays of white LED packages were life-tested; four arrays consisted of multi-die packages and the remaining were single-die packages. All the LEDs were operated at their rated current (350 mA or 420 mA) and at ambient temperatures of 35°C and 50°C. The operating conditions of the arrays and the measured cathode-pin temperatures are summarized in Table 11.

Figure 90 shows the relative light output as a function of time for the LED arrays. As seen in Fig. 90(a), the variation of life among the different commercial white LEDs is very large at the 35°C ambient temperature condition, 500 hours to almost 45,000 hours. For two of the devices, C and G, it is too early to make a reasonable prediction of their expected life. The life differences at 50°C ambient temperature are similar to those at the lower temperature (shown in Fig. 90(b)). However, device F is exhibiting a much longer life at the higher ambient temperature than at the lower ambient temperature. To identify possible reasons for this unexpected occurrence, the cathode-pin temperature data over the period of the life test were carefully analyzed. However, nothing looked abnormal, and the average value was maintained throughout. One possible explanation for the longer life at the elevated ambient temperature could be that the performance variation between similar LEDs is large, due to manufacturing issues. It is not possible to verify this explanation in this life study because the sample size is too small.

Table 11. Testing conditions for high-flux white LEDs.

	Drive Current (mA)	T_{pin} @ 35°C ambient temperature (°C)	T_{pin} @ 50°C ambient temperature (°C)
A	350	52	58
B	350	38	49
C	350	40	48
D	350	38	50
E	350	44	58
F	420	59	68
G	350	64	77

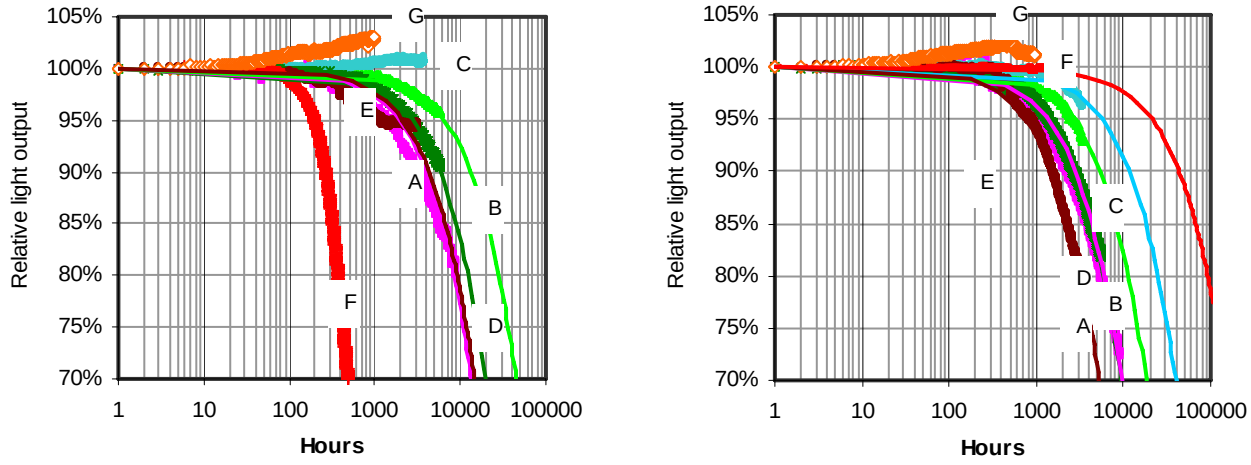


Fig. 90. Relative light output as a function of time for high-flux white LEDs at (a) 35°C and (b) 50°C ambient temperature operating conditions.

Life prediction study for phosphor-converted white LEDs

Presently, LED manufacturers are designing more efficient and reliable white LEDs than ever before. However, there is no easy way to predict the life of white LEDs under conditions different than nominal. Therefore, the goal of this part of the study was to investigate how different types of commercial white LEDs degrade over time and to compare the effects of drive current and ambient temperature on the degradation rate. In the long run, this information will be useful in developing a life predictor that can reduce the need for time-consuming life tests.

Typically, LED performance is affected by the drive current and by the ambient temperature surrounding the LED. Both of these parameters contribute to the junction temperature of the LED, which is known to be a good predictor of LED life. Therefore, our objective was to determine whether drive current and ambient heat have similar effects on the degradation of white LEDs. To understand how the different LED packages are affected by these parameters, LED arrays were tested at different operating conditions using either the same current but different ambient temperatures, or the same ambient temperature but different currents.

Experiment

Two life tests were conducted to compare the effects of drive current and ambient temperature on white LED degradation. The first experiment investigated 5-mm white LEDs arrays, and the second experiment studied high-flux LED arrays.

Before beginning the experiments, the LEDs were operated in their individual chambers for 1,000 hours for seasoning. Prior experiments in the laboratory have shown the need for seasoning because of the rapid changes that LEDs experience initially (probably due to annealing factors) before they settle into a steady decline over time.

Experiment 1

The goal of the first experiment was to determine the effects of ambient temperature and drive current on the degradation rate of 5-mm white LEDs. Two groups of white LEDs were life-tested. The LEDs in Group 1 were operated at similar currents but at different ambient temperatures, and the LEDs in Group 2 were tested at similar ambient temperatures but at different currents. Thirty 5-mm white LEDs were selected from the same batch, acquired in April 2003. Six LEDs with the same peak wavelength for the short-wavelength emission were connected in series to form an array. Altogether, five LED arrays were constructed and each was mounted inside its own life-test chamber. The operating conditions of the five arrays and their estimated junction temperatures are shown in Table 12. These conditions were achieved by adjusting the LED drive current and the ambient temperature inside the chambers.

Table 12. Testing conditions and estimated junction temperatures for the 5-mm LED arrays in Experiment 1.

	Array #	Ambient Temperature (°C)	Drive Current (mA)	Estimated Junction Temperature (°C)
Group 1	Array 1	41	15	56
	Array 2	55	16	70
	Array 3	69	15	85
Group 2	Array 1	41	15	56
	Array 4	40	28	70
	Array 5	37	45	85

Figure 91 shows the relative light output as a function of time for the five LED arrays. For each array, the relative light output over time was normalized to its initial value. The horizontal axis is on a log scale. The light output decrease over time is exponential in nature and therefore, the light output, L, can be expressed as:

$$L = L_0 \cdot e^{-\alpha t} \qquad (6)$$

where α is the light output degradation rate, *t* is the operation time measured in hours, and L_0 is the initial light output, which is normalized to 100%.

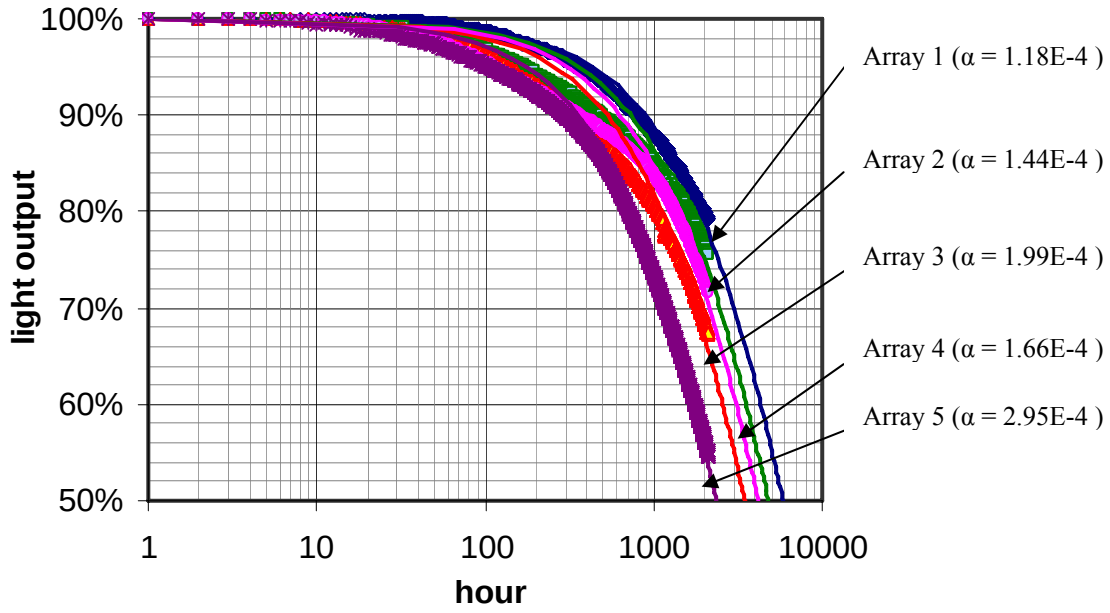


Fig. 91. Light output variation as a function time for the 5-mm LED arrays in Experiment 1.

Exponential curve fits yielded different degradation rates for each LED array. Figure 92 illustrates the variation of the degradation rate as a function of LED junction temperature. A higher degradation rate means faster light output depreciation. As the junction temperature increased, the degradation rate also showed an increasing trend. However, Fig. 92 shows that the junction temperature increase caused by drive current had a larger effect on the degradation rate than the junction temperature increase caused by ambient temperature.

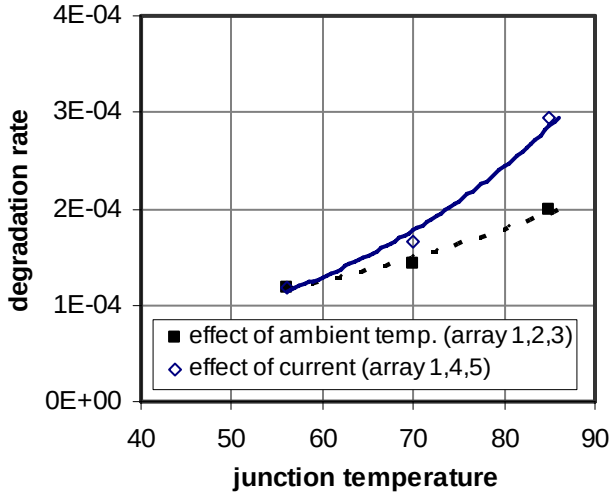


Fig. 92. Degradation rate α as a function of junction temperature for the 5-mm LED arrays in Experiment 1.

Experiment 2

The goal of the second experiment was to determine the effects of ambient heat and drive current on the degradation rate of high-flux white LEDs. Ten high-flux, single-die white LEDs, acquired in 2004, were selected from the same batch, and two LEDs with the same short-wavelength peak were connected in series to form an array. As before, five arrays of white LEDs were life-tested. The LEDs were operated at their rated current of 350 mA but at different ambient temperatures. The operating conditions of the five arrays and their estimated junction temperatures are summarized in Table 13.

Table 13. Testing conditions and estimated junction temperatures for the high-flux LED arrays in Experiment 2.

Array #	Ambient Temperature (°C)	Drive Current (mA)	Estimated Junction Temperature (°C)
Array 1	35	350	56
Array 2	45	350	59
Array 3	50	350	66
Array 4	55	350	68
Array 5	60	350	76

Figure 93 shows the relative light output as a function of time for the LED arrays, which had the same drive current but different ambient temperatures. Here, too, the light output decrease over time is exponential in nature. Exponential curve fits yielded the degradation rate for each LED array. Figure 94 illustrates the variation of the degradation rate as a function of junction temperature. With increasing junction temperature, the degradation rate increased exponentially.

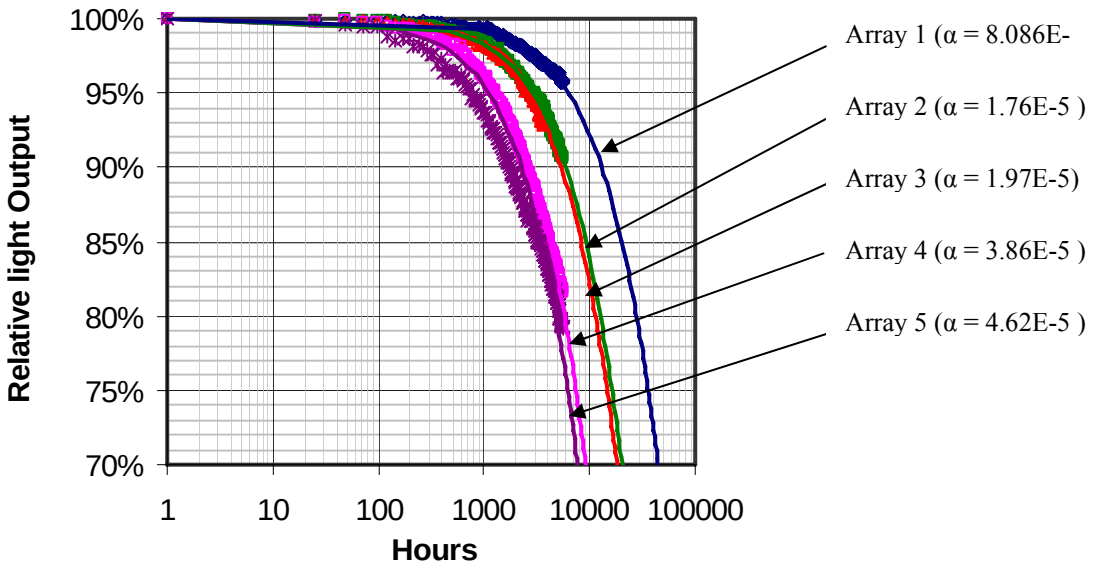


Fig. 93. Light output variation as a function time for the high-flux LED arrays in Experiment 2.

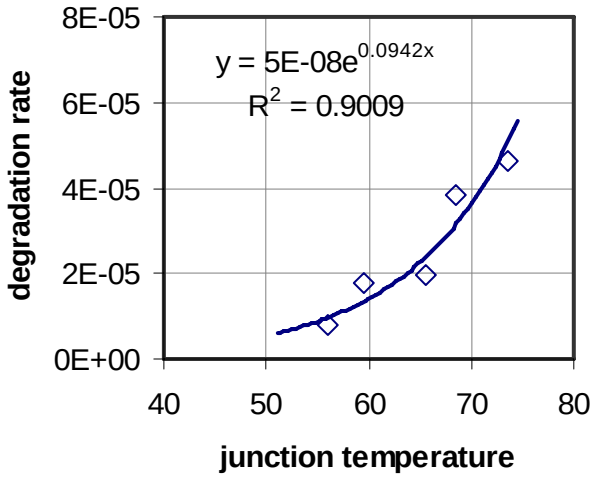


Fig. 94. Degradation rate α as a function of junction temperature for the high-flux LED arrays in Experiment 2.

Figure 95 combines the three conditions for the single-die white LEDs in Fig. 89. As shown in Fig. 95, this type of high-flux LED shows greater sensitivity, and thus faster degradation, to a junction temperature rise produced by ambient temperature than by drive current. Figure 96 shows the hypothesized degradation rates under the effects of ambient temperature and drive current. This is opposite of the effect observed in 5-mm LEDs (Fig. 92), which degrade more quickly with current-induced heat. This dissimilarity could possibly be induced by the package differences between 5-mm LEDs and high-flux LEDs. The silicon-based encapsulant of high-flux LEDs is less sensitive to short-wavelength radiation, which contributes to the yellowing of the encapsulant of 5-mm LEDs and causes faster light output depreciation. However, to verify the two curves in Fig. 96, one more life test is needed for the high-flux LEDs. In that life test, the high-flux LEDs should operate at the same ambient temperature but at different drive currents.

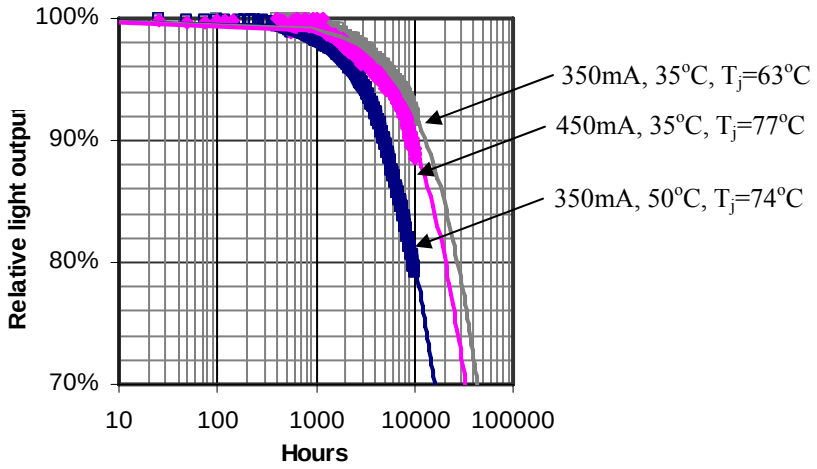


Fig. 95. Light output variation as a function time for the single-die white LEDs used in the first benchmarking study.

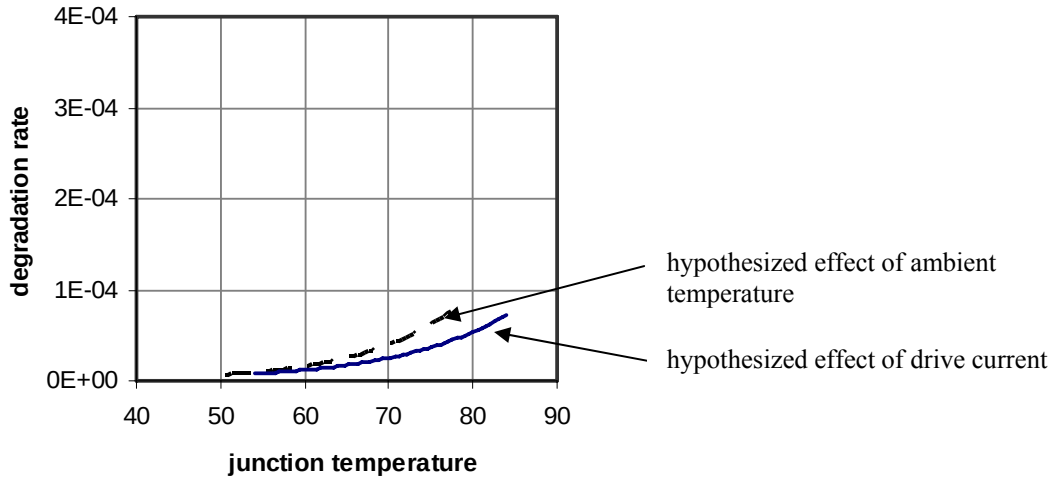


Fig. 96. Hypothesized degradation rate α as a function of junction temperature for high-flux LEDs.

Summary

Overall, the single-die green and white arrays of the first benchmarking study showed very little light loss after 10,000 hours, even with current and ambient temperature increases much above normal operating conditions. The blue and multi-die white LED arrays, on the other hand, seem to have a high degradation rate. Data extrapolation indicates that the single-die white LED will maintain 70% of its initial light output at 45,000 hours. The white LEDs showed significant color variations (of the order of a 12-step MacAdam ellipse) between each individual LED. However, the color shift over time was within a 4-step MacAdam ellipse. For white LEDs to be accepted broadly for general illumination applications, the color variation between similar products must become much smaller, of the order of a 2-step MacAdam ellipse, in order to match the performance of linear fluorescent lamps available at the present time. Until manufacturing processes improve to provide consistent color between similar LEDs, color binning is one option for creating arrays with unnoticeable color variation.

From Fig. 90 it appears that for the same ambient temperature, the different LEDs have different cathode pin temperatures and life values, even though it is too early to draw conclusions about the life for some LEDs. The results from the second benchmarking study indicate that the different LEDs would require different amounts of heat sink when being packaged into fixtures in order to have similar life. By testing different commercial white LEDs, we can understand the degradation mechanisms for different types of LEDs and work toward developing a metric for predicting the life of white LEDs.

Experiments from the life prediction study showed that the LED degradation rate changes as a function of junction temperature depending on the source of increasing heat (drive current or ambient heat). For 5-mm LEDs, rises in current-induced junction temperature have a greater effect on the degradation rate than rises in ambient heat-induced junction temperature. However, for high-flux LEDs, the ambient temperature seems to have a greater effect than the current. Nevertheless, one more life test is needed to verify this observation. Once a life predictor can be quantified, the LED life of a system can be estimated without long-term life testing.

CONCLUSIONS

Although UCSB's work in the first year of the project focused on vertical cavity surface-emitting lasers and ultraviolet light emitting diodes for generating white light via red-green-blue phosphor excitation, these devices required much more time for significant improvement than this project provided. Thus research emphasis shifted to blue MCLEDs in the second year. Due to their low overall device thickness, development of MCLED structures required improvements in not only film growth, but in particular post-growth processing. We found that the most viable process was to remove the (Al,In)GaN epitaxial device layer from its sapphire substrate, in a flip-chip process in which a silicon wafer supported the device. Then the device cavity was thinned using a combination of reactive-ion etching and mechanical polishing. These were critical processes, since optimal light extraction from the MCLED cavity required precise control of thickness. The MCLED that resulted had greater than 10% light extraction efficiency, which is superior to that of conventional planar LEDs, but needs improvement. We will continue pursuing growth and processing optimization to raise extraction efficiency.

UCSB also developed thick nonpolar GaN epitaxial layers and free-standing substrates. We optimized the LEO process for *a*-plane and *m*-plane GaN grown by hydride vapor phase epitaxy. In doing so, regions of very low dislocation density ($< 1 \times 10^6$ cm^{-2}) were obtained. In the case of *m*-plane GaN, nearly 2" diameter planar free-standing films were obtained by spontaneous separation from their $LiAlO_2$ substrates. The principle benefit of nonpolar GaN is the lack of electrical polarization fields in the conduction direction, which hinder the efficient recombination of electrons and holes in quantum wells.

UCSB grew and processed nonpolar blue LEDs on both *a*-plane and *m*-plane HVPE GaN templates, which showed impressive performance for initial devices. The LEDs on *a*-plane LEO HVPE GaN benefited from lowered average dislocation density, while LEDs on free-standing planar *m*-plane HVPE GaN had the advantage of better heat extraction into the GaN substrate. Most notably, these LEDs exhibited little or no wavelength shift with increasing drive current, which has been a persistent problem in conventional polar *c*-plane LEDs. Additionally, the optical output power was unsaturated at drive current values (*e.g.* 300 mA) much higher than observed for *c*-plane LEDs.

During the first year of this project, the LRC concentrated on developing the specifications for the proposed white light source by benchmarking existing high-power white LEDs, conducting human factors studies, and completing a literature review. In addition, the LRC characterized existing encapsulants to package the short-wavelength LEDs. During the second year, the LRC conducted extensive ray-tracing analyses to study device performance, and developed secondary optics to package UCSB's light emitters. A tubular white light source was produced using a light guide in front of a commercial blue LED. The phosphor was placed remotely over the light guide to improve overall system performance.

The LRC source modeling effort begun in Year 2 was continued by incorporating physical optics into the models, so that the modeled results agree with UCSB's light output measurement results. Further characterization of YAG:Ce phosphor material was completed, including careful analysis of the phosphor's optical properties and beam-scattering properties in the forward and reverse directions. Finally, alternate secondary optics were identified to create uniform radiation on the phosphor layer. The concept of making the encapsulant function as the distribution optics was investigated, and the better of the two candidates was selected for a final prototype light

source/fixture. A commercially available blue LED package was to be used in this task, and a prototype white light source was to be built and tested in the laboratory.

The LRC conducted a phosphor characterization study to better understand the interaction between short-wavelength light and phosphor and to quantify the amount of light reflected back to the die in a phosphor-converted white LED package. From the data gathered, the LRC estimated that at higher phosphor densities, approximately 40% of the light was transmitted through the phosphor-coated plate and the remaining 60% was reflected back toward the die. Therefore, it was concluded that a packaging method is needed to help extract these backscattered photons and raise the luminous efficacy of white LEDs.

The LRC hypothesized that by placing the phosphor layer away from the die, the backscattered light could be extracted before being absorbed by the die. Based on simulation results and current lab capabilities, an initial prototype of the "scattered photon extraction" (SPE) package was built. The SPE package places the phosphor away from the die onto the top layer of a secondary optic. Results comparing SPE and typical white LED packages showed that the average luminous flux and the corresponding average efficacy for six tested SPE packages were 90.7 lm and 36.3 lm/W, respectively. The average luminous flux and the corresponding average efficacy for six similar commercial white LED packages were 56.5 lm and 22.6 lm/W, respectively.

A comparison study of different source forms for general illumination was conducted in two parts: an optical ray-tracing analysis and a human factors study. Overall, an RCLED offers greater benefits when creating a linear light source compared to traditional HBLEDs. The RCLED package is about 60% more efficient than the traditional LED package. For the traditional LED, maximum efficiency is reached at a diameter of 0.25 inch. With the RCLED, the rod diameter can be smaller, 0.1 inch. With the encapsulated method, it is possible to achieve similar optical efficiencies with both types of LEDs (RCLED and traditional HBLED).

To understand how people react to the two types of lighting, a human factors study was conducted to understand their preferences. For this study, two experiments were conducted: a mockup experiment and a scale model experiment. The mockup experiment compared two application styles, downlight and general diffuse light from a suspended linear source (a light pipe). The results suggested that the light pipe condition was rated as the dimmest lighting condition and as the least appropriate condition for commercial lighting. The results also suggested that the lighting condition with 12 downlight luminous elements in the field of view was rated as the brightest lighting condition and as the most appropriate condition for office and commercial lighting. The sensation of glare was reduced as the number of luminous elements increased for a fixed total area and a fixed luminance of luminous elements. In the scale model experiment, the results suggested that lighting conditions with 12 luminous elements were rated as the most appropriate. As the size of each element decreased while the number of downlight luminous elements increased to maintain appropriate illuminance, the room became less glaring for the same luminance. Larger luminaire spacing, which provides a more uniform illuminance distribution, may be preferred with an appropriate number of downlights.

In the area of epoxy development, efforts turned towards silicone-epoxy resins after initial studies found that simple organic resins could not be considered for LED encapsulants due to their significant yellowing at 140°C. It was reasoned that if the epoxy portion of the molecule were eliminated, it might be possible to achieve a reasonable level of thermal oxidative stability. Thus, several polydimethylsiloxane (silicone) resins were evaluated. The results were dramatic. Even after four weeks at 140°C in air, there was no observable yellowing. Polydimethyl-

siloxanes appear to have excellent, inherent oxidative stability. However, on long-term exposure to heat, even these resins undergo slow, degradative bond cleavage reactions. Over the course of the third year, the structure of the Si-H containing oligomer has changed substantially. After a series of tests and changes, Rensselaer's Chemistry group is now confident that the chemical approach to the design of encapsulants using thermoset silicone resins for high-intensity LEDs is correct.

In the third year of the project, the LRC voluntarily continued its experimental studies from Years 1 and 2 to benchmark the performance of current LED devices. The results showed that single-die green and single-die white LEDs degraded slowly, even under increased drive current and ambient temperature, whereas single-die blue and multi-die white LEDs showed the highest rates of degradation. Experiments from the life prediction study showed that the LED degradation rate changes as a function of junction temperature depending on the source of increasing heat (drive current or ambient heat). For 5-mm LEDs, rises in current-induced junction temperature have a greater effect on the degradation rate than rises in ambient heat-induced junction temperature. However, for high-flux LEDs, the ambient temperature seems to have a greater effect than the current.

UCSB PUBLISHED PAPERS AND PATENTS

2005 Papers

Pattison MP, Sharma R, David A, Waki I, Weisbuch C, Nakamura S, "Gallium nitride based micro-cavity light emitting diodes emitting at 498nm", submitted to Applied Physics Letters.

Haskell BA, Baker TJ, McLaurin MB, Wu F, Fini PT, DenBaars SP, Speck JS, Nakamura S. "Defect reduction in (11$\underline{2}$00) m-plane gallium nitride via lateral epitaxial overgrowth by hydride vapor phase epitaxy", Applied Physics Letters, vol.86, no.11, pp.111917-1-3 (2005).

Chakraborty A, Keller S, Meier C, Haskell BA, Keller S, Waltereit P, DenBaars SP, Nakamura S, Speck JS, Mishra UK; "Properties of nonpolar a-plane InGaN/GaN multiple quantum wells grown on lateral epitaxially overgrown a-plane GaN", Applied Physics Letters, vol.86, no.3, pp.31901-1-3 (2005).

2004 Papers

Fujii T, David A, Schwach C, Pattison PM, Sharma R, Fujito K, Margalith T, Denbaars SP, Weisbuch C, Nakamura S; "Microcavity effect in GaN-based light-emitting diodes formed by laser lift-off and etch-back technique", Japanese Journal of Applied Physics Part 2-Letters, vol.43, no.3B, pp.L411-13 (2004)

Weisbuch C, David A, Fujii T, Schwach C, DenBaars SP, Nakamura S, Rattier M, Benisty H, Houdr R, Stanley R, Carlin J-F, Krauss TF, Smith CJM; "Recent results and latest views on microcavity LEDs", SPIE-Int. Soc. Opt. Eng. Proceedings of SPIE - the International Society for Optical Engineering, vol.5366, no.1, pp.1-19 (2004).

Chakraborty A, Xing H, Craven MD, Keller S, Mates T, Speck JS, DenBaars SP, Mishra UK; "Nonpolar a-plane p-type GaN and p-n junction diodes" Journal of Applied Physics, vol.96, no.8, pp.4494-9 (2004).

2003 Papers

Katona TM, Schmidt MC, Margalith T, Moe C, Tamura H, Sato H, Funaoka C, Underwood R, Nakamura S, Speck JS, DenBaars SP; "336 nm ultraviolet LEDs grown with AlN interlayers for strain reduction", Physica Status Solidi C, no.7, pp.2206-9 (2003).

Haskell BA, Wu F, Matsuda S, Craven MD, Fini PT, DenBaars SP, Speck JS, Nakamura S. "Structural and morphological characteristics of planar (11$\underline{2}$0) a-plane gallium nitride grown by hydride vapor phase epitaxy", Applied Physics Letters, vol.83, no.8, pp.1554-6 (2003).

Haskell BA, Wu F, Craven MD, Matsuda S, Fini PT, Fujii T, Fujito K, DenBaars SP, Speck JS, Nakamura S; "Defect reduction in (11$\underline{2}$0) a-plane gallium nitride via lateral epitaxial overgrowth by hydride vapor-phase epitaxy", Applied Physics Letters, vol.83, no.4, pp.644-6 (2003).

Pending Patents/Applications

A. Patent Identification: N/A
Date Submitted or Issued: U.C. ROI submitted 6/1/05
Title of Patent: Semiconductor Micro-Cavity Light Emitting Diode
Type of Patent: Record of Invention filed; no provisional patent filed yet
Brief Summary: This U.C. Record of Invention describes light-emitting devices termed 'micro-cavity' light emitting diodes (MC-LEDs), based on the gallium nitride semiconductor system. Such devices exhibit enhanced light emission efficiency, spectral narrowing, and emission directionality, which are all the result of interference of light within a carefully tailored cavity. The successful fabrication of MC-LEDs requires precise control of thin-film growth as well as device processing, the techniques for which are covered in this disclosure.

B. Patent Identification: U.C. Case #2005-144
Date Submitted or Issued: 2/28/05
Title of Patent: Horizontal Emitting, Vertical Emitting, Beam Shaped, Distributed Feedback (DFB) Lasers By Growth Over A Patterned Substrate
Type of Patent: U.S. Provisional patent
Brief Summary: The invention describes new laser structures with simplified fabrication processing. They rely on active layers directly grown on patterned substrates. Such lasers can emit in the device plane. They can also emit outside the plane by having the guided light shaped into extracted light thanks to a buried diffraction grating. Eventually another buried grating can act as a distributed feedback (DFB) for single wavelength emission. In addition, the gratings act as patterned growth masks for Lateral Epitaxial Overgrowth (LEO). The high index contrast between the active layer and the LEO layer diminishes spontaneous emission outside guided modes.

C. Patent Identification: U.C. Case #2005-145
Date Submitted or Issued: 2/28/05
Title of Patent: Single Or Multi-Color High Efficiency Light Emitting Diode (LED) By Growth Over A Patterned Substrate
Type of Patent: U.S. Provisional Patent
Brief Summary: The invention describes new LED structures that provide increased light extraction efficiency retaining a planar structure. The new LED structures have direct emission outside the structure and, in addition, convert the guided light into extracted light thanks to a buried diffraction grating. In addition, this grating acts as a growth mask for Lateral Epitaxial Overgrowth (LEO). The high index contrast between the active layer and the LEO layer ensures that emission into unwanted leaky modes is kept to a minimum.

LRC PUBLISHED PAPERS AND FILED PATENTS

2005 Papers

Narendran, N. and Y. Gu. In press. Life of LED-based white light sources. *Journal of Display Technology*.

Narendran, N., Y. Gu, J.P. Freyssinier-Nova, and Y. Zhu. 2005. Extracting phosphor-scattered photons to improve white LED efficiency. *Phys. stat. sol. (a)* 202 (6): R60-R62.

2004 Papers

Gu, Y., and N. Narendran. 2004. A non-contact method for determining junction temperature of phosphor-converted white LEDs. *Third International Conference on Solid State Lighting, Proceedings of SPIE* 5187: 107-114.

Gu, Y., N. Narendran, and J.P. Freyssinier. 2004. White LED performance. *Fourth International Conference on Solid State Lighting, Proceedings of SPIE* 5530, eds. I.T. Ferguson, N. Narendran, S.P. DenBaars, J.C. Carrano, 119-124. Bellingham, WA: International Society of Optical Engineers.

Narendran, N., L. Deng, R.M. Pysar, Y. Gu, and H. Yu. 2004. Performance characteristics of high-power light-emitting diodes. *Third International Conference on Solid State Lighting, Proceedings of SPIE* 5187: 267-275.

Narendran, N., Y. Gu, J.P. Freyssinier, H. Yu, and L. Deng. 2004. Solid-state lighting: Failure analysis of white LEDs. *Journal of Crystal Growth* 268 (3-4): 449-456.

Narendran, N., Y. Gu, and R. Hosseinzadeh. 2004. Estimating junction temperature of high-flux white LEDs. In *Light-emitting diodes: Research, manufacturing, and applications VIII*, *Proceedings of SPIE* 5366, eds. S.A. Stockman, H.W. Yao, E.F. Schubert, 158-160. Bellingham, WA: International Society of Optical Engineers.

Pending Patents

Patent Identification: Invention disclosure OTC 936, US60/622653
Date Submitted or Issued: Submitted 10-26-2004
Title of Patent: Silicone Resin Encapsulants for Light Emitting Diodes
Type of Patent: Provisional

Patent Identification: Invention disclosure OTC 858
Date Submitted or Issued: Submitted 05-05-2005
Title of Patent: Novel package for producing white light with short-wavelength LEDs/RCLEDs and down conversion phosphors
Type of Patent: utility PCT application

REFERENCES

[Benisty 1998] H. Benisty, H. De Neve, and C. Weisbuch, IEEE J. Quantum Electron. **34**, 1612 (1998).

[Bernecker 1985] Bernecker, C. and J.M. Mier. 1985. The effect of source luminance on the perception of environment brightness. *J. Ill. Eng. Soc.* 15(1): 253-271.

[Blondelle 1995] J. Blondelle, H. De Neve, P. Demeester, P. Van Daele, G. Borghs, and R. Baets, Electron. Lett. **31**, 1286 (1995).

[Calle 2002] F. Calle, F.B. Naranjo, S. Fernández, M.A. Sánchz-García, E. Calleja, and E. Muñoz, Phys. Status Solidi A **192**, 277 (2002).

[Chichibu 2004] S. Chichibu, T. Sota, K. Wada and S. Nakamura: J. Vac. Sci. & Technol. B 16 (1998) 2204.

[CIE 1995] Commission International de l'Éclairage (CIE). 1995. CIE 117-1995: Discomfort glare in interior lighting.

[CIE 2002] Commission International de l'Éclairage (CIE). 2002. CIE 146-2002: CIE collection on glare.

[Connell 1995] Connell, J.W., J.V. Crivello, and D. Bi. 1995. The effect of low earth orbit atomic oxygen exposure on epoxy functionalized siloxanes. *J. Appl. Polym. Sci.* 57: 1251-1259.

[Crivello 1997a] Crivello, J.V., and Z. Mao. 1997a. Cationic photopolymerization of organic-inorganic hybrid matrixes. *Chem. Mater.* 9(7): 1562-1569.

[Crivello 1997b] Crivello, J.V., and Z. Mao. 1997b. Synthesis of multifunctional siloxane oligomers using Sol-Gel techniques and their photoinitiated cationic polymerization. *Chem. Mater.* 9(7): 1554-1561.

[David 2000] S. David, A. Chelnokov, and J.-M. Lourtioz, "Wide angularly isotropic photonic bandgaps obtained from two-dimensional photonic crystals with Archimedean-like tilings", Optics Lett. 25 1001-3 (2000).

[De Mierry 2002] P. De Mierry, J.M. Bethoux, H.P.D. Schenk, M. Vaille, E. Feltin, B. Beaumont, M. Leroux, S. Dalmasso, and P. Gibart, Phys. Status Solidi A **192**, 335 (2002).

[De Neve 1997] H. De Neve, J. Blondelle, P. Van Daele, P. Demeester, and R. Baets, Appl. Phys. Lett. **70**, 799 (1997).

[Dill 1998] C. Dill, R.P. Stanley, U. Oesterle, D. Ochoa, and M. Ilegems, Appl. Phys. Lett. **73**, 3812 (1998).

[Einhorn 1969] Einhorn H.D. 1969. An analytical expression for the glare position index. *Illum. Eng.* 64(4): 228-229.

[Einhorn 1991] Einhorn H.D. 1991. Discomfort glare from small and large sources. *Proceedings of the 1st International Symposium on Glare*, 101-114.

[Flynn 1975] Flynn J.E., T.J. Spencer, O. Martyniuk, and C. Hendrick. 1975. The influence of spatial light on human judgment. *Proceedings of 18th CIE Session*, 39-46.

[Flynn 1977] Flynn J.E. 1977. A study of subjective responses to low energy and non-uniform lighting systems. *Light. Des. and App.* 7(2): 167-179.

[Fujii 2004] T. Fujii, A. David, C. Schwach, P.M. Pattison, R. Sharma, K. Fujito, T. Margalith, S.P. DenBaars, C. Weisbuch, and S. Nakamura, Jpn. J. Appl. Phys. **43**, L411 (2004).

[Gu 2004] Gu, Y., N. Narendran, and J.P. Freyssinier. 2004. White LED performance. *Fourth International Conference on Solid State Lighting,* Proceedings of SPIE 5530, eds. I.T. Ferguson, N. Narendran, S.P. DenBaars, J.C. Carrano, 119-124. Bellingham, WA: International Society of Optical Engineers.

[Hopkinson 1957] Hopkinson, R.G. 1957. Evaluation of glare. *Illum. Eng.* 52(6): 305-316.

[Loe 1994] Loe D.L., K.P. Mansfield, and E. Rowlands. 1994. Appearance of lit environment and its relevance in lighting design: experimental study. *Light. Res. and Tech.* 26(3): 119-133.

[Luckiesh 1949] Luckiesh M. and S.K. Guth S. 1949. Brightness in visual field at borderline between comfort and discomfort (BCD). *Illum. Eng.* 64: 650-666.

[Mukai 1997] Mukai K, Y. Akashi, and Y. Tanabe. 1997. New office lighting system to realize comfortable lighting environment with low energy. *Proceedings of 3rd Lux Pacifica*.

[Nakamura 1994] Nakamura S., T. Mukai. and M. Senoh. 1994. Candela-class high-brightness InGaN/AlGaN double-heterostructure blue-light-emitting diodes. *Appl. Phys. Lett.* 64(13): 1687-1689.

[Narendran 2004] Narendran N., Y. Gu, J. P. Freyssinier, H. Yu, and L. Deng. 2004. Solid-State Lighting: Failure Analysis of White LEDs. *J. Crys. Gro.* 268(3-4): 449-456.

[Narendran 2005] Narendran N., Y. Gu, J. P. Freyssinier-Nova, Y. Zhu. 2005. Extracting phosphor-scattered photons to improve white LED efficiency. *Phys. stat. sol. (a)* 202(6): R60-R62.

[Paul 1999] Paul B.M., and H.M. Einhorn. 1999. Discomfort glare from small light sources. *Light. Res. and Tech.* 31(4): 139-144.

[Petherbridge 1950] Petherbridge P., and R.G. Hopkinson. 1950. Discomfort glare and the lighting of buildings. *Transaction of Illuminating Engineering Society* (London) 15(1): 39-79.

[Putnam 1951] Putnam R.C., and R.E. Faucett. 1951. The threshold of discomfort glare at low adaptation levels. *Illum. Eng.* 46(10): 505.

[Rattier 2003] M. Rattier, H. Benisty, E. Schwoob, C. Weisbuch, T. F. Krauss, C. J. M. Smith, R. Houdré and U. Oesterle, "Omnidirectional and compact guided light extraction from Archimedean photonic lattices", Appl. Phys. Lett. 83 1283-5 (2003).

[Schubert 1992] E.F. Schubert, Y.H. Wang, A.Y. Cho, L.W. Tu, G.J. Zydzik, Appl. Phys. Lett. **60**, 921 (1992).

[Shaw 2002] A. Shaw, T. McCormack, A.L. Bradley, J.G. Lunney, and J.F. Donegan, Phys. Status Solidi A **192**, 103 (2002).

[Shaw 2004] A. J. Shaw, A. L. Bradley, J. F. Donegan, and J. G. Lunney, IEEE Phot. Tech. Lett. **16**, 2006 (2004).

[Tiller 1995] Tiller D.K., and J.A. Veitch. 1995. Perceived room brightness: Pilot study on the effect of luminance distribution. *Light. Res. and Tech.* 27(2): 93-101.

[Vanfleet 2003] R. R. Vanfleet, J. A. Simmons, H. P. Maruska, D. W. Hill, M. M. C. Chou, and B. H. Chai, Appl. Phys. Lett., **83** (6) 1139 (2003).

[Weisbuch 2004] C. Weisbuch, A. David, T. Fujii, C. Schwach, S. Denbaars, S. Nakamura, M. Rattier, H. Benisty, R. Houdré, R. Stanley, J.F.Carlin, T.F. Krauss, C.J.M. Smith, "Recent results and latest views on microcavity LEDs", to be published in SPIE Proceedings, 2004.

[Yamada 2003] Yamada K., Y. Imai, and K. Ishii. 2003. Optical simulation of light source devices composed of blue LEDs and YAG phosphor. *J. Light & Vis. Env.* 27(2): 70-74.

APPENDICES

A.1: Views of experimental conditions for the mockup experiment



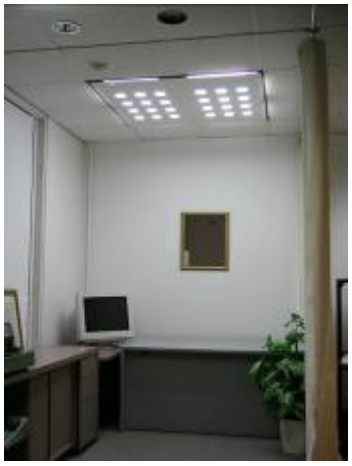
(1) DL-2



(2) DL-6



(3) DL-12



(4) DL-24



(5) DL-48



(6) LP-2

A.2: Questionnaire for mockup experiment

SUBJECTIVE APPRAISAL OF LED LIGHTING SCHEMES

Lighting Scheme – Number of luminaires: _____

Date: _____

This experiment explores the effectiveness of different layouts of recessed downlights that use LED light sources. In this pilot study, we have tried to simulate LED fixtures by using a fluorescent luminaire and a perforated plate. Please try to assume the light sources to be LED sources, and observe the light sources as well as the pattern of illumination of the "room". Please answer the following questions based on your evaluation of the space and the light sources.

I find this lighting condition to be:

Dim	-3	-2	-1	0	1	2	3	Bright
Non-uniform	-3	-2	-1	0	1	2	3	Uniform
Boring	-3	-2	-1	0	1	2	3	Interesting
Private	-3	-2	-1	0	1	2	3	Public
Simple	-3	-2	-1	0	1	2	3	Complex
Unpleasant	-3	-2	-1	0	1	2	3	Pleasant
Somber	-3	-2	-1	0	1	2	3	Cheerful
Confined	-3	-2	-1	0	1	2	3	Spacious
Gloomy	-3	-2	-1	0	1	2	3	Radiant
Subdued	-3	-2	-1	0	1	2	3	Stimulating
Glary	-3	-2	-1	0	1	2	3	Comfortable
Dislike	-3	-2	-1	0	1	2	3	Like

Is this type of lighting acceptable to you for the following applications?
(-2 highly unacceptable, 1 unacceptable, 0 not sure, 1 acceptable, 2 highly acceptable):

Office Lighting	-2	-1	0	1	2
Residential Lighting	-2	-1	0	1	2
Commercial Lighting – Stores, Restaurants, Hotels etc.	-2	-1	0	1	2

Is this type of lighting acceptable to you with respect to the shadows that are formed?

-2 -1 0 1 2

Do you find the effect of the lighting on your face to be:

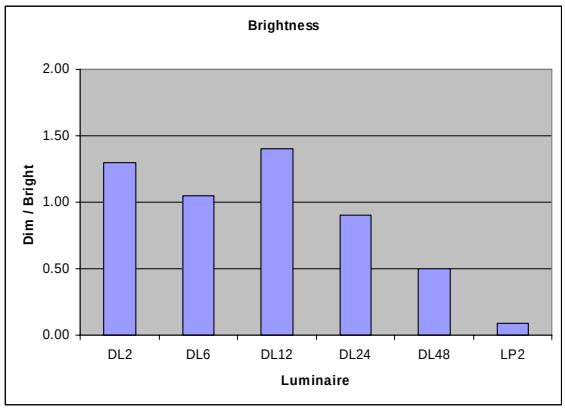
Too harsh Harsh Neutral Soft Too soft

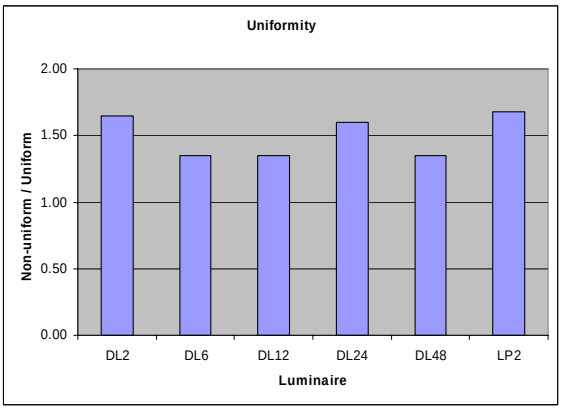
Do you find the number of lights and their spacing to be:

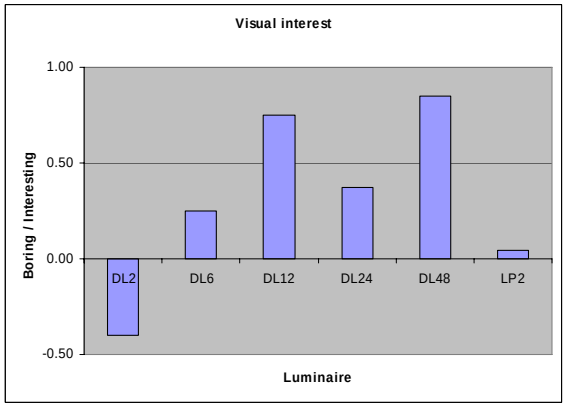
Too many	More than necessary	Appropriate for this room	Fewer than necessary	Much Less than necessary

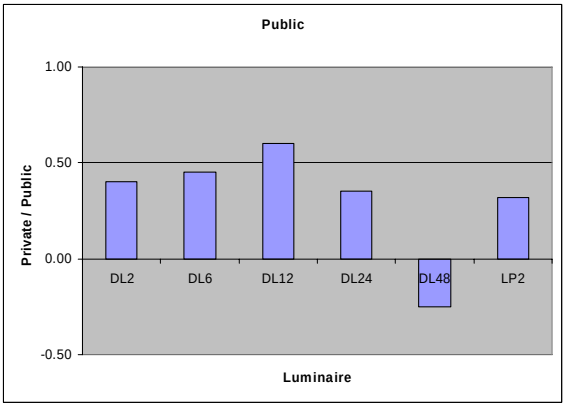
Thank you for participating in this experiment.

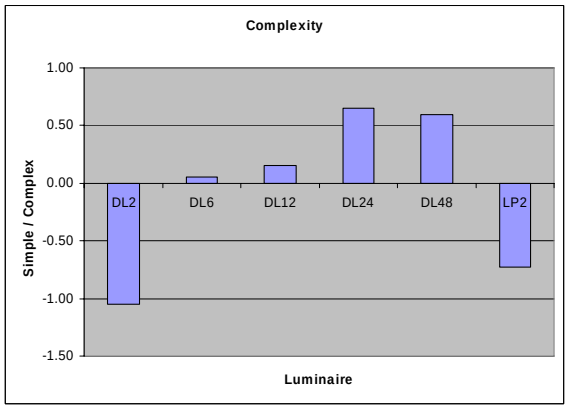
A.3: Results of subjective evaluations for the 12 pairs of contrasting words

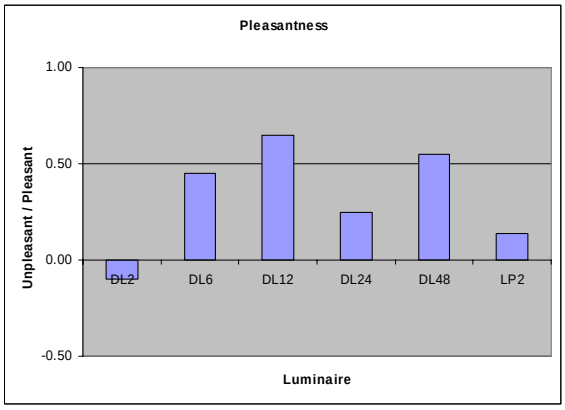




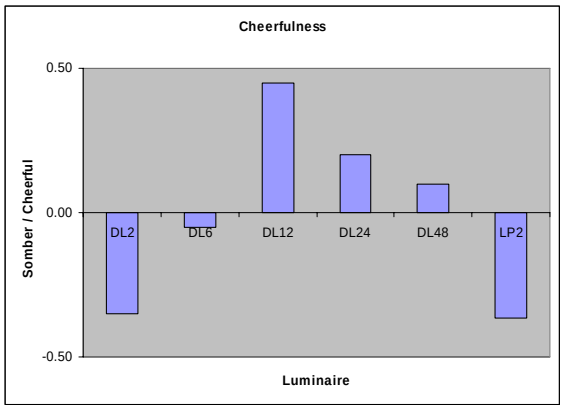


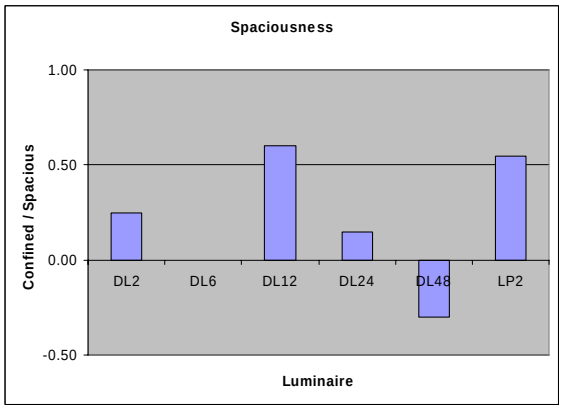


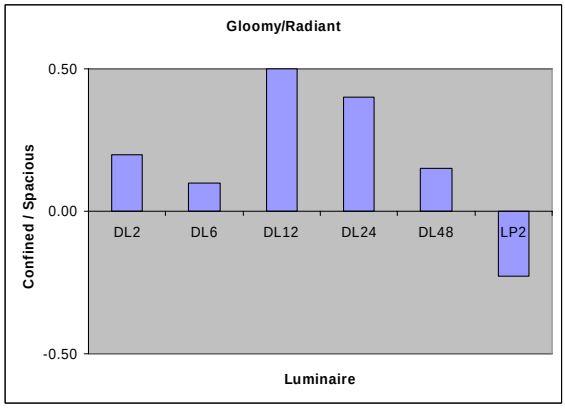


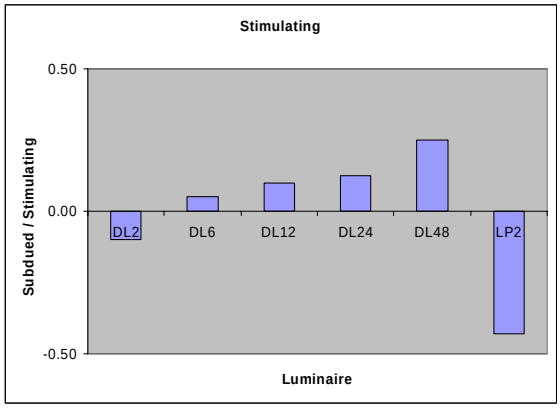


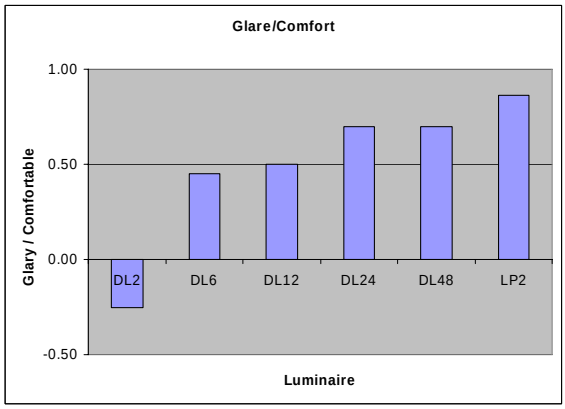
A.3 (Cont.)

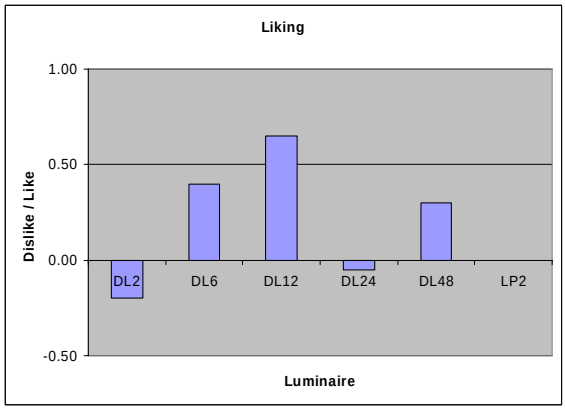

Cheerfulness
Somber / Cheerful
0.50
0.00
-0.50
DL2
DL6
DL12
DL24
DL48
LP2
Luminaire


Spaciousness
Confined / Spacious
1.00
0.50
0.00
-0.50
DL2
DL6
DL12
DL24
DL48
LP2
Luminaire


Gloomy/Radiant
Confined / Spacious
0.50
0.00
-0.50
DL2
DL6
DL12
DL24
DL48
LP2
Luminaire


Stimulating
Subdued / Stimulating
0.50
0.00
-0.50
DL2
DL6
DL12
DL24
DL48
LP2
Luminaire


Glare/Comfort
Glary / Comfortable
1.00
0.50
0.00
-0.50
DL2
DL6
DL12
DL24
DL48
LP2
Luminaire

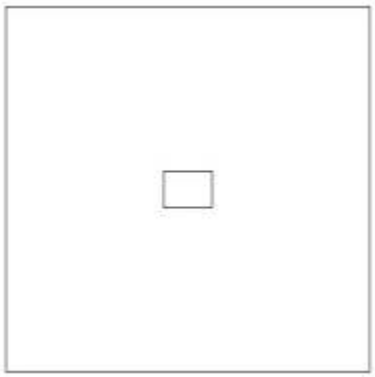

Liking
Dislike / Like
1.00
0.50
0.00
-0.50
DL2
DL6
DL12
DL24
DL48
LP2
Luminaire

A.4: UGR formula (CIE, 1995)

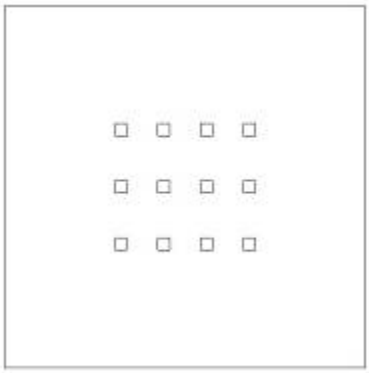
$$UGR = 8\log_{10}(0.25 / L_b)\sum(L^2\omega / p^2)$$

$L_{b:}$ Background luminance [cd/m^2]
L: Luminance of source [cd/m^2]
ω: Solid angle of source [sr]
p: Position index (Luckiesh and Guth, 1949)

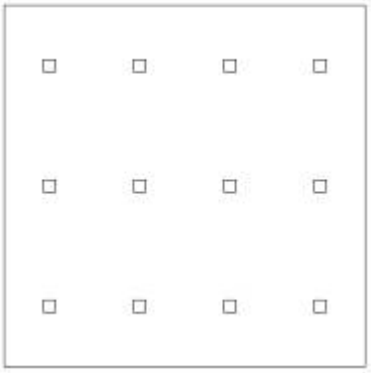
A.5: Layouts and views of light sources in scale model experiment



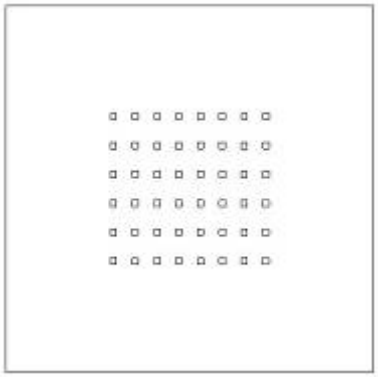
Condition 1



Condition 2



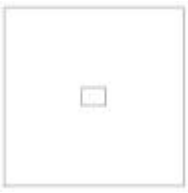
Condition 3



Condition 4



Condition 5



Condition 6



Condition 7



Condition 8

A.5 (Cont.)



View of Condition 7



View of Condition 5

A.6: Questionnaire for scale model experiment

SUBJECTIVE APPRAISAL OF DOWNLIGHTS

Lighting condition: _____
Subject: _____
Date: _____

Please observe the light sources and the space illuminated by the light sources. Then, please answer the following questions based on your evaluation of the light sources and space by circling the number which most closely describes the degree of your agreement with each statement.

How does the space appear?

Dim	-3	-2	-1	0	1	2	3	Bright
Non-uniform	-3	-2	-1	0	1	2	3	Uniform
Boring	-3	-2	-1	0	1	2	3	Interesting
Unpleasant	-3	-2	-1	0	1	2	3	Pleasant
Dislike	-3	-2	-1	0	1	2	3	Like

How do the light sources appear?

The light sources are too bright.
-2: disagree -1: somewhat disagree 0: neutral 1: somewhat agree 2: agree

The light sources are too dim.
-2: disagree -1: somewhat disagree 0: neutral 1: somewhat agree 2: agree

The number of light sources is:
-2: too many -1: more than necessary 0: appropriate 1: fewer than necessary 2: too few

I like the layout of the light sources.
-2: disagree -1: somewhat disagree 0: neutral 1: somewhat agree 2: agree

Additional Comments:

Thank you for your time and contribution.

A.7: Results (p-values) of t-tests for the scale model experiment

A pair of conditions with a p-value below 0.05 was regarded as a significant difference.

Brightness	1	2	3	4	5	6	7
1							
2	0.346						
3	**0.016**	**0.049**					
4	0.086	0.749	0.102				
5	0.204	0.625	0.187	0.801			
6	0.144	0.562	0.235	0.651	1.000		
7	1.000	0.203	**0.001**	0.076	0.090	**0.048**	
8	1.000	0.249	**0.001**	0.116	0.175	0.076	1.000

Uniform	1	2	3	4	5	6	7
1							
2	**0.003**						
3	**0.000**	**0.000**					
4	**0.002**	0.172	**0.008**				
5	**0.000**	**0.000**	0.310	**0.002**			
6	**0.006**	0.299	**0.009**	0.905	**0.006**		
7	**0.000**	**0.003**	**0.042**	0.108	**0.002**	0.115	
8	**0.000**	**0.000**	1.000	**0.004**	0.331	**0.009**	**0.024**

Interest	1	2	3	4	5	6	7
1							
2	**0.035**						
3	**0.000**	**0.006**					
4	**0.000**	**0.049**	0.393				
5	**0.000**	**0.001**	0.083	0.060			
6	1.000	**0.002**	**0.000**	**0.001**	**0.000**		
7	**0.007**	0.095	0.094	0.508	**0.004**	**0.001**	
8	**0.001**	**0.004**	0.842	0.346	0.227	**0.000**	**0.042**

Pleasant	1	2	3	4	5	6	7
1							
2	0.079						
3	**0.000**	**0.009**					
4	**0.010**	0.412	**0.085**				
5	**0.002**	**0.019**	0.848	0.116			
6	0.570	0.177	**0.002**	**0.074**	**0.008**		
7	**0.006**	**0.046**	0.261	0.562	0.421	**0.009**	
8	**0.002**	**0.025**	0.834	0.189	1.000	**0.001**	0.412

A.7 (Cont.)

Liking	1	2	3	4	5	6	7
1							
2	**0.024**						
3	**0.000**	**0.013**					
4	**0.003**	0.483	0.053				
5	**0.000**	**0.033**	0.507	0.097			
6	0.193	0.187	**0.001**	0.101	**0.006**		
7	**0.001**	0.061	0.085	0.500	0.249	**0.006**	
8	**0.000**	**0.020**	0.682	0.149	0.881	**0.001**	0.120

Too bright	1	2	3	4	5	6	7
1							
2	0.185						
3	0.185	1.000					
4	**0.015**	**0.037**	**0.037**				
5	**0.042**	0.384	0.368	0.288			
6	0.564	0.409	0.409	**0.035**	0.083		
7	**0.003**	**0.005**	**0.008**	0.528	0.177	**0.017**	
8	**0.000**	**0.003**	**0.009**	0.409	0.120	**0.004**	0.848

Too dim	1	2	3	4	5	6	7
1							
2	0.163						
3	0.466	**0.046**					
4	0.331	0.854	0.095				
5	0.868	0.368	0.135	0.298			
6	0.734	0.177	0.695	0.110	0.564		
7	**0.035**	0.317	**0.001**	0.110	**0.030**	**0.015**	
8	0.868	0.399	0.263	0.430	1.000	0.528	0.017

number	1	2	3	4	5	6	7
1							
2	**0.000**						
3	**0.000**	**0.000**					
4	**0.000**	**0.002**	0.130				
5	**0.000**	**0.000**	**0.001**	0.361			
6	**0.046**	0.057	**0.000**	**0.000**	**0.000**		
7	**0.000**	**0.001**	0.495	0.095	**0.002**	**0.001**	
8	**0.000**	**0.000**	0.172	0.607	0.083	**0.000**	0.069

A.7 (Cont.)

Layout	1	2	3	4	5	6	7
1							
2	0.055						
3	**0.000**	**0.005**					
4	**0.003**	0.482	**0.028**				
5	**0.000**	**0.049**	0.149	0.187			
6	0.369	0.274	**0.001**	0.124	**0.006**		
7	**0.000**	**0.009**	0.321	0.108	1.000	**0.005**	
8	**0.001**	**0.005**	0.592	0.120	0.495	**0.001**	0.562